King's College London

Department of Physics

A Measurement of the Cosmogenic Neutron Production in Water at the SNO+ Experiment

Katharine Dixon

Supervisor: Prof. Jeanne Wilson

A thesis presented for the degree of

Doctor of Philosophy

July 2025

Declaration

I hereby declare that, except where specific reference is made to the work of others, the contents of this thesis are original and have not been submitted in whole or in part for consideration for any other degree or qualification in this, or any other university.

Katharine Dixon

Date: January 9, 2026

Acknowledgements

Well we are finally here, and I can say for certain that we would not be at this point without my supervisor, Jeanne. You have gone above and beyond anything I could have hoped for in a supervisor, and I feel incredibly fortunate to have had the chance to work alongside you. Your advice and support have been invaluable. It was truly an honour to be your student.

I must also thank Daniel. Although you only became my postdoc halfway through my PhD, the real progress only began once you were around to provide guidance and support. You were also excellent company for revisiting the old Sudbury classics with.

I would also like to thank everyone on SNO+. Whether I have asked you for help, worked with you, or have just been to karaoke with you, you're all a great bunch of people to be around. In particular, thanks to Jeff and Eric for reviewing my analysis so this could actually happen. To Szymon and Christine, for giving me something fun to work on while underground. To Lorna, for helping me get started and making everything feel a lot less overwhelming. To Bill, for answering all my dumb RAT questions. Also, no name I have had (or will ever have) will beat the name "Lee". And finally, to Chloe, Ben and Gully for making Sudbury a lot more fun the second time around. Thank you for being my friends (and for chopping all those logs on the farm).

To all past and present members of the EPAP group. You have all been such lovely people to work and hang out with. I hope we get to do it again in the future.

I definitely would not have survived London if it weren't for all my friends here,

so thank you everyone. In particular, thank you, Lucy, for making the big move with me. It was far less scary with you by my side, and now we're London pros. To Catherine, undergrad physics would have been so much tougher without you. And, of course, to the boys: Rory, Jonny and Harry, you have made my final year here the best one yet. I don't know what I'll do without you guys around to hype me up.

Thank you to John, Michelle and Belle. Without you, I would have had nowhere to live in my second year. Letting me stay in your lovely house, taking me to and from the airport, and feeding me with Nando's was one of the kindest things anyone has ever done for me.

And lastly, my family. Thank you for your amazing support this whole time. It was always a comfort to know that you'd always be there for me, and that at the end of the day, I could always come back home and work with Tilly on the farm. I am very lucky to have had that.

> "Well, I must close, for I must now write at breakneck speed. Everything has been composed, but not yet written down."
>
> — Wolfgang Mozart

Abstract

Cosmogenic neutrons are produced in cosmic muon-induced interactions, and are backgrounds to many low-energy physics searches. Understanding their production aids in the cosmogenic neutron background estimation for experiments. The number of neutrons a muon produces will depend on the energy of the muon and the material through which the muon is propagating. The neutron yield has been measured by a number of experiments, over a wide range of muon energies.

As presented in this thesis, the SNO+ experiment has measured the cosmogenic neutron yield in water to be $Y_n^\mu = (3.38^{+0.23}_{-0.30}) \times 10^{-4}\,\mathrm{cm}^2\mathrm{g}^{-1}\mu^{-1}$. This value disagrees with the GEANT4 prediction for water in SNO+, which is given by $Y_n^\mu = (2.130 \pm 0.001(\mathrm{stat})) \times 10^{-4}\,\mathrm{cm}^2\mathrm{g}^{-1}\mu^{-1}$. This discrepancy between measurement and GEANT4 simulation is consistent with previous comparisons by the Daya Bay collaboration.

SNO+ receives an average muon energy of (364.1 ± 0.1) GeV, one of the highest among the current underground laboratories. This neutron yield measurement is important for improving models for neutron production at high energies. At this energy, the SNO+ result for the neutron yield agrees with the FLUKA prediction.

SNO+ uses the same detector used by the SNO experiment. SNO made a measurement of the neutron yield using heavy water that is approximately double this result. This is the first comparison between light water and heavy water that uses the same muon flux, giving a unique observation of how atomic weight affects the muon-induced neutron production.

Contents

List of Figures

List of Tables

Nomenclature

$0\nu\beta\beta$ Decay	Neutrinoless Double Beta Decay
$2\nu\beta\beta$	Two Neutrino Double Beta Decay
m.w.e	Meters Water Equivalent
AV	Acrylic Vessel
BD	1,2-butanediol
BisMSB	1,4-bis(2-methylstyryl)benzene
CMB	Cosmic Microwave Background
CMOS	Complementary Metal-Oxide-Semiconductor
CSS	channel software status
CTC	Crate Trigger Card
CUORE	Cryogenic Underground Observatory for Rare Events
DAQ	Data Acquisition
DB	Daughter Board
DC	Data Cleaning
DT	Dissolution Tank
ECA	Electronic Calibration

FEC	Front-End Card
GERDA	The GERmanium Detector Array
GSU	Gain Scaled Units
GT	Global Trigger
HV	High Voltage
HWT	Hot Water Tank
IO	Inverted Ordering
KATRIN	KArlsruhe TRitium Neutrino
LAB	Liquid Alkylbenzene
LH	Left-Handed
LSS	Large Scale Structure
MC	Monte Carlo
MTC/A+	Analogue Master Trigger Card
MTC/D	Digital Master Trigger Card
nhits	Number of PMT hits
NO	Normal Ordering
NRT	Nitric Rinse Tank
NWT	Nitric Waste Tank
OWL	Outward Facing PMT
PCA	PMT Calibration
PMT	Photomultiplier Tube

PMTIC	PMT Interface Card
PPO	2,5-diphenyloxazole
PSUP	PMT Support Structure
QCD	Quantum Chromodynamics
QFT	Quantum Field Theory
QHL	High Gain Long Integration Charge
QHS	High Gain Short Integration Charge
QLX	Low Gain Variable Integration Charge
RH	Right-Handed
RMS	Root-Mean Squared
SK	Super-Kamiokande
SM	Standard Model
SMS	Source Manipulator System
SNO	Sudbury Neutrino Observatory
SST	Supernatant Storage Tank
TAC	Time-to-Amplitude Converter
TeA	Telluric Acid
TeBD	Tellurium Butanediol
TRT	Thermal Rinse Tank
UI	Universal Interface
UPW	Ultra-Pure Water

URM	Umbilical Retrieval Mechanism
WEB	Wet End Breakdown
ZDAB	Zebra DAta Bank

Chapter 1

Introduction

Cosmic muons are produced in the particle interactions that occur within the Earth's atmosphere. They are produced with a wide range of energies, and they lose energy through ionising and radiative processes, until they eventually decay. Those with high energies can penetrate the Earth's surface, where the rate of energy loss is greater. Due to this effect, the number of muons reduces with depth, and only muons with very high energies will make it to the furthest depths.

Many particle physics experiments look for underground locations where the number of cosmic muons is significantly reduced due to the Earth's shielding properties. This is because cosmic muons produce a significant number of particles from the showers they induce as they travel through a medium. If these particles are produced within a particle physics detector, they act as a background to the physics searches. Although moving underground reduces the amount of these backgrounds, it does not remove them completely, and so they must be identified for removal from the data. This requires a strong understanding of the background.

One of the particles produced in the cosmic muon showers, that is a potential background, is the neutron. To understand this background, the yield of these cosmogenic neutrons has been measured by many experiments, covering a range of muon energies and using a variety of detecting materials. In this thesis, the analysis for measuring the cosmogenic neutron yield in water at the SNO+ experiment is presented. The 6011 m.w.e overburden at SNO+ means that SNO+ observes muons with an average energy of around 364 GeV.

As will be introduced in chapter 2, SNO+ is an experiment that is searching for neutrinoless double beta. This is a rare decay that could provide insight into how a neutrino gets its very small mass. This chapter will also give a description of the detector setup used by SNO+. One of the most important features of the detector are the photo-sensors that are able to detect even the smallest signals of light produced in particle interactions. SNO+ has three phases, defined by what the detector is filled with. The first phase was the water phase, the next and current phase is the scintillator phase, and the final phase is the tellurium phase in which SNO+ will begin its neutrinoless double beta decay search. Work was performed by the author on the effort to prepare for the tellurium phase, through the commissioning of the telluric acid purification plant. This is described in appendix B. This analysis uses the data taken during the water phase.

Chapter 3 explains in more detail the mechanism behind cosmogenic neutron production. This includes an in-depth breakdown of how muons lose energy through interactions as they propagate. During the water phase, neutrons in the detector are absorbed by hydrogen atoms that emit light when they de-excite, in the form of a 2.2 MeV gamma. This light is what makes the neutron a background, as well as being the signal used to identify them. A description of how these neutron producing interactions are modelled in simulation is also included here. This chapter concludes with a summary of the current experimental field of results from cosmogenic neutron yield measurements.

There are many moving parts involved in turning raw experimental data into data that is analysable. First, there needs to be a system of recording and storing any data that corresponds to a physics event. However, this data will not tell us anything about the physics without calibrating it. While calibration will help us understand our data, reconstruction will read and interpret the data, based on the distribution of light hitting the photo-sensors and the amount of light produced. This is all explained in chapter 4.

As there will be a mixture of particle events recorded, a list of event criteria is applied to the data in order to select the events we care about. The high-energy nature of muons causes them to produce a lot of light in the detector. This is used to identify muon events. On the other hand, the neutron signal is low energy and produces very little light. Again, this characteristic is used to identify these events, along with other requirements based on the time since the muon and the distance from the muon. These lists of criteria were created by Billy Liggins in [1] and are defined in chapter 5. Before events can be selected, this chapter outlines the role of run selection. Run selection is a step in the data processing chain, where the data is assessed on whether its quality is high enough for analysis. The author's role in this is presented in appendix A.

Events may be accidentally identified as a muon-induced neutron. These events are backgrounds to the cosmogenic neutrons, and must be removed from the data. Applying the cosmogenic neutron selection criteria to events outside each muon's time window gives a measurement of the number of these background events to expect. This and other contributions to the cosmogenic neutron backgrounds are discussed in chapter 6.

Due to the small amount of light produced by the neutron signal, it is very easy to miss events. Approximately only 50% of the neutron capture events will be seen by the detector, a number which is further reduced by the selection criteria. Missed neutrons are accounted for by the neutron selection efficiency, the focus of chapter 7. This depends on where the muon travels through the detector, so needs to be evaluated on an event-by-event basis. This chapter will present the method for doing this, and identifies and calculates any contributions to the uncertainty in the neutron selection efficiency. All methodology described in this section has been developed by the author for this analysis, with the idea that it may be used in any future analyses of the cosmogenic neutron yield at SNO+.

In chapter 8, the final result for the cosmogenic neutron yield is calculated. This chapter will also summarise how the uncertainty in the yield will be handled, with the dominant contribution arising from the use of simulations in determining the neutron selection efficiency. The final result is compared with the results from other experiments, and the conclusions are presented in chapter 9.

Chapter 2

SNO+ and the Search for Neutrinoless Double Beta Decay

As we learn more about the universe, we often come away with more questions. Particle physics is no different and experiments are often required to answer these questions. The neutrino was first postulated by Wolfgang Pauli in 1930 [2] as a solution to the energy conservation problem in beta decay, but it wasn't until 1956 when their existence was confirmed experimentally by Clyde Cowan and Frederick Reines [3]. Since this breakthrough in neutrino detection, a wide variety of neutrino physics experiments have been built with the aim of solving many of the unknowns we still have in neutrino physics. SNO+ is one neutrino experiment with the main goal of searching for neutrinoless double beta decay, a rare and never before observed decay which could unlock the nature of the neutrino.

This chapter aims to summarise our current understanding of the neutrino and the importance of searching for neutrinoless double beta decay. This will lead to an introduction of SNO+, including its physics goals, the experimental setup, and how SNO+ plans to search for neutrinoless double beta decay.

2.1 The Standard Model and Particle Mass

The world around us, including ourselves, is made up of matter, and is influenced by forces. The main constituents of matter are atoms. Each atom contains electrons orbiting a central nucleus that contains protons and neutrons. On an even smaller scale, the neutrons and protons are made up of particles known as quarks. These, along with the electron, are the fundamental particles, known as fermions. The different forces which act upon these fermions are transferred through force-carrying particles, known as bosons. The Standard Model (SM) of particle physics is a theory that aims to describe all fundamental particles and the interactions they undergo.

Particles have intrinsic properties that are used to define the different types. These properties include mass, charge and spin. In the SM, particles are categorised as fermions or bosons, based on their spin: fermions have half-integer spin, and bosons have integer spin. Fermions follow Fermi-Dirac statistics, which means they obey the Pauli exclusion principle. The exclusion principle forbids two fermions to occupy the same quantum state within a system. This means fermions within a system, such as an atom, cannot have the same energy and spin. On the other hand, bosons follow Bose-Einstein statistics, and have no such exclusion principle. Each fermion f has its own associated anti-fermion $\bar{f}$. Anti-fermions have the same mass as their fermion, but the quantum numbers such as charge and spin are reversed.

Bosons with spin-1 are called gauge bosons, and mediate the interactions between particles. The fundamental interactions are the electromagnetic, the weak and the strong interaction, and each interaction has its own gauge boson. The electromagnetic interaction occurs through the exchange of a photon between two charged particles. The $W^{\pm}$ and Z bosons are the exchange particles for the weak interaction, and the gluon mediates the strong interaction. All fermions can interact weakly, although not all can interact strongly.

Each fundamental force is described by a quantum field theory (QFT). For the strong force, this is called quantum chromodynamics (QCD). In QCD, the gluon will only couple to certain particles. A property known as colour charge is assigned to the particles in order to distinguish between those that can couple to gluons and those that cannot. Particles that have colour charge are named quarks, and particles with no colour charge are called leptons. There are six quarks (and six anti-quarks): up u (anti-up $\bar{u}$), down d (anti-down $\bar{d}$), strange s (anti-strange $\bar{s}$), charm c (anti-charm $\bar{c}$), top t (anti-top $\bar{t}$) and bottom b (anti-bottom $\bar{b}$). Each quark comes with three colour charges. The different colour charges are red, green and blue for quarks, and anti-red, anti-green and anti-blue for anti-quarks. Colour confinement requires that every particle be colourless. This means that quarks can never be isolated, but instead form bound states that are colourless, known as hadrons. A colourless state can be a combination of three quarks that each have a different colour: one red, one blue and one green (or one anti-red, one anti-blue and one anti-green). These particles are baryons, and examples of baryons include protons (uud) and neutrons (udd). The other combination of quarks that forms a colourless state is a quark-anti-quark pair. These are called mesons, and examples include pions and kaons.

As already stated, leptons are particles without colour charge. There are three negatively charged leptons, named: electron e^-, muon μ^- and tau τ^-. Since these are charged particles, they can interact through the electromagnetic interaction. Each of the three charged leptons form a pair with a neutral lepton, called a neutrino, where each particle in the pair shares a property known as lepton flavour. The neutral leptons paired with the electron, muon and tau are named the electron neutrino ν_e, the muon neutrino ν_μ and the tau neutrino ν_τ, respectively. Neutrinos are neutral particles that only interact through the weak interaction.

Leptons are assigned lepton numbers L, and lepton flavour numbers $L_i, i \in e, \mu, \tau$. All leptons have a lepton number of $+1$, while all anti-leptons have a lepton number of -1. Lepton flavour number is slightly more complicated in that it is equal to $+1$ for leptons of that flavour, -1 for anti-leptons of that flavour, and 0 for leptons or anti-leptons of another flavour. This is summarised in table 2.1. The conservation of lepton number, before and after an interaction, is a naturally

Lepton (anti-lepton)	L	L_e	L_μ	L_τ
$e^-(e^+)$	$+1(-1)$	$+1(-1)$	0	0
$\mu^-(\mu^+)$	$+1(-1)$	0	$+1(-1)$	0
$\tau^-(\tau^+)$	$+1(-1)$	0	0	$+1(-1)$
$\nu_e(\bar{\nu}_e)$	$+1(-1)$	$+1(-1)$	0	0
$\nu_\mu(\bar{\nu}_\mu)$	$+1(-1)$	0	$+1(-1)$	0
$\nu_\tau(\bar{\nu}_\tau)$	$+1(-1)$	0	0	$+1(-1)$

Table 2.1: Summary of the lepton numbers L and the lepton flavour numbers $L_i, i \in e, \mu, \tau$ for the electron e^-, muon μ^-, tau τ^-, electron neutrino ν_e, muon neutrino ν_μ and tau neutrino ν_τ, and their respective anti-particles e^+, μ^+, τ^+, $\bar{\nu}_e$, $\bar{\nu}_\mu$ and $\bar{\nu}_\tau$.

occurring symmetry in the Standard Model. While many interactions also conserve lepton flavour number, there are cases where this is broken.

A particle's spin is used to define a property called helicity. If a particle's spin projects in the direction of its momentum, the helicity is positive, whereas, if the projected spin is in the opposite direction to the particle's momentum, the helicity is negative. However, if the particle is travelling less than the speed of light, the direction of a particle's momentum depends entirely on the frame of reference it is being observed in. This makes the helicity dependent on the frame of reference, and not a fixed measure. Chirality is introduced to be a spin-related property that is invariant to the observer's reference frame. Chirality defines particles as being either left-handed (LH) or right-handed (RH). For massless particles that travel at the speed of light, chirality and helicity are equivalent, where RH particles have a positive helicity and LH particles have a negative helicity. Both LH and RH particles can partake in electromagnetic and strong interactions, which means all quarks and charged leptons having been observed in both chirality states.

However, the weak interaction will only couple to LH particles or RH anti-particles. Since neutrinos only interact through the weak interaction, only LH neutrinos and RH anti-neutrinos have been observed.

A Dirac mass term is a way of coupling LH and RH fermions to give them mass. Simply adding a Dirac mass term into the SM does not work as this mixes the LH and RH chiral states. This is a problem because it would break the chiral symmetry enforced by the weak interaction only coupling to LH fermions and RH anti-fermions. Instead, particles in the SM achieve mass through interactions with a scalar field, known as the Higgs field. This interaction is know as the Higgs mechanism, and produces an effective Dirac mass term for fermions, while preserving the chiral symmetry. The stronger a particle's coupling to the Higgs field, the more massive the particle is. The Higgs boson is the spin-0 boson associated with the Higgs field.

Whilst the Higgs mechanism works for most fermions in the SM, of which both LH and RH chiral states have been observed, neutrinos are unique. Since RH neutrino states have not been observed, it was assumed that they do not exist and the neutrino is massless. However, it has since been proven that neutrinos do have mass, and a mechanism to include this in the SM must be found.

2.2 Massive Neutrinos

As stated above, neutrinos in the SM were assumed to be massless. This was proven to be wrong after the observation of neutrino oscillations, a process in which a neutrino can change flavour. The changing of neutrino flavour means neutrino oscillation is a lepton flavour number violating process.

Neutrino oscillation was first proposed as a solution to the solar neutrino problem, a shortfall in the number of detected electron neutrinos emitted from the Sun [4], compared with the number expected [5]. The idea was that the electron neutrinos emitted from the Sun were changing flavour before reaching the Earth, where they were detected. If the detector is only searching for electron neutrinos, and is blind to other neutrino flavours, then this would explain the lack of electron neutrinos. Further deficits in the number of observed neutrinos were seen in atmospheric muon neutrinos, neutrinos produced by particle interactions in the Earth's atmosphere [6]. Following a similar principle, neutrino oscillation could also explain this anomaly.

Neutrino oscillations were eventually confirmed experimentally by the Super-Kamiokande (SK) experiment and the Sudbury Neutrino Observatory (SNO). SK demonstrated an angular dependence on the disappearing atmospheric muon neutrinos, in which the muon neutrinos coming from above showed less disappearance than those coming from below [7]. This was explained by neutrino oscillation because the muon neutrinos arriving from below had travelled through the Earth, over a much further distance, and were more likely to undergo oscillations than those that had arrived from above, only travelling a short distance from their creation in the atmosphere. SNO was able to measure the total neutrino flux from the Sun, regardless of neutrino flavour. From this method, they were able to show that the electron neutrinos were oscillating into muon or tau neutrinos during their journey from the centre of the Sun to Earth [8].

Since neutrinos only interact weakly, they are only observed as one of three possible flavour eigenstates. As already revealed, these flavour eigenstates are ν_e, ν_μ and ν_τ. Neutrino mixing is the idea that the flavour eigenstates are linear combinations of three mass eigenstates. These mass eigenstates are denoted by ν_1, ν_2 and ν_3, each with mass m_1, m_2 and m_3, respectively. Neutrino mixing is described by

$$|\nu_\alpha\rangle = \sum_{i=1}^{3} U^*_{\alpha i}|\nu_i\rangle \qquad \alpha = e, \mu, \tau. \tag{2.1}$$

The components $U_{\alpha i}$ are defined in the unitary Pontecorvo-Maki-Nakagawa-Sakata (PMNS) matrix U_{PMNS}. Assuming three neutrino flavours, this is

$$U_{\text{PMNS}} = \begin{pmatrix} c_{12}c_{13} & s_{12}c_{13} & s_{13}e^{-i\delta_{CP}} \\ -s_{12}c_{23} - c_{12}s_{13}s_{23}e^{i\delta_{CP}} & c_{12}c_{23} - s_{12}s_{13}s_{23}e^{i\delta_{CP}} & c_{13}s_{23} \\ s_{12}s_{23} - c_{12}s_{13}c_{23}e^{i\delta_{CP}} & -c_{12}s_{23} - s_{12}s_{13}c_{23}e^{i\delta_{CP}} & c_{13}c_{23} \end{pmatrix}, \tag{2.2}$$

where $c_{ij} = \cos(\theta_{ij})$ and $s_{ij} = \sin(\theta_{ij})$. The mixing parameters are given by the mixing angles θ_{ij}, where $0 \leq \theta_{ij} \leq \pi/2$, and the CP violating phase δ_{CP}, where $0 \leq \delta_{CP} \leq 2\pi$ [9].

In neutrino oscillation, the propagation of the mass eigenstates leads to a change in the mixing that results in a change in flavour. This change in mixing is only possible if the mass eigenstates propagate at different frequencies. For this to be satisfied, the mass eigenstates must each have a unique mass (i.e. $m_1 \neq m_2 \neq m_3$), which is only allowed if at least two of the mass eigenstates have a non-zero mass. Therefore the observation of neutrino oscillation requires neutrinos to be massive. However, neutrino oscillation experiments are only sensitive to neutrino mass through the mass splittings $\Delta m^2_{ij} = m^2_i - m^2_j$, which they are able to measure. This means that neutrino oscillation experiments cannot measure the neutrino mass directly.

The neutrino mass still remains an unknown. The KArlsruhe TRitium Neutrino (KATRIN) experiment is currently working to measure the neutrino mass through direct measurements. The experiment precisely measures the energy of the electron produced in the β decay of tritium. Over time, this builds up an energy spectrum for the decay, and the kinematic endpoint can be taken as the point where the spectrum ends. The shape of the spectrum at the endpoint is affected by neutrino mass, and measuring the amount of shape distortion is used to calculate the neutrino mass. While KATRIN has not yet measured the neutrino mass, it has been able to set an upper limit of $m_\nu < 0.45\,\mathrm{eV}$ (90% CL) on the neutrino mass m_ν [10].

Further limits to the neutrino mass scale have been set using cosmological data, where the sum of the neutrino masses can be measured. This is done using measurements of the cosmic microwave background (CMB) and measurements of large scale structures (LSS). The current limit provided by CMB measurements is $\sum m_\nu < 0.26\,\mathrm{eV}$ (95% CL) [11]. The current limit provided by LSS measurements is $\sum m_\nu < 0.13\,\mathrm{eV}$ (95% CL) [12].

Since the discovery of neutrino oscillations, massive neutrinos must be incorporated into the SM. The limits set by direct measurements of the neutrino mass and cosmological data show that the mass scale of the neutrino is less than eV-scale. For context, the electron is the lightest charged fermion in the SM with a mass of $0.511\,\mathrm{MeV}$. This means any model that incorporates neutrino mass into the SM must also explain why the neutrinos are so much lighter than the other fermions.

Since neutrinos were assumed to be massless because of a lack of a RH state, one method of giving SM neutrinos mass is to simply add in a RH neutrino. As with the other fermions, the interaction with the Higgs field provides a Dirac mass term m_D for the neutrino. However, this method fails to account for the incredibly small neutrino mass.

Another way of introducing mass to the SM neutrino is through adding a Majorana mass term. In the SM, all fermions are Dirac fermions, where the particle and the anti-particle are two distinct particles. There also exists the concept of Majorana fermions, particles that are their own anti-particle [13]. Since a particle and anti-particle have opposite charges, charged fermions are forbidden from being Majorana. However neutral particles, such as neutrinos, are candidates to be Majorana particles. The Majorana mass term couples a fermion with its anti-fermion. In order to preserve symmetry in the SM, this is only allowed for RH Majorana neutrinos. The result is a LH neutrino with a mass of $m_\nu \approx m_D^2/M_R$ and a RH neutrino with a mass of M_R. For the LH neutrino mass to be small, as compatible with observation, the mass of the RH neutrino must be large. For this reason, this is called the see-saw mechanism [14].

2.3 Neutrinoless Double Beta Decay

The term isotope refers to atoms with the same number of protons, but a different number of neutrons. Within a family of isotopes, the most stable isotope is the one in which the least amount of energy is needed to bind the nucleus together. Instability of an isotope can be caused by the nucleus containing too many neutrons or too many protons. Beta decay occurs when an unstable nucleus converts a neutron into a proton, or vice versa, in order to become stable. A beta particle $\beta^\pm$ refers to the electron or positron (anti-particle of the electron) emitted by a nucleus during beta decay. Equations 2.3 and 2.4 respectively show β^- and β^+ decay, where n is a neutron and p is a proton.

$$n \rightarrow p + \beta^- + \bar{\nu}_e \tag{2.3}$$

$$p \rightarrow n + \beta^+ + \nu_e \tag{2.4}$$

Also emitted in β^- decay is an electron anti-neutrino $\bar{\nu}_e$, or an electron neutrino ν_e in the case of β^+ decay. The energy released in this decay is known as the Q-value and is carried away by the beta particle and neutrino. Each beta decay has its own Q-value that is constant for that decay.

There is the possibility for some isotopes to decay into a more stable isotope through the emission of two beta particles, in the form of two simultaneous beta decays [15]. This process is known as two neutrino double beta ($2\nu\beta\beta$) decay and is represented in figure 2.1a. This only occurs if β decay is energetically forbidden, but $2\nu\beta\beta$ decay is energetically allowed. A decay is energetically forbidden if its decay product is heavier than itself. The first observation of $2\nu\beta\beta$ decay of ^{130}Te with a half-life of $T_{1/2}^{2\nu\beta\beta} = 1.4 \times 10^{21}$ yr was made in 1950 [16].

Neutrinoless double beta ($0\nu\beta\beta$ decay) decay is a postulated decay in which two neutrons are transformed into two protons and two beta particles are emitted from the nucleus with no associated neutrinos, as shown in figure 2.1b. The two electrons in the final state means that $0\nu\beta\beta$ decay is a lepton number violating process. $0\nu\beta\beta$ decay is possible for Majorana neutrinos, where the transmutation of neutrino to anti-neutrino allows for two simultaneous beta decays with no neutrinos in the final state [17]. Observing $0\nu\beta\beta$ decay would provide strong evidence towards neutrinos being Majorana particles, a key ingredient of the see-saw mechanism.

The event rate of $0\nu\beta\beta$ decay is given by

$$\Gamma_{0\nu\beta\beta} = G_{0\nu}|M_{0\nu}|^2|m_{\beta\beta}|^2, \tag{2.5}$$

where $G_{0\nu}$ is the phase-space factor, $M_{0\nu}$ is the nuclear matrix element, and $m_{\beta\beta}$ is the effective neutrino mass. These quantities are defined below.

The effective neutrino mass $m_{\beta\beta}$ is the sum of the neutrino masses weighted by U_{PMNS}, as shown in

$$m_{\beta\beta} = \left| \sum_{k=1}^{3} m_k U_{ek}^2 \right|. \tag{2.6}$$

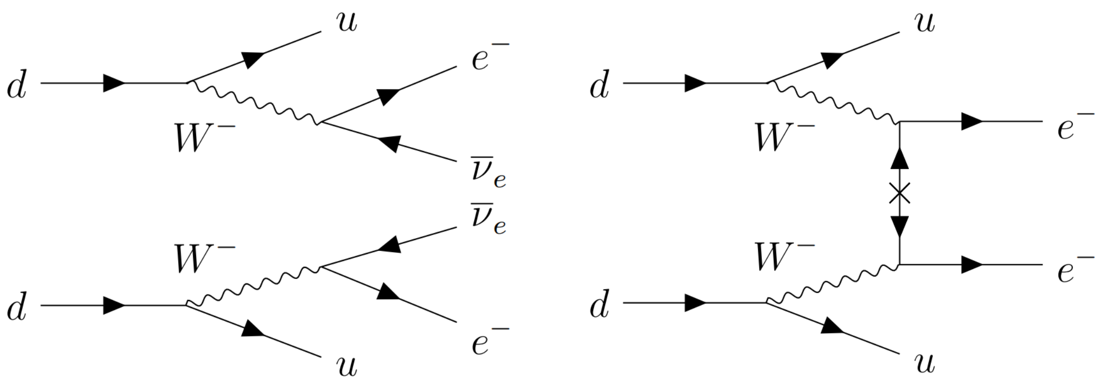

(a) $2\nu\beta\beta$ decay.

(b) $0\nu\beta\beta$ decay.

Figure 2.1: Quark-level Feynman diagrams for two neutrino (left) and neutrinoless (right) double beta decay.

The ordering of the neutrino mass eigenstate's masses will affect the effective neutrino mass. There are two combinations of mass ordering: normal ordering (NO) defined as $m_1 < m_2 < m_3$, or inverted ordering (IO) defined as $m_3 < m_1 \approx m_2$. The mass ordering is currently unknown, and is being pursued by neutrino oscillation experiments.

The phase-space factor $G_{0\nu}$ represents all possible final state configurations of the two electrons in $0\nu\beta\beta$ decay, constrained by the conservation of energy and momentum. Since all the energy released in the decay will be carried away solely by the two electrons, this depends heavily on the decay's Q-value. Interactions between the released electrons and the protons within the nucleus must also be accounted for in the phase-space factor. This creates a dependence on the proton number of the isotope Z. The phase factors have been calculated accurately for many isotopes that can undergo $0\nu\beta\beta$ decay [18].

The nuclear matrix element $M_{0\nu}$ gives the probability for the transition from the two neutrons in the initial state to the two protons and two electrons in the final state, within a given nuclear structure. Since the process takes place in the nucleus, this is affected by how the nucleus is configured. This leads to dependencies on the type of isotope and the model which describes the nuclear structure. The neutrino propagator means that there is also a dependency on neutrino properties,

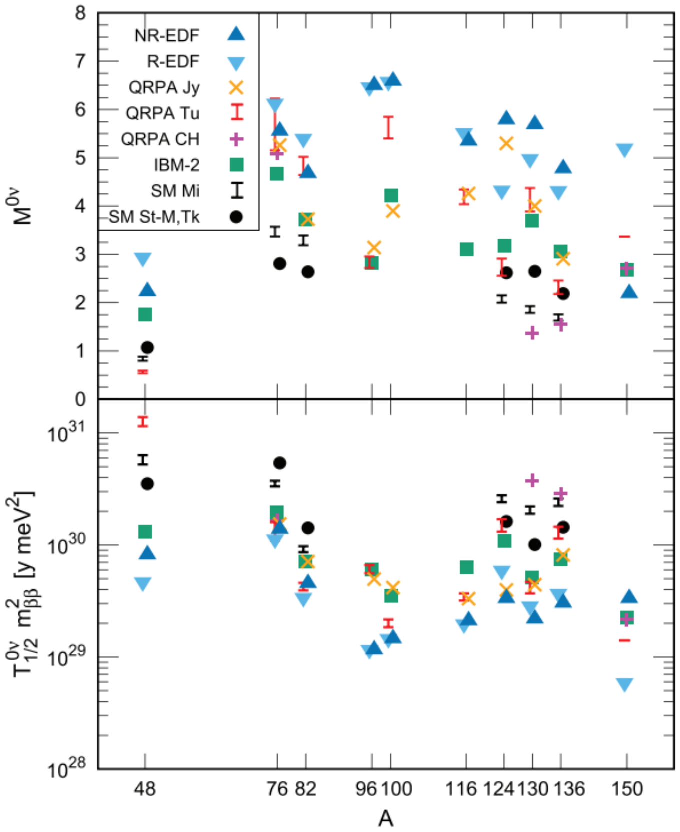

Figure 2.2: The above panel shows the nuclear matrix elements for the candidate isotope mass numbers A, calculated using different nuclear models. Below this gives the associated $0\nu\beta\beta$ decay half-lives, scaled by the unknown effective neutrino mass [19].

such as the unknown neutrino mass ordering. The nuclear matrix element is based solely on theoretical calculations, and has been calculated for different isotopes, using different models. The differences in the models leads to a wide variation in the nuclear matrix element, which in turn leads to a large uncertainty in the $0\nu\beta\beta$ decay rate calculation. Figure 2.2 shows how the different models used to calculate the nuclear matrix elements for each isotope leads to a large uncertainty in the $0\nu\beta\beta$ decay rate [19].

There are many experiments that have searched and are searching for $0\nu\beta\beta$ decay, using a range of isotopes. Only isotopes that are capable of $2\nu\beta\beta$ decay are candidates for $0\nu\beta\beta$ decay. Theoretically there are almost 70 isotopes that have the potential to undergo $0\nu\beta\beta$ decay, however a list of only 9 isotopes is generally considered for experimental searches due to availability and Q-value [17]. This list is given in table 2.2, including some of the key properties that are considered when

Isotope	Q-value [MeV]	δ_{nat} [%]	$T_{1/2}^{2\nu\beta\beta}$ [yr]
^{48}Ca	4.27	0.187	6.4×10^{19}
^{76}Ge	2.04	7.61	1.926×10^{21}
^{82}Se	3.00	8.73	8.60×10^{19}
^{96}Zr	3.36	2.80	2.35×10^{19}
^{100}Mo	3.03	9.63	7.12×10^{18}
^{116}Cd	2.81	7.49	2.63×10^{19}
^{130}Te	2.53	34.08	7.71×10^{20}
^{136}Xe	2.46	8.87	2.165×10^{21}
^{150}Nd	3.37	5.6	9.34×10^{18}

Table 2.2: The candidate isotopes for $0\nu\beta\beta$ decay experiments, along with their Q-values [17], natural abundance δ_{nat} [20] and $2\nu\beta\beta$ decay half-life $T_{1/2}^{2\nu\beta\beta}$ [17].

deciding on which isotope to use in a $0\nu\beta\beta$ decay search. The experimental signature for $0\nu\beta\beta$ decay is a peak in the summed electron energy, at the Q-value of the decay. This means that the decay's Q-value dictates the energy region of interest for the experiment. Deciding an appropriate Q-value is important because the background contribution to this region should be minimised. Also, the $0\nu\beta\beta$ decay rate increases with Q-value meaning higher Q-values leads to more decays [17]. A high natural abundance of the isotope means less money and time to be spent on enrichment. The isotope's half-life for $2\nu\beta\beta$ decay is also an important consideration as this controls the amount of $2\nu\beta\beta$ decays which are an intrinsic background to $0\nu\beta\beta$ decay.

The current and future experimental landscape for $0\nu\beta\beta$ decay searches is a diverse and well-populated one. The GERmanium Detector Array (GERDA) experiment set the half-life limit for ^{76}Ge to $T_{1/2}^{0\nu\beta\beta} > 1.8 \times 10^{26}$ yr [21]. The Cryogenic Underground Observatory for Rare Events (CUORE) experiment set the half-life limit for ^{130}Te to $T_{1/2}^{0\nu\beta\beta} > 2.2 \times 10^{25}$ yr [22]. More recently, KamLAND-Zen set the half-life limit for ^{136}Xe to $T_{1/2}^{0\nu\beta\beta} > 3.8 \times 10^{26}$ yr. This set the best limit on the effective neutrino mass to be $m_{\beta\beta} < (28 - 122)$ meV [23]. These results are represented as limits on the effective neutrino mass in figure 2.3.

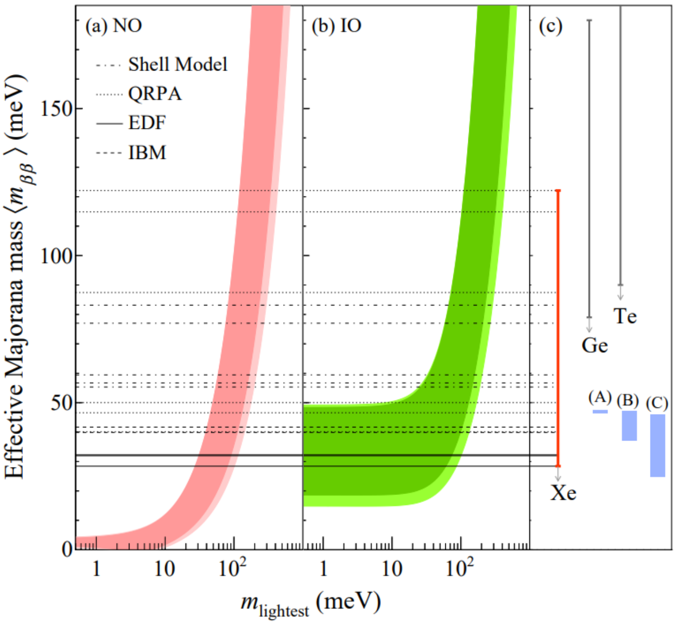

Figure 2.3: The effective neutrino mass as a function of the mass of the lightest neutrino m_{lightest} [23]. The shaded regions are predictions made using the best-fit values from neutrino oscillation experiments. Panel (a) is for normal ordering (NO) and panel (b) is for inverted ordering (NI). Panel (c) shows the limits set by GERDA (^{76}Ge) [21], CUORE (^{130}Te) [22], and KamLAND-Zen (^{136}Xe) [23]. (A), (B) and (C) represent theoretical predictions, and the dot-dashed lines are the different models used for the nuclear matrix element calculations.

2.4 The SNO+ Experiment

The introduction of neutrinoless double beta decay in the previous section brings us to SNO+, an experiment that will search for this rare decay. In section 2.4.1, this and other physics goals of SNO+ are presented. SNO+ is a multi-purpose neutrino experiment that makes use of the detector used by the SNO experiment. The main infrastructure of the detector, including all of its components, is described in section 2.4.2, and section 2.4.3 will outline the different phases of SNO+ and describe how they are used to achieve the physics goals.

2.4.1 Physics Goals

The SNO+ experiment has been set up with the aim of searching for $0\nu\beta\beta$ decay, introduced in section 2.3. In $2\nu\beta\beta$ decay, two neutrons are simultaneously converted into two protons with the resulting energy being carried away among the two electrons and two neutrinos produced. Since some of the energy is carried away by the neutrinos, the sum of energies of the two electrons results in a spectrum up to the Q-value of the decay. In $0\nu\beta\beta$ decay, by definition, no neutrinos are found in the final state, leaving the energy to be shared solely between the electrons. The result of this is a peak in the summed energies of the electrons, at the Q-value of the decay, which SNO+ aims to find.

As well as the $0\nu\beta\beta$ decay programme, SNO+ hosts a variety of other physics searches. Already published results have included searches for solar neutrinos [24, 25]; reactor antineutrinos [26, 27]; and nucleon decay [28, 29].

2.4.2 The SNO+ Detector

SNO+ has inherited the detector infrastructure used by the SNO experiment. The detector is located in SNOLAB, an underground laboratory in Sudbury, Canada. At this location, there is a flat rock overburden of 2070 m, or 6011 meters of water equivalent (m.w.e).

The SNO+ detector is made up of many different components. The acrylic vessel (AV) is used to house the detecting medium. It is a spherical shell of thickness 5.5 cm and radius 6 m. At the top of the AV is a 7 m high cylindrical “neck” that creates a path from the AV to the deck above. Surrounding the AV are 9362 inward facing photomultiplier tubes (PMTs), all directed towards the centre of the AV. These PMTs are each surrounded by a light concentrator and mounted to the PMT support structure (PSUP), a frame of radius 8.5 m that is concentric with the AV. Also mounted to the PSUP are 91 outward-facing PMTs (OWLs), without light concentrators, used for cosmic muon identification. This is all contained within a cavity filled with ultra-pure water (UPW). A network of hold-up and hold-down ropes are used to keep the AV in a stable position within the surrounding UPW.

The detector electronics, explained in section 4.1.1, are housed above the detector, with a separating platform. The top of the neck is sealed by the universal interface (UI). Mounted on the UI are four neck PMTs which are directed down the neck.

Photomultiplier Tubes

The PMTs are used to detect light produced in particle interactions with a high sensitivity. They consist of a photocathode and an electron multiplier which are stored within a vacuum filled, low-activity glass casing. When a photon is incident on the photocathode, an electron is released via the photoelectric effect. The electron is then accelerated through a series of dynodes with an applied voltage, the electron multiplier component. At each dynode, the electron produces multiple secondary electrons, causing the number of electrons to increase at each dynode. The result is an amplified signal that is sent to the signal processing systems, described in section 4.1. SNO+ uses the Hamamatsu R1408 8" PMTs that were used in the SNO experiment, with repairs and replacements made during the re-commissioning of the detector. With the 27 cm diameter aluminium light concentrators surrounding each PMT, the PMTs give a total detector coverage of $\sim 54\%$.

Cover Gas System

The radon isotopes ^{220}Rn and ^{222}Rn are produced in the decay chains of the ^{232}Th and ^{238}U, respectively, that naturally occur in the rock surrounding SNO+. In the decay chain of ^{232}Th, ^{212}Bi and ^{208}Tl are produced. A daughter of ^{222}Rn is the short-lived ^{214}Bi. These isotopes are all potential backgrounds to physics searches, and the cover gas systems have been developed to reduce these backgrounds.

There are two cover gas systems, installed in SNO+, designed to reduce the amount of radon contamination in the detector. The first is the cavity cover gas system which uses nitrogen gas to flush the space between the UPW shielding and the cavity roof. The second, installed in September 2018, is the AV cover gas system. This operates in the same way as the cavity cover gas system but, in the volume above the liquid in the neck. More details on the cover gas systems at SNO+ can be found in [30].

Calibration Systems

Calibration is the fundamental way of understanding a detector. The SNO+ detector has instrumentation in place for performing many methods of *in-situ* calibrations. One calibration method involves deploying a source within the AV, or between the AV and the PSUP. The calibration source can be positioned at different points in the detector using the source manipulator system (SMS). The SMS, as pictured in figure 2.4, is made up of an umbilical which runs through the neck, and attaches directly to the source through the source interface. Running through the umbilical are power and signal cables, and gas lines, and the source interface allows the connections between these lines and the source. The umbilical is moved along the vertical axis through a system of pulleys contained within the umbilical retrieval mechanism (URM). The URM is located in a clean room, above the UI. The source can be moved away from the vertical axis, in two directions, using two pairs of side ropes. Each side rope is attached to the AV at one end, and attached to a motor box, above the UI, at the other. The side ropes run through a connection to the umbilical which allows for the movement of the source, driven by the motor boxes. For source deployment into the volume between the AV and the PSUP, there are six calibration guide tubes [30].

Details on the calibration methods used during the water phase of SNO+ will be presented in section 4.2.

2.4.3 The Phases of SNO+

SNO+ has three planned operating phases which define the medium that fills the AV. The three phases are: water, scintillator and tellurium. The water phase ran from May 2017 until July 2019. The scintillator phase is the current phase of SNO+, which commenced in April 2022. When SNO+ enters its tellurium phase, the search for $0\nu\beta\beta$ decay will begin. This section will describe each phase in more detail.

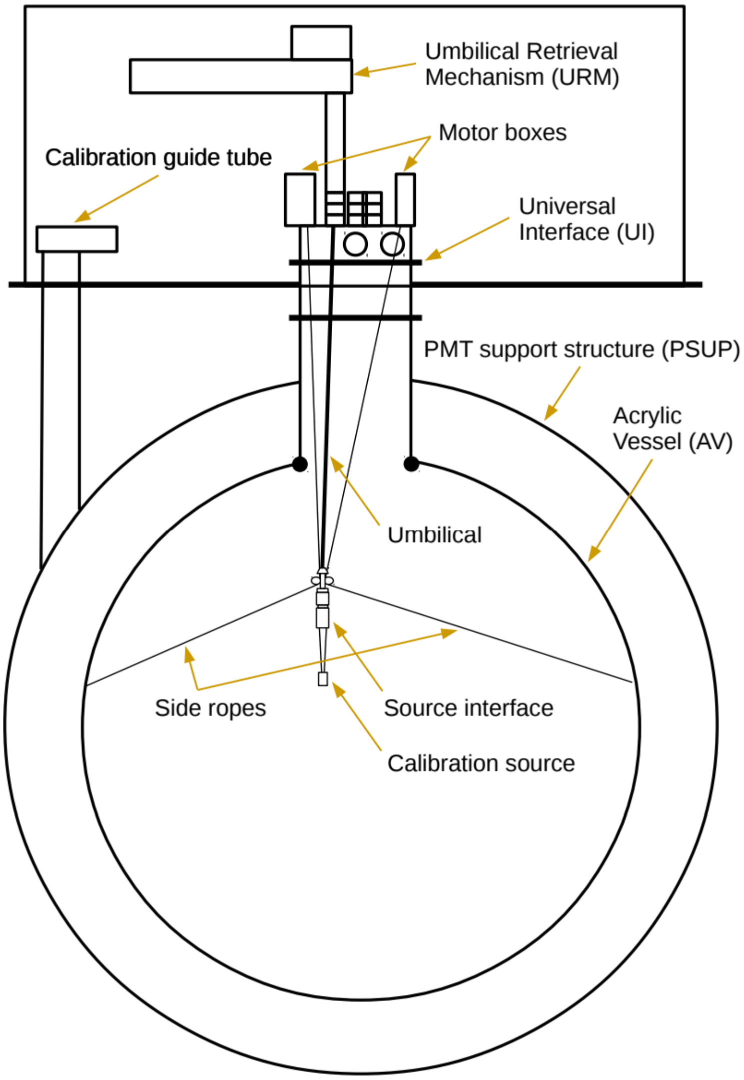

Figure 2.4: An illustration of the source manipulator system (SMS), which has been designed for the deployment of calibration sources at different positions in the detector [30].

Water Phase

For the water phase, the AV was filled with 0.9 kt of UPW. The purpose of this phase was the re-commissioning of the detector and its electronics. Additionally, the radon level in UPW is significantly less than in the surrounding cavity air, allowing for the suppression of radon. Further reduction to the radon levels came from the installation of the cover gas systems installed during this phase. An evaluation of the background contribution from the different components of the detector was made.

During this phase, SNO+ was used as a water Cherenkov detector and was able to collect physics data. Due to the refractive index of water, light travels through water at around three quarters of the speed of light in a vacuum. This allows charged particles to travel faster than the speed of light in water, as they are unaffected by the refractive index. Charged particles moving faster than the speed of light through water emit electromagnetic radiation, called Cherenkov radiation. The angle θ at which the radiation is emitted, is related to the speed of the particle v_p through

$$\cos\theta = \frac{c}{nv_p}, \tag{2.7}$$

where n is the refractive index of the material the particle is traversing, and c is the speed of light in a vacuum. For SNO+'s water phase, this was the mechanism used for detecting particles. The continuous emission of this radiation as the particle is moving creates a cone of light with an apex of θ. Determining the size and the direction of the light cone provides information about the particle's position, direction and speed.

The threshold velocity for a particle to produce Cherenkov radiation is $v_{th} = c/n$. Using this, the threshold kinetic energy of a particle of mass m can be derived to give

$$E_{th} = \left(\frac{1}{\sqrt{1-1/n^2}} - 1\right) mc^2. \tag{2.8}$$

For a muon in water ($n = 1.33$), this threshold energy is around 55 MeV.

Scintillator Phase

Scintillators of a wide variety are commonly used for the detection of particles. Charged particles, that are produced in particle interactions, ionise and excite the atoms of the scintillator. Light is produced isotropically when the excited atoms de-excite. This scintillation light can be detected by the PMTs and used to identify the particle type and location in the detector. The advantages of using a scintillator detector include the greater light yield produced by the scintillator, compared with water. This allows SNO+ to probe down to lower energy thresholds with an improved energy resolution.

When selecting a scintillator there are many important factors to consider including the yield, the wavelength of the scintillation light, the compatibility with the detector materials, complexity of synthesis, and environmental impact. The liquid scintillator added to the AV for the scintillator phase is a mixture of the solvent liquid alkylbenzene (LAB), and the fluor 2,5-diphenyloxazole (PPO). A second fluor, 1,4-bis(2-methylstyryl)benzene (BisMSB), was also added during the scintillator phase. While the purpose of the PPO is to increase the light yield of the scintillator, the BisMSB is added to shift the wavelength of the scintillation light to longer wavelengths. At these longer wavelengths, the PMTs have a greater detection efficiency (420 nm). This particular “cocktail” was chosen due to its compatibility with the AV and a light yield that is competitive with other liquid scintillator based experiments. The safety and simplicity of the cocktail were also factors in deciding the cocktail [31].

Tellurium Phase

The final phase is the tellurium phase in which SNO+ will begin its search for $0\nu\beta\beta$ decay. The isotope ^{130}Te has been chosen as it is known to undergo $2\nu\beta\beta$ decay, making it a candidate for $0\nu\beta\beta$ decay. Among the other candidate isotopes, ^{130}Te has one of the longest $2\nu\beta\beta$ decay half-lives. This reduces the number of $2\nu\beta\beta$ decay events, a background to $0\nu\beta\beta$ decay searches. Further to this, ^{130}Te has the highest natural abundance of all the candidate isotopes, shown in table 2.2. This makes enrichment unnecessary which, on a tonne-scale, saves a great cost.

The Q-value for $2\nu\beta\beta$ with ^{130}Te is 2.53 MeV [17]. The β decay Q-value of ^{214}Bi is 3.270 MeV. This is greater than the $2\nu\beta\beta$ decay Q-value for ^{130}Te, meaning that the $0\nu\beta\beta$ decay signal will fall within the β decay spectrum of ^{214}Bi. This increases the need for a high radio-purity, along with effective background tagging [30].

The scintillator will be initially loaded with 1.3 tonnes of ^{130}Te, yielding a concentration of 0.5%. In order to achieve the required radio-purity, telluric acid (TeA) is purified in the TeA purification plant prior to loading. The TeA is then dissolved in water and transferred to the TeBD synthesis plant, where it is heated with 1,2-butanediol (BD) to form tellurium butanediol (TeBD), which is soluble in LAB. Calibration work was completed by the author as part of the TeA plant commissioning. This is described in further detail in appendix B.

2.5 Chapter Summary

The purpose of this chapter has been to introduce and motivate the SNO+ experiment. The main goal of SNO+ is to search for $0\nu\beta\beta$ decay, a rare decay which could lead to insight into how neutrino mass is generated.

The motivation behind SNO+ began with an introduction to the SM, a fundamental theory of particle physics. Here, the interaction with the Higgs boson was stated as the mechanism in which most particles achieve mass. However, due to the absence of an observed RH neutrino, the neutrino was assumed to be massless. The discovery of neutrino oscillations proved that neutrinos actually do have mass, and the SM needed to be adapted to accommodate this observation.

This brings us to Majorana neutrinos, the idea that the neutrino and the antineutrino are the same. This provides a way of introducing neutrino mass to the SM that allows for the incredibly small neutrino masses. One way of probing whether neutrinos are Majorana is through $0\nu\beta\beta$ decay searches. While many experiments have already searched for this decay using a variety of candidate isotopes, SNO+

hopes to use the isotope ^{130}Te to produce world-leading half-life sensitivities for $0\nu\beta\beta$ decay.

Also introduced in this chapter was a detailed description of the detector set-up, including the calibration systems, and the different phases of SNO+. SNO+ is currently in its scintillator phase, and will not begin its search for $0\nu\beta\beta$ decay until it enters its tellurium phase. Before the scintillator phase, there was a water phase in which the detector was filled only with UPW. The purpose of this phase was to re-commission the detector after it was inherited from the SNO experiment. However, many high quality physics analyses have been made using the water phase data. This thesis provides a further water phase analysis in the measurement of the cosmic muon-induced neutron yield, the theory behind which is introduced in the next chapter.

Chapter 3

Cosmogenic Neutrons

The previous chapter introduced different types of particles, including muons. This chapter introduces cosmic muons, high-energy muons produced in the atmosphere. Details about how the muons lose energy will be provided which leads on to cosmogenic neutrons. These are neutrons produced by cosmic muons, and are a source of background for many particle physics experiments. Measuring the number of cosmogenic neutrons is the aim of this thesis, as motivated at the end of this chapter.

3.1 Cosmic Muons

In 1912, Victor Hess performed an experiment in which he measured the rate of ionisation of the air at different altitudes. This ionisation was believed to be caused by γ radiation from radioactive elements in the Earth's crust. If this hypothesis was true, the ionisation rate would be expected to decrease as altitude increases. After several balloon trips, he found that the ionisation rate increased with altitude, concluding that there must be some high energy radiation entering the atmosphere from above [32]. This radiation later became known as cosmic rays, and experiments have since determined many of its properties.

Cosmic rays are high energy particles that travel through space, ranging in energies from non-relativistic to ultra-relativistic. They are predominantly made up of protons, but also include nuclei such as helium, electrons, positrons and anti-

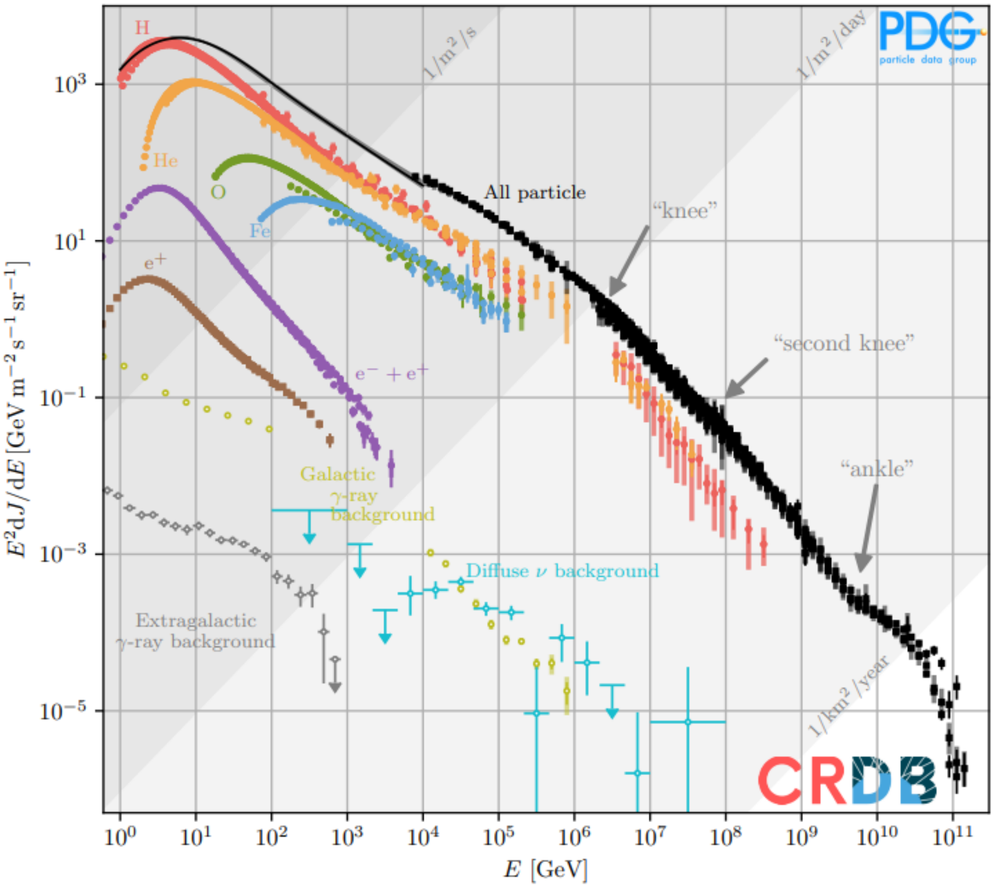

Figure 3.1: The energy spectrum of cosmic rays [33].

protons. There are many candidates for the origin of cosmic rays, such as remnants of supernovae, active galactic nuclei, pulsars, and many more. Figure 3.1 shows the energy spectrum of cosmic rays. Above the "knee" the incoming direction of the cosmic rays is approximately isotropic, but around and below the knee the distribution of sources and Galactic magnetic fields can cause small variations in the arrival direction [33].

When cosmic rays travel through the Earth's atmosphere, secondary particles are produced in interactions with the nuclei in air. The secondary particles go on to interact or decay, producing more particles which form cascades of particles known as air showers. Most secondary particles are charged ($\pi^{\pm}$) and neutral (π^0) pions. If the charged pions have enough energy, they will interact with the nuclei in the atmosphere, resulting in the hadronic component of the cosmic ray shower, before decaying via

$$\pi^{\pm} \rightarrow \mu^{\pm} + \overset{(-)}{\nu}_{\mu}. \tag{3.1}$$

The branching ratio of this decay is 100%, so all charged pions decay this way. The neutral pions decay into a pair of photons via

$$\pi^{0} \rightarrow \gamma\gamma. \tag{3.2}$$

The photons undergo pair production to create electron-positron pairs, inciting the electromagnetic component of the shower. Charged kaons are also a product of cosmic ray interactions in the atmosphere which decay via

$$K^{\pm} \rightarrow \mu^{\pm} + \overset{(-)}{\nu}_{\mu}, \tag{3.3}$$

with a branching ratio of 63.5% [34]. The muons produced in the decays of the charged mesons form the muonic component of the shower.

Muons generated in the cosmic ray-induced showers are called cosmic muons, and are typically produced around $10 - 15\,\mathrm{km}$ above the Earth's surface. Muons have a lifetime of $2.2\,\mu\mathrm{s}$ before decaying via

$$\mu^{\mp} \rightarrow e^{\mp} + \bar{\nu}_{e} + \overset{(-)}{\nu}_{\mu}. \tag{3.4}$$

The electron produced in muon decay is sometimes referred to as a Michel electron. For the speed that muons travel at ($\sim 0.995c$), they should only make it around $700\,\mathrm{m}$ before decaying. This means they should decay before reaching the Earth's surface. Time dilation is a product of special relativity in which time moves at different rates, depending on the frame of reference of the observer. A result of this is that moving clocks appear to run slower. This has the following effect on particle lifetime

$$\tau = \frac{\tau_0}{\sqrt{1 - (v/c)^2}}, \tag{3.5}$$

where v is the velocity of the particle, τ_0 is the lifetime of the particle at rest, and τ is the lifetime of the particle measured in the laboratory frame. Because muons travel close to the speed of light, their lifetime to an observer on Earth appears longer [35]. This means that muons can make it to the Earth's surface before decaying, with some reaching below the surface. Muons can arrive at the surface of the Earth from different directions but, since a higher incidence angle means a longer time of flight, most muons arrive from more vertical directions.

Muons lose energy through either ionisation or radiative processes, depending on their energy. Muons with lower energies tend to lose energy through ionisation, the interaction with electrons in atoms which causes the atoms to lose electrons. At higher energies, radiative processes become the dominant forms of energy loss. Figure 3.2 shows the radiative processes via which muons lose energy: bremsstrahlung, e^-e^+ pair production, and photonuclear processes [36]. Bremsstrahlung is the release of energy, in the form of radiation, when a muon is decelerated by the electric field of a nucleus. Pair production is the creation of an electron-positron pair, where, if the muons have enough energy, some of the muon's energy is used for this process in the presence of the electric field of a nucleus. Photonuclear processes are interactions with a nucleus causing the production of hadrons.

The average rate of muon energy loss is described by

$$-\frac{dE}{dx} = a(E) + b(E)E, \tag{3.6}$$

where E is the muon energy, $a(E)$ is the energy dependent contribution to the energy loss through ionisation, and $b(E)$ is the energy dependent contribution to the energy loss through radiative processes. The critical energy $\epsilon \equiv a/b$ is the energy above which radiative processes become the dominant form of muon energy loss. In rock, this is approximately 500 GeV [37].

Cosmic muons with high enough energies can penetrate the Earth's crust. As muons travel further through the Earth's crust the energy diminishing processes, discussed above, cause the muons to slow down until they eventually decay. This

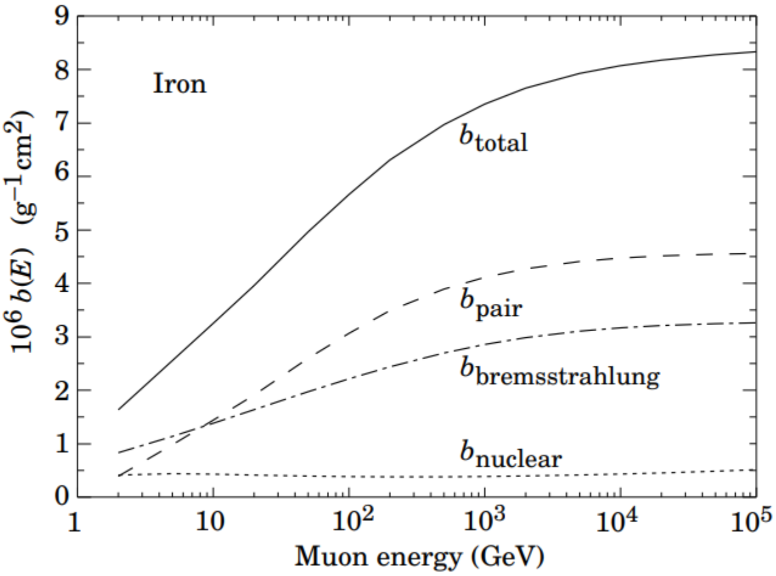

Figure 3.2: The contributions to muon energy loss in iron due to the radiative processes: bremsstrahlung, production of e^-e^+ pairs and photonuclear interactions [36].

means that the muon flux decreases as we go deeper underground. The muon intensity I, as a function of vertical depth h_0 and the direction from which the muons arrive θ, is given by

$$I(\theta, h_0) = \left(I_1 e^{-h_0 \sec\theta/\lambda_1} + I_2 e^{-h_0 \sec\theta/\lambda_2}\right) \sec\theta \tag{3.7}$$

The parameters $I_1 = (8.60 \pm 0.53) \times 10^{-6}\,\text{cm}^{-2}\text{s}^{-1}$, $I_2 = (0.44 \pm 0.06) \times 10^{-6}\,\text{cm}^{-2}\text{s}^{-1}$, $\lambda_1 = 0.45 \pm 0.01\,\text{km.w.e}$ and $\lambda_2 = 0.87 \pm 0.02\,\text{km.w.e}$ have been determined using experimental data. The intensity-depth relation can be seen in figure 3.3 which shows the dependence of the muon flux on the vertical depth through the Earth. This plot was made using measurements from underground laboratories at different depths, with a mix of flat and mountain overburdens, including SNOLAB (Sudbury), which has a flat overburden. Figure 3.4 shows how the muon intensity changes with incoming muon direction [38].

The energy spectrum of the muons is given by

$$\frac{dN}{dE} = A e^{-bh(\gamma_\mu - 1)} \left(E + \epsilon_\mu \left(1 - e^{-bh}\right)\right)^{-\gamma_\mu}, \tag{3.8}$$

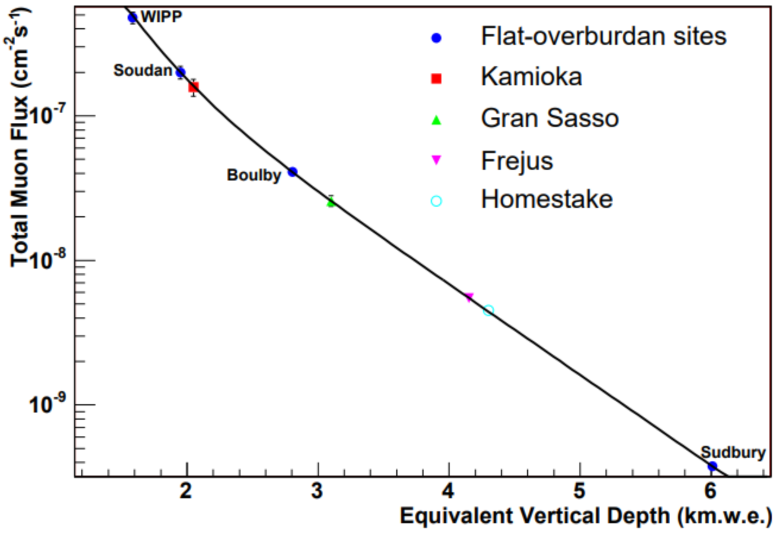

Figure 3.3: The muon flux as a function of equivalent vertical depth, using fluxes measured at different underground sites. The sites labelled as “Flat-overburden sites” have been fitted with equation 3.7, with the parameters floating, given by the black line. The other sites are a mix of flat and mountain overburdens [38].

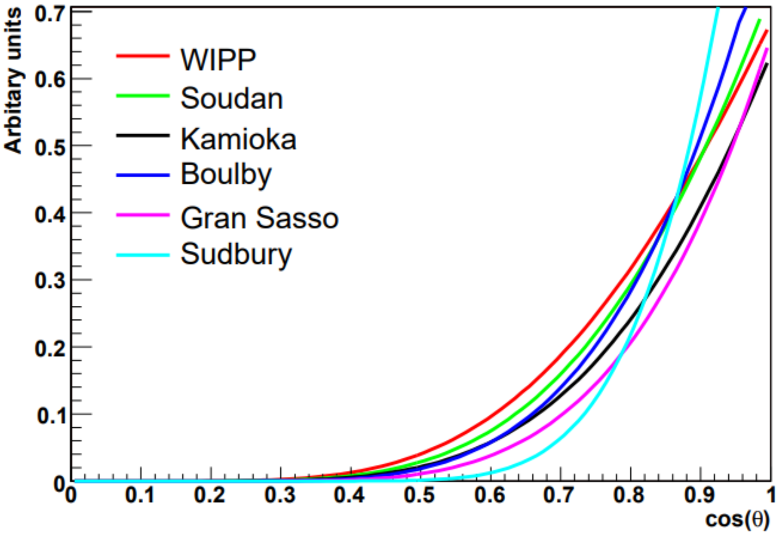

Figure 3.4: The angular distribution of the muons at different underground sites, based on equation 3.7 [38].

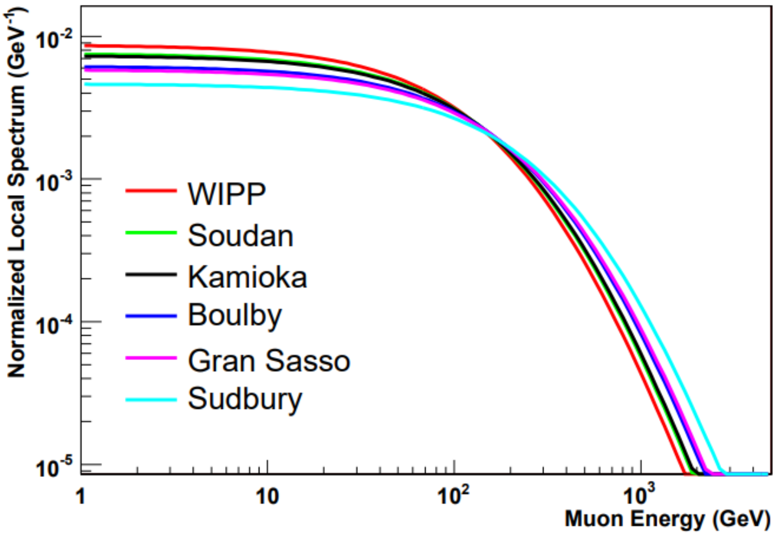

Figure 3.5: The muon energy spectrum at different underground sites, based on equation 3.8 [38].

which is represented in figure 3.5 [38]. A is the normalisation constant, and the constants $b = 0.4\,/\text{km.w.e}$, $\gamma_\mu = 3.77$ and $\epsilon_\mu = 693\,\text{GeV}$ [39].

3.2 Neutron Production

There are a number of ways in which muons can produce neutrons. Considered one of the most common mechanisms for neutron production are the interactions associated with muon-induced showers. As discussed, muons moving through a medium lose energy through ionisation and radiative processes. The daughter particles from these processes induce particle showers, of which there are two kinds: electromagnetic and hadronic. A particle shower is the result of an initial particle producing multiple secondary particles which then go on to produce further particles, creating a shower of particles. Each particle is produced with less energy than its parent particle, causing the average particle energy to fall over time. Once the average energy of the particles in a shower falls below the critical energy of the medium, the production rate of particles starts to decrease due to ionisation becoming the dominant form of energy loss [40].

In electromagnetic showers, electrons, positrons and gammas are produced via pair production and bremsstrahlung. The gammas may also undergo photonuclear processes to produce neutrons, and charged pions. In hadronic showers, charged and neutral pions are produced. The charged pions will mostly go through a series of inelastic collisions causing nuclear breakup and the production of neutrons and more pions. Meanwhile, the neutral pions will decay into pairs of gammas which can incite an electromagnetic shower. The critical energy of hadronic showers in water ($\sim 1\,\mathrm{GeV}$) is greater than the critical energy of electromagnetic showers in water ($80\,\mathrm{MeV}$). This means that hadronic showers are rarer than electromagnetic ones [41]. When the average energy of a hadronic shower falls below $\sim 300\,\mathrm{GeV}$, pion production is suppressed and another type of hadronic shower takes over. In these showers, called nucleon cascades or neutronic showers, protons and neutrons can be released from nuclei by a gamma.

Another way free neutrons are produced is by the muon directly, through a process called muon spallation. This is the release of nucleons, from a nucleus, after colliding with a muon. Spallation can also occur after collisions between nuclei and other muon-induced particles such as protons, pions and even the neutrons themselves [40].

The neutrons, produced through the above mechanisms, can go through a series of collisions and scatters before finally undergoing radiative capture. In water, neutrons capture onto the hydrogen atoms to produce a $2.2\,\mathrm{MeV}$ gamma γ, as shown in

$$n +^1_1 H \rightarrow^2_1 H + \gamma\,(2.2\,\mathrm{MeV}). \tag{3.9}$$

The average time for a neutron to capture in water is $\sim 200\,\mu\mathrm{s}$ [42].

3.3 Cosmic Muon-Induced Neutrons in Simulation

3.3.1 Simulating Muons and Neutrons in SNO+

The random nature of particles makes it difficult to predict how they will interact. Monte Carlo (MC) simulation is a computational technique that uses repeated random sampling to model complex systems. This method is employed by SNO+ for the purpose of simulating particles and their interactions within the SNO+ detector. The overall framework uses GEANT4 [43], a software package that accurately simulates the passage of particles through matter, to do the low level physics simulation and particle tracking. The other aspects of the simulations, including detector geometry, and the readout and trigger systems (see section 4.1.1), are also incorporated into this framework.

Simulations of muons should model the muon flux at the SNO+ detector as well as the interactions they induce during their passage through the detector. The distance a muon travels through the Earth, before reaching the detector, depends on their direction. The further a muon must travel, the more likely it is to be attenuated before reaching the detector. This angular dependence must be included in the simulation of muons.

In order to replicate the intensity of the muons in different directions at SNO+, equation 3.7, in section 3.1, is sampled using a vertical depth $h_0 = 6.011\,\text{km.w.e.}$ The energies of the muons, as a function of direction, are sampled from equation 3.8. This flux distribution models the angular dependence due to the flat rock overburden. The angular dependence of the muon flux at the surface of the Earth is assumed to be negligible. Figure 3.6 shows the distribution of muon energies and directions at SNO+. The sampling of this spectrum serves as the starting point for the muon simulations, as implemented by the author. This muon flux model predicts an average cosmic muon energy of $(364 \pm 1)\,\text{GeV}$ at SNO+, where the uncertainty here is the uncertainty in calculating the average energy.

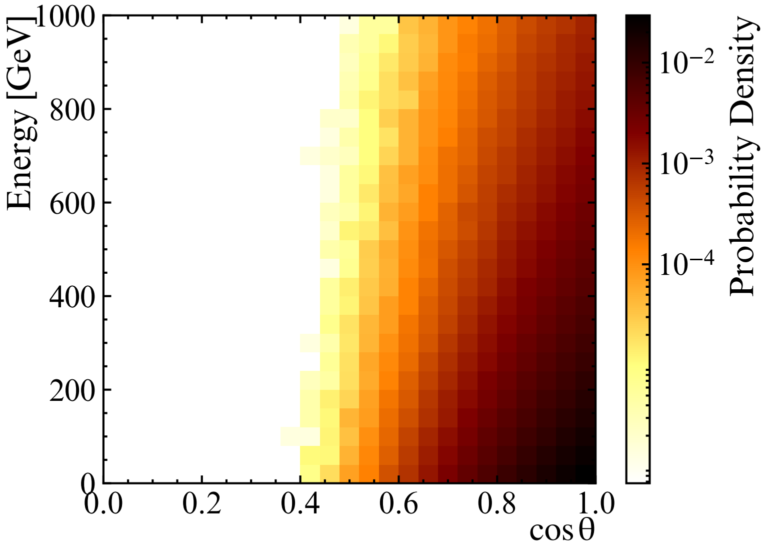

Figure 3.6: The cosmic muon energy spectrum at SNO+ as a function of direction (θ) used for modelling the muon flux in simulation.

3.3.2 Simulating Neutron Production

Simulating muon-induced neutron production accurately is important for background estimation in underground experiments. In the SNO+ simulation framework, neutron production is simulated by Geant4 (version 10.00.p04). A custom physics list is used in which High Precision is used for neutron physics between 0-20 MeV. In the 10 MeV-GeV range, the Bertini and Binary Cascade models for hadrons are used, and the Quark-Gluon String Model is used at very high energies. Figure 3.7 presents the energy spectrum for muon-induced neutrons in SNO+ simulation.

FLUKA is another MC simulation tool that can model the transport of particles from energies of keV and above [44], including the passage of cosmic rays through any material. This makes FLUKA an alternative neutron production simulator to Geant4. Figure 3.8 compares the contributions to cosmogenic neutron production that are predicted by the two MC packages. At very low muon energies, both FLUKA and Geant4 agree on the ordering of the mechanisms which contribute to neutron production, with photonuclear processes from electromagnetic showers contributing the largest fraction. In both cases, the fraction of neutrons produced from photonuclear processes and muon spallation decreases as muon en-

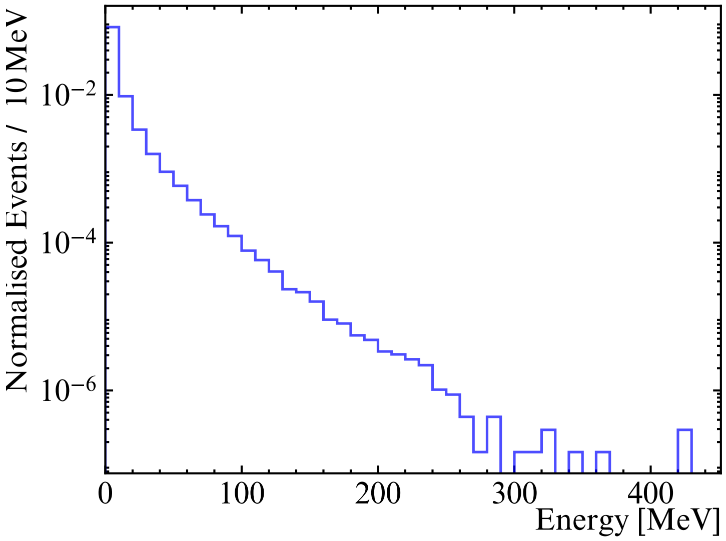

Figure 3.7: The starting energies of muon-induced neutrons in SNO+ simulation.

ergy increases, with production via hadronic showers increasing at the same time. However, Geant4 predicts that production through electromagnetic showers will remain dominant as muon energy increases, whilst FLUKA predicts production from hadronic showers will take over as most dominant [45].

These differences in the neutron production, between the two simulation packages was studied in [45]. In this paper, they reported that Geant4 predicts up to 30% less neutrons than FLUKA, for muons with energies greater than ∼ 100 GeV [45].

3.4 Cosmogenic Neutron Yield

The cosmic muon-induced neutron yield is a density-normalised measurement of the number of neutrons produced by a muon per unit track length. This analysis calculates the yield in water. For a given muon, the neutron yield Y_n^μ is calculated using

$$Y_n^\mu = \frac{N_n^\mu}{L^\mu \rho}, \tag{3.10}$$

where N_n^μ is the number of neutron captures produced by the muon, along its track in water; L^μ is the track length of the muon; and ρ is the density of the medium. The number of neutron captures produced by a muon is related to the number of

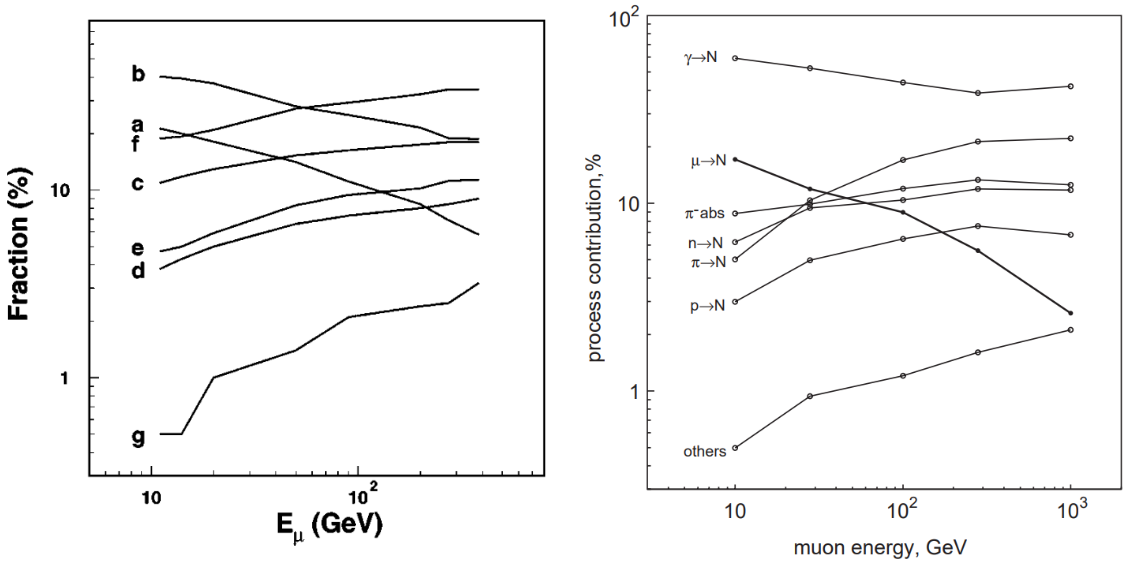

(a) FLUKA [40].

(b) Geant4 [45].

Figure 3.8: The contributions to cosmic muon-induced neutron production, as a function of muon energy, as predicted by FLUKA (left) and Geant4 (right). To aid with comparison, a and $\mu \rightarrow N$ are muon spallation, b and $\gamma \rightarrow N$ are photonuclear processes, c and $n \rightarrow N$ are neutron spallation, d and $p \rightarrow N$ are proton spallation, e and $\pi \rightarrow N$ are positive charged pion spallation, f and π^-abs are negative charged pion spallation and absorption, and g and others includes photonuclear interactions, kaon spallation, and reactions involving light atomic fragments, anti-nucleons and short-lived hadrons.

neutron captures observed N^{μ}_{obs} through

$$N^{\mu}_{\text{obs}} = \varepsilon^{\mu} N^{\mu}_{n} + B^{\mu}_{C} + B^{\mu}_{R}. \tag{3.11}$$

In equation 3.11, ε^{μ} is the neutron selection efficiency; B^{μ}_{C} is the muon correlated backgrounds; and B^{μ}_{R} is the random detector backgrounds that coincide with a muon. The neutron selection efficiency is the probability of detecting a neutron and is discussed in section 7, and the two types of backgrounds are discussed in section 6.

The number of neutrons a muon produces will increase with muon energy due to an increase in the electromagnetic and hadronic shower energies, creating more secondary particles. This has been demonstrated experimentally, as shown in figure 3.9. This plot shows measurements of the neutron yield made at different underground laboratories. The variation in depths of the laboratories gives a variation in the average muon energy. The larger the overburden, the higher the average muon energy. This is due to the low-energy muons being attenuated by the Earth's crust. SNOLAB has one of the largest overburdens of an underground laboratory, meaning that the average energy of muons travelling through is relatively high. Thus, measuring the neutron yield at SNO+ will provide a greater insight into neutrons produced from muons with a higher energy.

The results shown in figure 3.9 are mostly from liquid scintillator-based measurements. However, there are two results from water-based measurements; one was made by the SK experiment [50] and the other by the SNO experiment [55]. The SNO measurement was made using both pure heavy water and NaCl-loaded heavy water. The SK measurement was made using gadolinium-loaded water. The measurement from this analysis, using the data taken during the water phase of SNO+, is the first measurement made using undoped ultra-pure water.

As shown in figure 3.10, the neutron production of the various contributions to the neutron yield increases with atomic weight. This can only be tested through measuring the neutron yield using the same muon energy with different materials. Since the SNO+ experiment uses the same detector as the SNO experiment, the

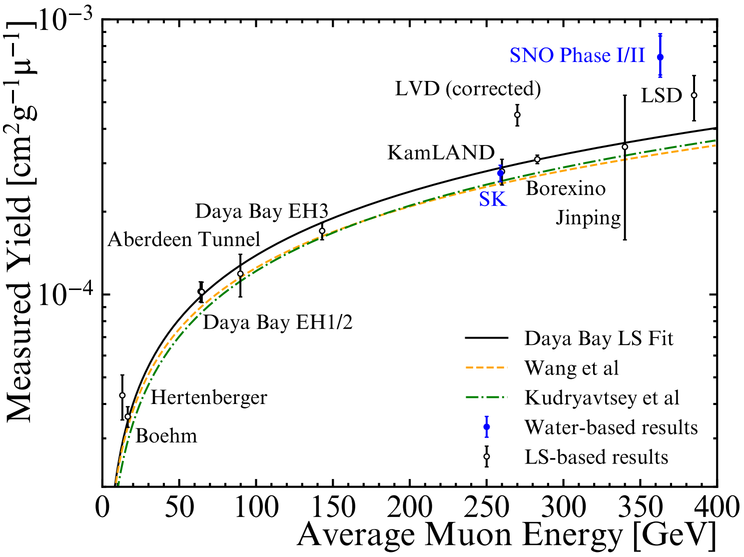

Figure 3.9: How the neutron yield changes with energy, as measured by different underground experiments: Hertenberger [46], Boehm [47], Daya Bay [48], Aberdeen Tunnel [49], SK [50], KamLAND [51], LVD [52], Borexino [53], Jingping [54], SNO [55], LSD [56], in order of average muon energy. The solid line is a fit made for liquid scintillator based measurements by Daya Bay [48]. The dashed lines are FLUKA-based liquid scintillator predictions [40][57].

average muon energy is the same. This allows for the comparison of neutron yields in different media from the same muon flux. A similar comparison was made after the SK measurement. The SK detector is at a depth approximately equal to the depth of the KamLAND experiment, within the same mountain. While the SK detector was filled with gadolinium-loaded water, the KamLAND detector was filled with liquid scintillator [51]. It was reported by the SK experiment that their result was consistent with the KamLAND result [50].

This section has provided the motivation behind using SNO+ to measure the cosmogenic neutron yield. Before carrying out the analysis, a great deal of work has gone into producing the events that will be looked at. This work will be summarised in the next chapter.

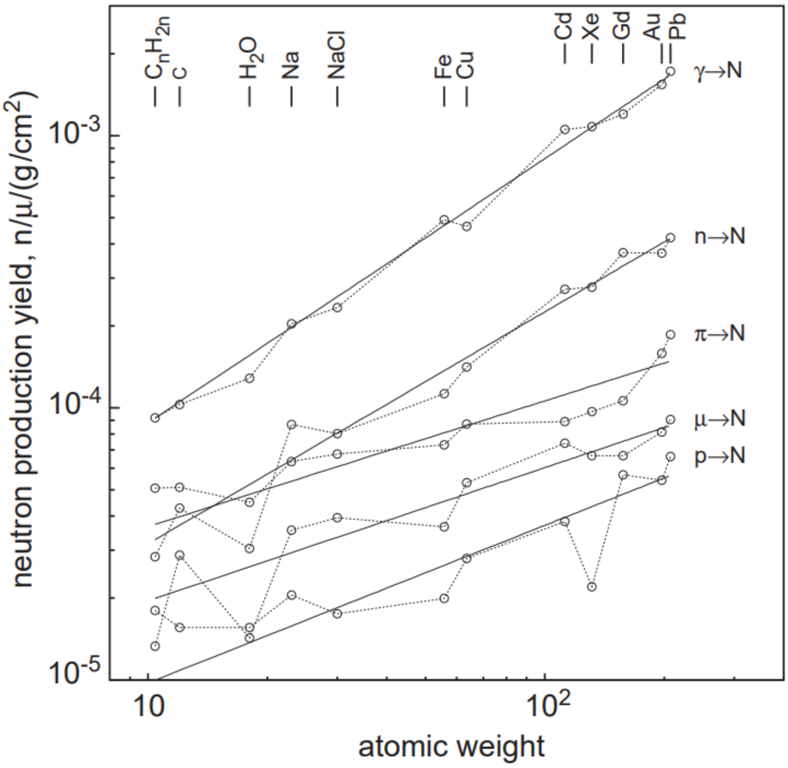

Figure 3.10: The contributions to the cosmic muon-induced neutron production yield as a function of atomic weight, for 280 GeV muons simulated in GEANT4. The process $\gamma \rightarrow N$ is photonuclear processes, $n \rightarrow N$ is neutron spallation, $\pi \rightarrow N$ is charged pion spallation, $\mu \rightarrow N$ is muon spallation, and $p \rightarrow N$ is proton spallation [45].

Chapter 4

Building an Event in SNO+

Before events can be selected and analysed, they first need to be built. SNO+ data, in its rawest state, is simply a collection of positions of hit PMTs, the times at which they were hit, and the amount of charge deposited in them. There are many steps involved in transforming this data into something understandable. This includes recording and storing the data, as described in section 4.1. Next, the detector needs to be calibrated, described in section 4.2, then the events need to be reconstructed, described in section 4.3.

4.1 Recording an Event

This section describes how we go from signal to raw data that can be processed for analysis, a very important stage of any experiment. The first section will outline the general pipeline from a PMT registering a hit, to an event being recorded. This includes the various electronics components that make up this system. The final section will describe the next stage in which the data is organised and stored in files, before being sent for processing.

4.1.1 Event Trigger and Readout Electronics

The trigger and readout systems take the information from the PMTs and decide whether an event has occurred in the detector. The electronics that make up these systems are contained within crates that are located above the detector in an area referred to as the deck. There are 19 crates in total. Within a crate, there are 16 PMT interface cards (PMTICs) that are assigned 32 PMTs apiece. Each PMTIC has an associated front-end card (FEC) which is connected through the crate backplane. A dedicated high voltage (HV) source is connected directly to the backplane of each crate, supplying around 2 kV to each PMT through the PMTICs. The components of the electronics have been significantly upgraded since being inherited from SNO, yet the systems continue to operate following similar procedures as outlined in [58].

After a PMT has detected a photon, as described in section 2.4.2, this information is sent through a 32 m waterproof cable to its dedicated PMTIC in the form of an analogue signal. The PMTIC passes the signal to the associated FEC where it is given to one of four assigned daughter boards (DBs), mounted on the FEC. The DB contains a discriminator, integrator and complementary metal-oxide-semiconductor (CMOS) chip. The discriminator chip compares the signal against an adjustable threshold. If the threshold is exceeded, a "hit" is registered on that PMT and the CMOS chip begins ramping a linear voltage, known as the time-to-amplitude converter (TAC), that is used to measure the time since the hit occurred.

When a hit occurs, the discriminator passes a copy of the signal (ESUM) to the integrator and CMOS chips. The integrator chip integrates the signal to produce three measurements of the charge: high gain long integration (QHL), high gain short integration (QHS), and low gain variable (long or short) integration (QLX). The integrator chip also calculates ESUMH and ESUML which are high and low gain versions of the copied ESUM signal, respectively. The CMOS chip generates two fixed-amplitude pulses with widths of 100 ns and 20 ns named N100 and N20, respectively. N100 is the nominal trigger used for SNO+ data. The N20 pulse can be used to study events in the centre of the detector by varying the delay on the pulses from the different PMTs depending on their positions in the detector. The CMOS chip also contains memory cells which temporarily store this information.

Each crate has a crate trigger card (CTC). Here, the N100, N20, ESUMH and

ESUML from the individual PMTs are summed across the whole crate and sent to the timing rack, which collects the different pulse signals from all 19 crates. The N100, ESUMH and ESUML signals from the OWLs are summed separately to give their own versions of those triggers: OWLN, OWLEHI and OWLELO, respectively. In the timing rack, there are seven analogue master trigger cards (MTC/A+), one for each type of signal: N100, N20, ESUMH, ESUML, and those from the OWLs. Each MTC/A+ applies a low, medium and high gain to their respective pulse signals, resulting in 21 signals that are then sent to the digital master trigger card (MTC/D). If any of the signals pass their preset thresholds, the MTC/D will release a global trigger (GT). Once a GT has been issued, the TAC ramp is stopped, and no more GTs can be used for the next 420 ns. If no GT is issued within 410 ns of a PMT hit, the memory cells in the CMOS chip are cleared, and the TAC and charge are reset.

In the case of a GT being issued, the data that was being stored in the CMOS chip is transferred to the crate's XL3 card. The XL3 card packages the charge and time data, for the PMTs associated to that crate, and sends it to the data acquisition (DAQ) systems. These are described in section 4.1.2.

Trigger Efficiency

As described above, an event is registered if it causes the detector to trigger. The probability that an event will cause the detector to trigger is given by the trigger efficiency. During an event, each time a PMT is hit, a pulse from that PMT is added to the total sum. A trigger is issued when the amplitude of the summed pulses passes the trigger threshold. If all the PMTs issued hits at similar times, then the sum of the pulses will form a tall and narrow peak. If the PMT hits were more spread in time, the sum of the pulses will form a shorter and broader peak. This means that events could have the same number of PMT hits, but only some of the events will actually exceed the threshold and trigger the detector, depending on the spread of the PMT hits in time. This spread of PMT hits in time can be due to event characteristics, such as position and direction. When evaluated as a function of the number of PMT hits, the trigger efficiency will be affected by this dependency.

To avoid dependence on event parameters, the trigger efficiency is calculated using the in-time hits. In-time hits is the number of PMT hits that arrive within a given time window: 89 ns for the N100 trigger and 46 ns for the N20 trigger. The time window is centred at the peak of the summed PMT pulses, and the number of in-time hits is given as the number of overlapping pulses within the time window.

Trigger thresholds are usually governed by the background rates: increasing the trigger threshold leads to less unwanted events triggering the detector. The low background rate in SNO+ means that the trigger threshold can be set relatively low, for a water Cherenkov detector. This allows SNO+ to probe lower regions of energy, including the detection of neutrons in water. During the water phase, the trigger threshold was set to approximately 7 PMT pulses. The relatively low energy of neutron captures means that the signal for detecting neutrons is close to this threshold. Figure 4.1 shows the trigger efficiency as a function of the number of PMT hits. This is compared to the distribution of 2.2 MeV gammas, according to PMT hits. The result of this comparison shows that around half of the 2.2 MeV gamma events will result in a detector trigger.

4.1.2 Data Acquisition and Nearline Processing

The DAQ systems handle the data that has been read out by the electronics, and prepares it for processing. DAQ contains a data server which receives the PMT data from the XL3s of each crate, and trigger information from the MTC/D. The data server passes this information to the event builder, where the data is organised into physics events with an associated trigger [30]. The builder then stores these events in “raw” data files, with the ZEBRA data bank (ZDAB) format. The data is organised into “runs” which are usually up to an hour long. For practicality, the size limit of the data files is set to 1 GB. This forces the data within a run to be split up into “subruns”, with one ZDAB file for each subrun.

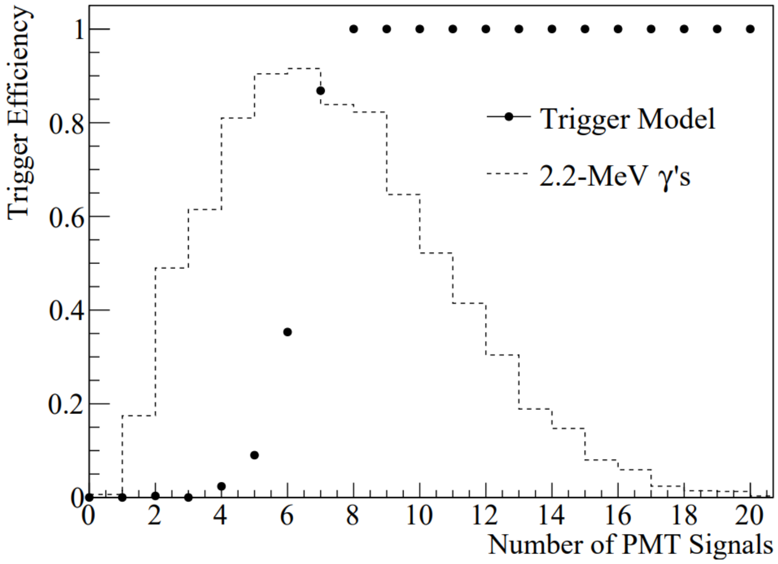

Figure 4.1: How the trigger efficiency changes with number of PMT pulses in simulation (solid points). Also shown is the distribution of the number of PMT signals for 2.2 MeV gamma events (dashed) [42].

For monitoring purposes, it can be useful to receive live feedback from the incoming raw data. The nearline systems have been designed to process incoming runs in real-time. This provides information on the quality of the live data, and can be used for diagnosing issues with the electronics [30].

As well as being sent to the nearline systems, the raw data is also uploaded to various data storage sites. Here, the processing stage can begin, and the events can be reconstructed into physics events. The processing stage is described in more detail in section 5.1.

4.2 Calibration

An important stage in setting up an experiment is understanding the data. This requires a translation between the detector output and measurable quantities such as time and energy, which is achieved through a combination of different calibration techniques. First, the response of the electronics and PMTs to an event must be measured. After this, sources of known energies and/or optical properties are deployed. The resulting correlation is then used to extrapolate properties of real data.

4.2.1 Electronic Calibration

The purpose of electronic calibration (ECA) is to measure the pedestal charge and covert TAC into time, per PMT channel. A pedestal is the offset in the charge, measured by each PMT channel, due to noise. These calibrations are usually performed on a weekly or bi-weekly basis, or after detector maintenance. In the normal detector state, PMTs are “fired” when an incident photon produces a signal that exceeds the threshold for that channel. Software that controls the DAQ can also be used to force a PMT channel to fire. This is known as a pedestal trigger, and is how ECAs are performed. ECA runs that measure the pedestals are separate to those that measure the TAC-to-time conversion.

In a pedestal measuring ECA run, a pedestal trigger is issued to the selected channels. This initiates the charge integrators in those channels then, once the GT has been issued, the charge integration stops. Provided there were no real events coincident with the ECA, the integrators are forced to integrate over a charge-less event. This gives a measurement of the pedestal for that channel.

The conversion between TAC and time is done using time slopes, which are measured for each channel. To measure the time slope of a channel, the time between the pedestal trigger and the GT is varied. When a pedestal trigger is issued in a channel, the TAC starts to ramp until the GT is issued. Varying the time between the pedestal trigger and the GT causes the length of the TAC ramp to vary. Measuring the time that the TAC was ramping for can be used to convert the TAC of real events into real time. This is important for knowing when in an event a PMT was fired [59].

4.2.2 PMT Calibration

The timing calibration of each PMT channel, performed in the ECA, measures the time between PMT trigger and GT. This fails to account for any delays in the timing due to the cable length and the time it takes for a PMT channel to issue a trigger. The PMT calibration (PCA) is done to measure these delays. In the water phase, PCAs were performed by the laserball, a spherical light source, 11 cm in diameter, that can be deployed at different positions within the detector using the SMS. Light travels into the laserball via optical fibres that are fed through the umbilical. The light passes into a sphere which contains air-filled glass beads with a diameter of 50 μm. The beads, held in place by a silicone gel, diffuse the light isotropically around the detector [60].

The lengths of the cables which connect the PMTs to their associated crates, where the discriminator chips are located, mean that there is a delay between the PMT receiving a hit and a trigger being issued. This delay is known as a cable delay. There is also a delay due to the time it takes for a PMT pulse to cross the discriminator threshold. This is called a time walk. Time walks depend on the size of the pulse, as shown in figure 4.2. In this figure, the larger of the two pulses crosses the threshold before the other, causing a difference in the time at which their triggers are issued. Using the laserball, photons are fired at PMTs at a known time. The intensity of the laser can be adjusted so that PMTs receive only single photons. The time between the photon reaching the PMT and the subsequent trigger is used to calculate the cable delays and time walks for each PMT.

The measurements taken in the ECA result in an integrated charge that has been corrected for the pedestal. However, this still needs to be related back to what has been observed by the detector. The integrated charge can be calibrated in a PCA by measuring the charge generated in a PMT from the laserball light. This can be used to convert the charge deposited by a PMT into single photo-electron units [61].

4.2.3 Optical Calibration

Optical calibrations are necessary for observing how light travels within the detector. The geometry and components of the detector causes light to undergo many different optical processes. For example, light will be refracted at the water-AV boundary,

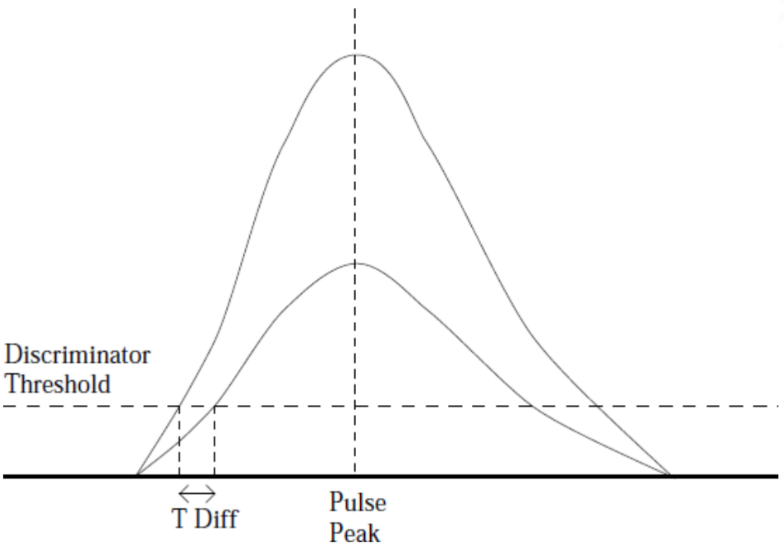

Figure 4.2: Two simultaneous PMT pulses with different charges that cross the discriminator threshold at different times, with T Diff being the difference in those times [61].

with the amount of refraction depending on the wavelength of the light and the position where the light originated. The laserball, introduced above, was used for the optical calibration during the water phase. The laserball contains dye cells which the light is passed through to select different wavelengths. Laserball calibration was performed at different positions in the detector, using different wavelengths of light [60].

4.2.4 Energy Calibration

The more energy a particle has, the more photons it will produce. This will lead to a greater number of PMT hits. For this reason, PMT hits are used as a measure of energy. To be able to do this, an energy calibration must be performed in order to determine the conversion factor between PMT hits and energy. This involves using a source of known energy and measuring the detector response. There is some variation in response over the detector volume, so the source is deployed at multiple positions in the detector. In the water phase of SNO+, ^{16}N was used as the energy calibration source [60].

^{16}N gas is sent through the gas capillary that runs through the umbilical, into a container that is attached to the end. The container houses a scintillator block and a PMT, with the power and signal cables running through the umbilical. The ^{16}N β decays, with a half-life of 7.1 s, into ^{16}O which is left in an excited state. The β-particles interact with the scintillator block and are detected by the source container's PMT. The ^{16}O will de-excite via the emission of a 6.1 MeV gamma for 66.2% of decays, and a 7.12 MeV gamma for 5% of decays. The gamma will penetrate the container and undergo Compton scatters to produce electrons which are detected by the detector, and the resulting spectrum is used to calibrate energy. The timing coincidence between the β-particle and the gamma is used to tag the events from the ^{16}N decays. Using the SMS described in section 2.4, the source can be moved to different positions within the AV, and between the AV and the PSUP [62].

4.2.5 Am-Be Calibration

The Am-Be calibration uses a mixture of powdered ^{241}Am and ^{9}Be, contained within a sealed capsule that can be attached to the umbilical, and positioned at different parts of the detector using the SMS. The different Am-Be positions are shown in figure 4.3. The positions that are contained within the AV are referred to as internal, and the positions in the space between the AV and the PSUP are referred to as external.

^{241}Am is known to α decay with a half-life of 432 years. The α particles will be adsorbed by the ^{9}Be nuclei to form ^{12}C and a neutron. Around 60% of the ^{12}C will be in an excited state. De-excitation occurs through the emission of a 4.4 MeV gamma. The neutron will travel a short distance before being captured on hydrogen, causing the emission of a 2.2 MeV gamma. The coincidence of a prompt 4.4 MeV gamma followed later by a delayed 2.2 MeV gamma can be used to identify these events.

As already discussed, neutrons are difficult to detect in pure water due to their low energy signal. However, SNO+ is able to set its trigger threshold low enough

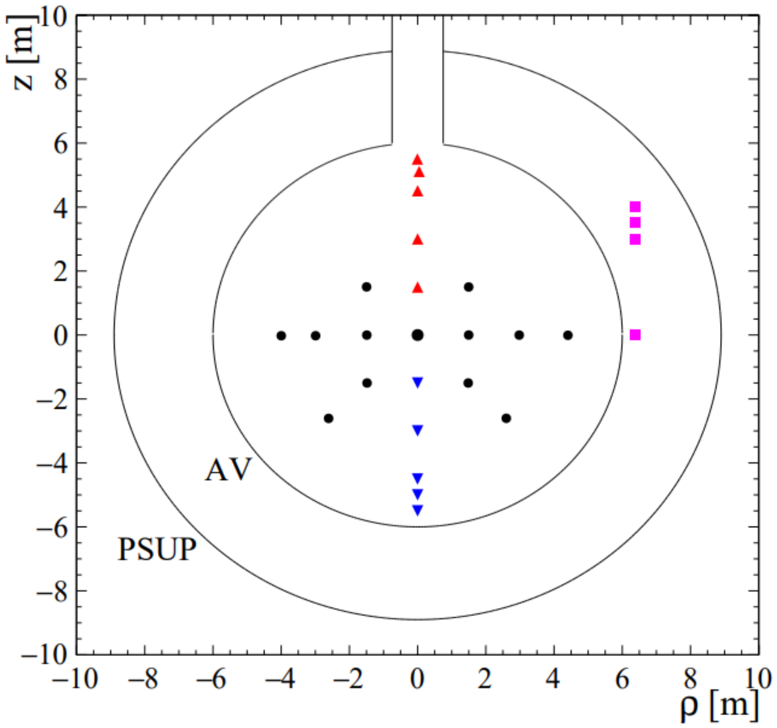

Figure 4.3: The different positions of the Am-Be source. For all positions along the vertical axis, positions at $z > 0$ are red and positions at $z < 0$ are blue. All other positions in the AV are black, and all positions outside the AV are magenta [42].

to detect the 2.2 MeV gamma produced in neutron capture. The Am-Be source was used to demonstrate SNO+'s ability for observing neutrons, and measure the neutron detection efficiency in different areas of the detector. The analysis found that the neutron detection efficiency in water, within the inner region of the detector, is $(50 \pm 1)\%$. Figure 4.4 shows the neutron detection efficiency for different radii [42].

Another measurement made during the Am-Be calibration was of the neutron capture time. This is the average lifetime of a neutron before capturing on hydrogen. The neutron capture time was measured to be $t_n = 202.53^{+0.87}_{-0.76}\,\mu\text{s}$ [42].

4.3 Reconstruction in Water

The data produced by the detector tells us which PMTs were hit in a given event, along with the time they were hit and the charge deposited in each PMT. Reconstruction is the process of taking this information and finding the most probable

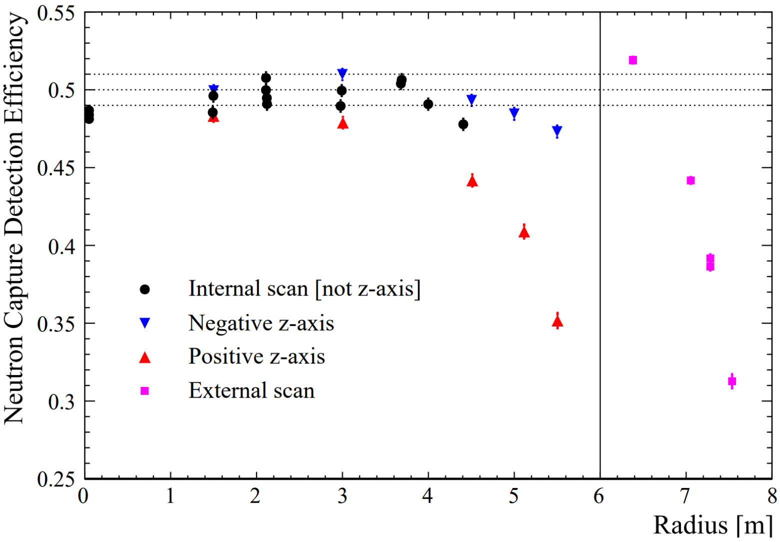

Figure 4.4: The neutron detection efficiency in water as a function of radius, measured using the deployed Am-Be calibration source at the positions given in figure 4.3 [42].

time, position, and energy of the event. SNO+ uses specially designed fitters to do this job. Events in SNO+ are typically point-like, and can be reconstructed using a single fitter, as described in section 4.3.1. However, the nature of cosmic muon events means that they require their own fitter for reconstruction which is outlined in section 4.3.2.

4.3.1 Reconstructing Point-Like Events

In this section, the methods for reconstructing point-like events are presented. Although some of these events may produce particle tracks, the tracks are small with respect the to our position resolution. For this reason, they can be assumed to be point-like.

The reconstruction method is broken up into four separate sections: Position, Direction, Drive Correction, and Energy. As the names suggest, the Position, Direction and Energy sections describe the reconstruction of the event's position, direction and energy, respectively. The Drive Correction section describes how the event's reconstructed position and direction are used to calculate a correction to the position, which is biased due to the characteristics of Cherenkov radiation. This is all performed by the SNO+ water fitter.

Position

The times at which each PMT is hit are key to reconstructing an event's position. The spherical geometry of the detector means that photons from the centre of the detector will arrive at the PMTs at the same time. Anything off-centre will have a distribution of PMT hit times; the PMTs closest to the event will trigger before those that are furthest away. SNO+'s water fitter draws on this to reconstruct single-site events.

In the first step of reconstructing the event, an approximate position and time are found. This is done by taking a group of four PMTs, and using their hit times t_h and positions $\vec{x}_h$ to solve

$$|\vec{x}_h - \vec{x}_e| = c(t_h - t_e) \tag{4.1}$$

to give the event's time t_e and position $\vec{x}_e$. In this case, the photons are assumed to have travelled in a straight line, with no scattering. This process is repeated for multiple random combinations of four PMTs, and the median event time and position are found. The output of this method is used as an input for the next step, where a more accurate position and time are found. The purpose of this step is to speed up the reconstruction, as this method is quicker than the method used next [1].

Using the approximate event time and position provided by the step above, a more accurate time and position is found, which takes into account the scattering effects that the photons might incur during their path towards the PMTs. A PMT's time residual t_{res}, given in

$$t_{res}(\vec{x}_e, t_e) = t_h - t_{tof}(\vec{x}_e) - t_e, \tag{4.2}$$

is the difference in time between the measured and expected hit time. This uses the time of flight t_{tof}, the time taken by a photon to travel from the position of the event to the PMT. This is calculated using

$$t_{tof} = \sum_i \frac{d_i}{v_i}, \tag{4.3}$$

where d_i is the distance travelled in volume i and v_i is the speed of photons in volume i, for the water and AV volumes. The distances photons will travel through each volume is determined by their position in the detector. The speed of light in each volume is calculated for a wavelength of 400 nm, the peak wavelength of Cherenkov light in water [63].

For each event, a distribution of PMT hit time residuals is generated using equation 4.2. This distribution is expected to follow a particular shape. Prompt photons, which quickly arrive at their PMTs, with minimal scattering, will have time residuals close to zero. This results in a Gaussian peak, centred near and around zero. Delayed light comes from photons that have had many scatters along their journey to the PMT. These hits will have slightly longer time residuals, causing a tail in the distribution. A model PDF of the time residuals has been generated from simulation and calibration. For a postulated event position and time, the distribution of time residuals can be compared to the expected shape, from the model PDF, as shown in figure 4.5. The comparison results in a likelihood that the event has a position and time equal to the postulated position and time, which is floated. The event time and position which gives the maximum likelihood is used as the reconstructed time and position of the event.

This position fitter will be the method used for reconstructing the 2.2 MeV gammas that are used to identify neutron captures. It is important that the position reconstruction performs well on these events. Figure 4.6 shows the difference between the reconstructed and true position when the position reconstruction method is applied to 2.2 MeV gammas, simulated in the detector.

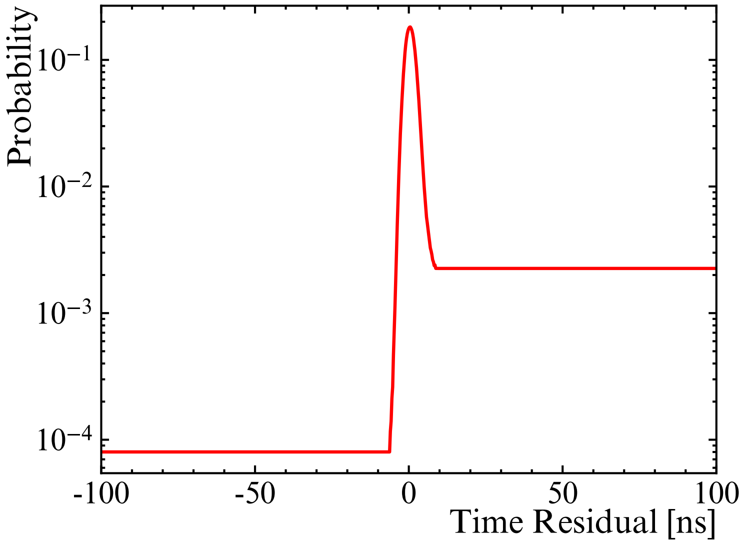

Figure 4.5: Time residual distribution generated from simulating 6 MeV electrons in the detector.

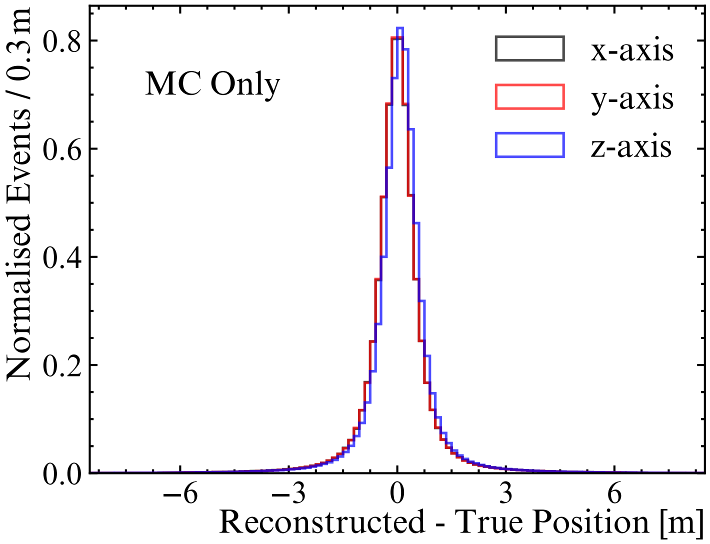

Figure 4.6: The difference between the reconstructed and true positions of simulated 2.2 MeV gammas, in the x (black), y (red) and z (blue) directions.

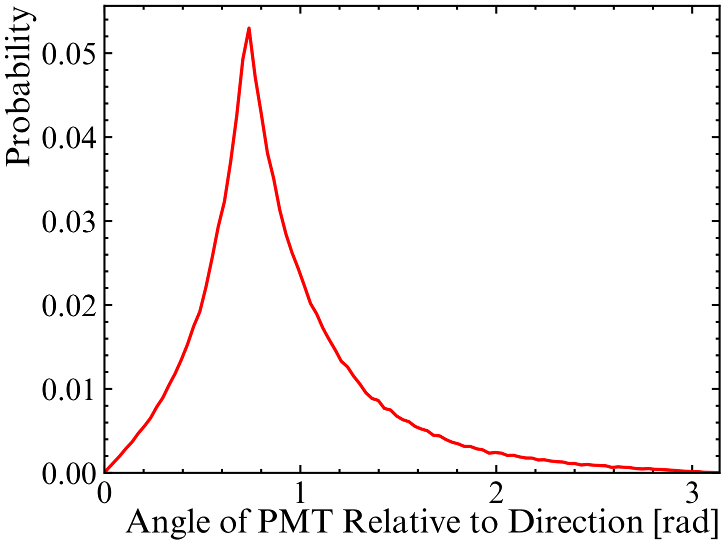

Figure 4.7: Distribution of angles between the direction of an event and the position of a hit PMT relative to the event's reconstructed position. This was generated using one million simulated 6 MeV electrons at the centre of the detector.

Direction

Like with the position fitter, the direction reconstruction method begins with an approximate value, which is used as an input into a likelihood-based method. The approximate direction is found using the charge-weighted centre of the PMT hits involved in the event. The vector between the event's fitted position and the charge-weighted centre of the PMTs gives an estimate of the direction.

The direction will be floated around the estimated direction to find the most probable direction. Whether a direction is more probable or not is based on its distribution of angles between the event's direction vector and the straight line that connects the hit PMT to the event's reconstructed position [63]. The shape of the distribution is compared to a model PDF, shown in figure 4.7, and the likelihood of that direction is calculated. For the range of postulated directions, the direction which maximised the likelihood is selected as the reconstructed direction [1].

Drive Correction

The behaviour of the Cherenkov cone can cause a bias in the reconstructed position of the event, along the direction of the cone. This bias comes mostly from the scattering of photons from the Cherenkov cone. The scattering causes an observed change in the Cherenkov angle, which results in a shift to the apparent source of the cone (i.e. the event position). The corrected position $\vec{r}_{cor}$ is found using the reconstructed position $\vec{r}_{recon}$ and direction $\vec{u}_{recon}$ in the following equation

$$\vec{r}_{cor} = \alpha\vec{r}_{recon} + \beta\vec{u}_{recon}, \tag{4.4}$$

where α and β have been tuned using simulation [1].

Energy

The method for reconstructing an event's energy is based on the simple fact that the more energy an event has, the more light it will produce. In the first step, the energy fitter will take the number of prompt PMT hits of the event, along with the event's position and direction, and convert to energy to give an approximation. This is used as an input for the next method, which takes into account the optical response of the PMTs, evaluated from calibrations. Based on the number of prompt hits, position and direction, this method will estimate the number of Cherenkov photons produced by the event. The number of Cherenkov photons can then be converted into energy, using conversion factors that have been derived from energy calibration. In water, the conversion between PMT hits and energy was approximately 8 PMTs per MeV [1]. Figure 4.8 shows the agreement in energy between the reconstructed data from the ^{16}N calibration and simulation. There is a divergence in the energy at around 2.5 MeV due to trigger threshold effects [62].

The number of PMT hits is a discrete quantity, leading to a Poisson distribution. The uncertainty in a Poisson distributed quantity is given by the square-root of the quantity. For example, for an event with N_{hits} PMT hits, the uncertainty in the

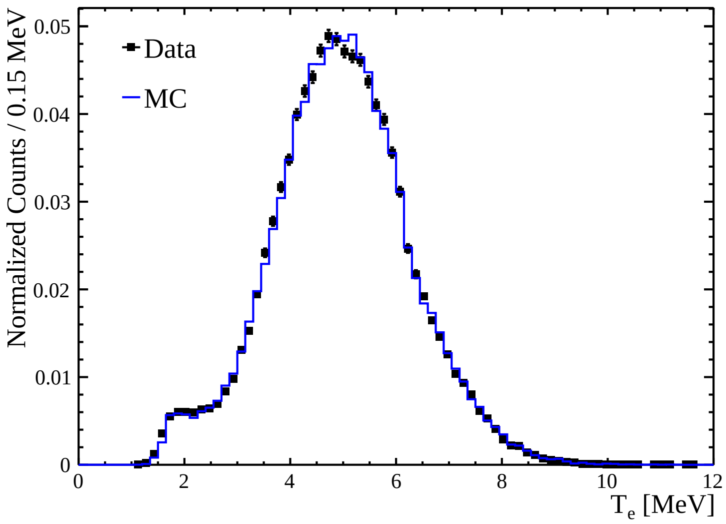

Figure 4.8: The reconstructed energy of the ^{16}N data (black) compared with the model in MC (blue), for the source being positioned at the centre of the detector [64].

number of PMT hits for the event is $\sqrt{N_{hits}}$. This translates directly through the conversion from PMT hits to energy, so that the fractional uncertainty in the energy follows $1/\sqrt{N_{hits}}$. As an unavoidable factor, this is known as the Poisson limit, and is something that cannot be improved by reconstruction methods [1].

4.3.2 Reconstructing Muons

Cosmic muons will enter the detector from above. Most will have enough energy to make it through the detector and exit. These are called through-going muons. If the muon does not have enough energy it will come to a rest within the detector and decay, producing a high energy electron. These are called stopping muons. The muon fitter requires both an entry and exit point for each muon. Since stopping muons do not have an exit point, the fitter will reject these events.

As a cosmic muon travels through the detector, it produces Cherenkov light at every point along its track. The PMTs that are hit early in the event window will indicate the muon's point of entry. The momentum of a cosmic muon is large enough that any interaction it undergoes along its track will have a negligible effect on the muon's direction. This means the muon's path can be assumed to be a straight line.

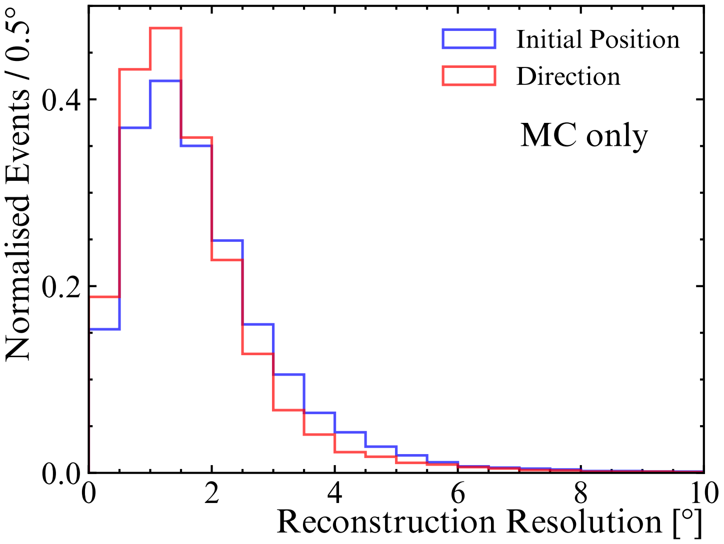

Figure 4.9: The angle between the true and reconstructed initial position (blue), and the true and reconstructed direction (red) vectors when the muon fitter is used to reconstruct muons in simulation.

The speed of the muon during its time in the detector will be close to constant, meaning the angle that the Cherenkov radiation is emitted in will be constant, due to equation 2.7. As a consequence, the PMTs that the muon is directed towards will receive a higher amount of the Cherenkov light than the others. This can be observed as the PMTs about the muon's exit point show a greater charge deposition.

The muon fitter, as described in [1], works by finding the muon's entry point and exit point, and drawing a vector between the two to represent the muon's direction. The entry point is found using the early hit PMTs. Firstly, the first 80 PMT hits recorded for the event are selected. Of these PMTs, the average position is calculated. If any of the 80 early hit PMTs are positioned more than 26° from the average position, these PMTs are assumed to be noise hits and are removed. After this, the average position of the 20 earliest remaining PMTs is found. This is projected onto the inner PSUP which is taken as the muon's entry position. The exit point of the muon is then given by the charge-weighted average of all hit PMTs. Figure 4.9 shows how well the muon fitter performs on muon simulations.

4.4 Chapter Summary

As this chapter has described, there is a great deal of work that must be done before analyses can be started. In section 4.1, the SNO+ electronics and DAQ systems were described. As shown, working with neutrons means working at and around the detector threshold. This makes it very important to understand how the detector trigger system works.

In section 4.2, various calibration methods were described. Calibration helps with understanding the detector. In particular, the Am-Be calibration used a neutron source to measure the neutron detection efficiency at different positions in the detector. This calibration provided the realisation that SNO+ has the ability to detect neutrons in UPW, an important feature for this analysis. The analysis of the Am-Be data gave a neutron capture life-time of $t_n = 202.53^{+0.87}_{-0.76}\,\mu$s.

Finally, section 4.3 outlined the reconstruction methods that will be used to reconstruct both neutron captures and muons. Like most events in SNO+, neutron captures are point-like events, and so use the general reconstruction methods used for most data. Muons, on the other hand, are track-like events, and require their own reconstruction method. Both were described in this section.

After applying the tools introduced in this chapter, the cosmic muons and the neutrons they produce can now my identified. The next chapter will explain how the candidate events are found.

Chapter 5

Event Selection

The water phase of SNO+ ran from September 2017 to July 2019. As a consequence of adding the AV cover gas system part way through the water phase, the data is split into two separate groups. The data taken up to October 2018 is referred to as the high background dataset. All subsequent data is placed in the low background dataset. As stated previously, the SNO+ data is organised into ∼hour long runs. An initial selection is applied to the runs to discard any runs that are considered to be of a poor quality. After this, the data is processed. This stage takes us from the information given by the PMTs for a triggered event to reconstructed particles. The run selection and processing steps are described in section 5.1.

This analysis requires a pure sample of muons which is achieved through the set of criteria, outlined in section 5.2. The criteria for selecting the neutron followers are presented in section 5.3, and section 5.4 gives the results from the selection. The selection criteria described in these sections were designed and optimised by Billy Liggins in [1].

5.1 Run Selection and Processing

Run selection is the process of discarding runs which should not be used for physics analysis. Discarded runs could include those in which there were multiple electronics breakdowns, and runs that were less than 30 minutes. Runs were also required to have all crates running in order to reduce reconstruction uncertainty due to lack of detector coverage. This check also enforces another requirement that the OWLs must be on in order to tag cosmic muons. The selected runs then go on to the processing stage. Work performed by the author on designing new run selection criteria during the scintillator phase is described in appendix A.

During processing, events that are considered undesirable for a typical physics analysis are flagged by data cleaning (DC). These events include any instrumental effects and muons. Compared to most other particles, muons produce a relatively large amount of light in the detector which causes many PMTs to register hits. An event is initially tagged by DC as a muon if there are 150 or more inward-facing PMT hits and at least 5 OWL hits. As this tag was designed to remove muons from a typical physics analysis, it has close to 100% efficiency with a sacrifice to the purity of the tagged muons. Events are tagged as a muon follower if they occur within 60 s after a muon tagged event. A typical physics analysis would likely aim to remove muons and their followers, but as this is a muon follower analysis, a custom data processing was developed. In this custom processing, if an event is tagged as a muon then the muon reconstruction fitter is applied, as outlined in section 4.3.2. If the event is tagged as a muon follower and has more than 9 PMT hits, the event is reconstructed.

Events not tagged as a muon or muon follower can be used to calculate the rate of random backgrounds. These are low energy backgrounds, with an assumed uniform rate, that occur in coincidence with a muon and count toward the muon follower signal. In order to calculate the rate of these events on a run-by-run basis, a 10% sample of events with between 9 and 25 PMT hits, per run, are reconstructed. These events will be discussed further in section 6.2.

5.2 Muon Selection

The initial conditions applied for selecting muon candidates, in the processing stage, prioritise efficiency over purity. In order to get a pure sample of muons for this analysis, additional selection criteria are applied. The development of the muon selection criteria was performed by Billy Liggins and is outlined in [1].

The number of PMT hits per event is denoted as nhits. Of the PMTs that make up the SNO+ detector, not all can be relied upon for accurate data all of the time. Unreliable PMTs are flagged by channel software status (CSS), which runs a series of checks on a run-by-run basis. These checks look for PMTs that have a higher or lower activity than expected. The number of PMT hits per event, after removing hits from CSS-flagged PMTs, is called cleaned nhits. Of the candidate muons selected in processing, those with cleaned nhits less than 1238 are removed.

Cherenkov radiation means that a muon produces a large amount of light, concentrated along its direction. This leads to a high amount of charge (QHS) being deposited in the PMTs closest to the muon's exit point. As the PMTs outside of the muon's flight path won't receive as much charge, muon events are expected to have a wide distribution of QHS values. Events where the root-mean squared (RMS) of the QHS distribution is less than 4.5 GSU are removed from the dataset, where gain scaled units (GSU) are the calibrated QHS registered on each tube over the high half point on that channel. These events with narrow QHS distributions are unlikely to be muons.

Another characteristic of a Cherenkov light producing event is that their distribution of PMT hit times is peaked where a large amount of PMTs are hit at the same time. This means that if events have their PMT hit distributed uniformly in time, they are probably not muons. If the RMS of the PMT hit time distribution for the event is greater than 38 ns then the event is removed.

Once these initial conditions have been applied to the muon tagged events, the following DC cuts are applied: neck event, burst, atmospheric and retrigger cuts. The neck cut removes any events with a large number of hits in the neck PMTs. The burst cut will remove events that are breakdowns; events wrongly tagged as a muon. Muons which decay within the detector, such as atmospheric and stopping muons, are removed by the atmospheric cut. This looks for events with a high number of

PMT hits (≥ 200) followed by an event with a slightly lower number of PMT hits (≥ 100), within $20\,\mu$s of the first event. This is the signature of a muon produced by a neutrino which then decays to a Michel electron. The retrigger cut removes events which occur within $3\,\mu$s of each other in order to remove small bursts of electronic breakdowns known as a wet end breakdown (WEB).

The final pair of conditions are applied to the reconstructed track length and direction. Due to the uncertainty in the reconstruction, only muons with a reconstructed track length of 10 m or more are selected. As cosmic muons are coming from above, we only expect to see downward going muons. To enforce this, the following condition to the muon's zenith angle θ is applied: $\cos\theta \geq 0.4$. Since the muon reconstruction method, described in section 4.3.2, requires an exit point, forcing the selection to require reconstructed muons removes any stopping muons that have no exit point.

The muon selection criteria are summarised in table 5.1. Figure 5.1 shows some of the distributions of the quantities that are used to select muons.

Parameter	**Select if**
nhits	≥ 150
OWL hits	≥ 5
Cleaned nhits	≥ 1238
Charge RMS	≥ 4.5 GSU
Time RMS	≤ 38 ns
DC tags	neck event burst atmospheric retrigger
Zenith angle θ of reconstructed direction	$\cos\theta \geq 0.4$
Reconstructed path length	≥ 10 m

Table 5.1: Summary of the muon selection criteria.

5.3 Neutron Selection

The neutron selection criteria are applied to any event tagged as a muon follower in processing. The fitValid condition checks whether reconstruction completed suc-

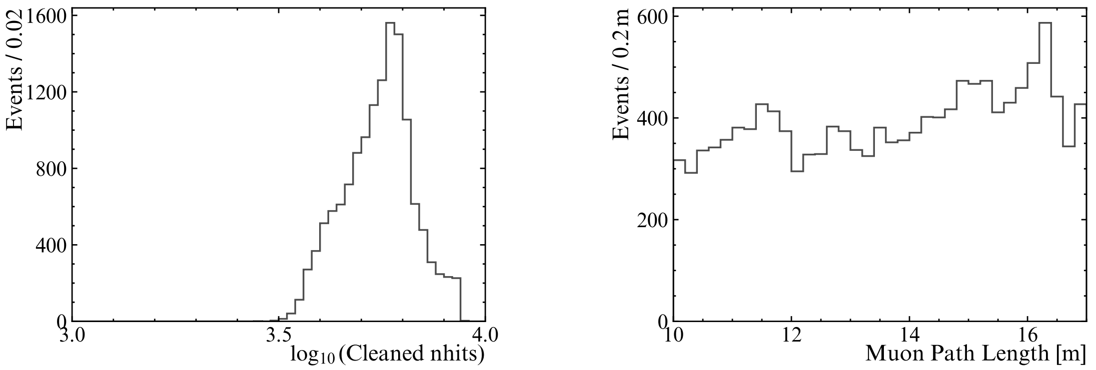

(a) Distribution of cleaned nhits for the selected muons.

(b) Distribution of muon path lengths for the selected muons.

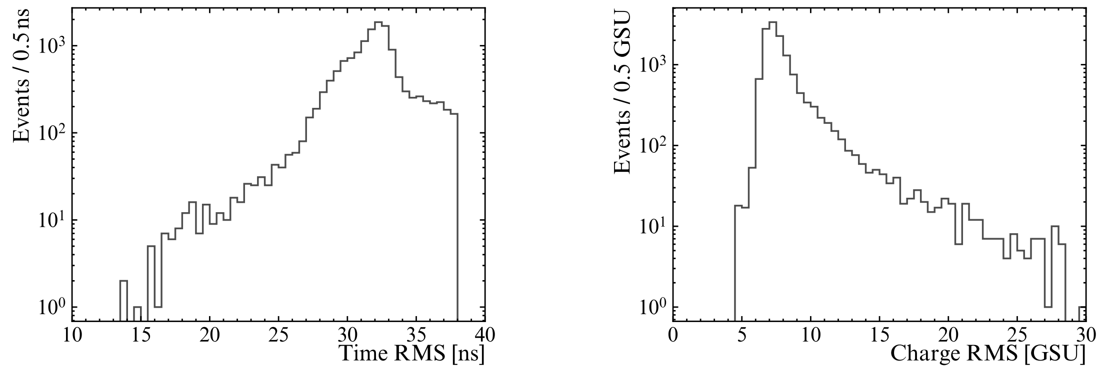

(c) Distribution of the RMS of the PMT hit times for the selected muons.

(d) Distribution of the RMS of the PMT charges for the selected muons.

Figure 5.1: Summary of the muon selection.

cessfully. To select the muon induced neutrons, a timing condition is applied to the time since muon $\Delta_\mu T$ that selects events where $10\,\mu\text{s} \leq \Delta_\mu T \leq 776\,\mu\text{s}$. A condition of $9 \leq$ inTimeHits100 ≤ 25 is applied, where inTimeHits100 is the number of in-time hits from the N100 trigger, as described in section 4.1.1. Two conditions are also applied to the fitted position so that only events within a radius $R < 8\,\text{m}$ and a distance from the muon track $\Delta_\mu R < 4.6\,\text{m}$ are selected. The neutron selection criteria are summarised in table 5.2 [1].

5.4 Event Selection Results

The event selection criteria for muons and their neutron followers, described above, were applied to the whole data set, after run selection. The total number of runs

Parameter	**Select if**
fitValid	True
$\Delta_\mu T$	$\geq 10\,\mu$s $\leq 776\,\mu$s
inTimeHits100	≥ 9 ≤ 25
$\Delta_\mu R$	$< 4.6\,$m
R	$< 8\,$m

Table 5.2: The neutron selection criteria that are applied to muon followers to select muon-induced neutrons.

analysed is 8179 which corresponds to a total live time of 321 days. After selection, $13,694$ muons remained with $1,208$ neutrons in total.

The number of muon events tagged in processing, per hour, is shown in figure 5.2a. This has been fitted with a Poisson function, given as

$$f_{poisson}(N_\mu;\mu) = \frac{\mu^{N_\mu}}{N_\mu!}e^{-\mu}, \tag{5.1}$$

where N_μ is the measured muon rate, and μ is the expected muon rate that is floated in the fit. The "raw muons" refers to the muons that were initially flagged in processing, before the additional selection criteria has been applied. Fitting the raw muon rate with this function resulted in a muon rate of $4.03 \pm 0.02\,\mu\text{hour}^{-1}$. After applying the selection criteria in table 5.1, the number of selected muons per hour is shown in figure 5.2b. This gives a fitted Poisson mean of $1.72 \pm 0.01\,\mu\text{hour}^{-1}$. The decrease in muon rate after applying the selection criteria is because the purity of the muon sample has been prioritised over efficiency. Any seasonal effects on the muon rate have not been taken into account in this analysis. Since the final result gives a yield per muon and does not depend on the muon rate, seasonal effects do not affect the final result.

Figure 5.3 shows the distribution of reconstructed muon directions in data. When compared with equation 3.7, the expected distribution of muon directions, they show good agreement up to $\cos\theta \sim 0.5$, where the data deviates. This small deviation is likely to be caused by atmospheric-induced muons.

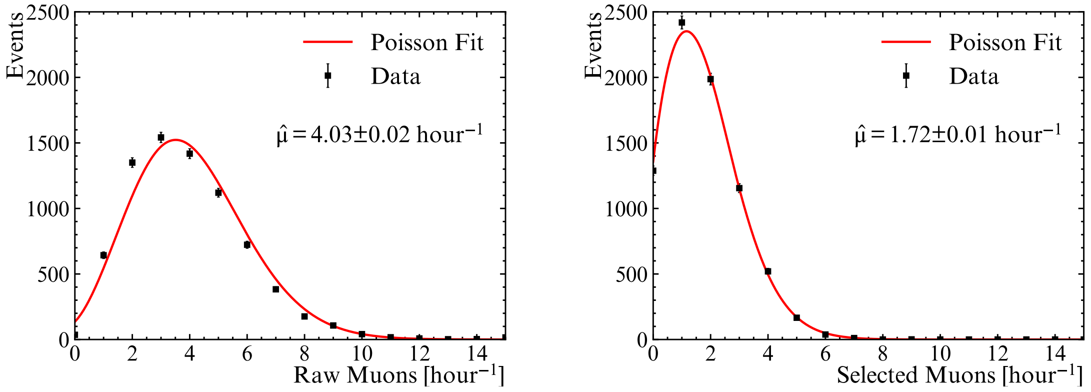

(a) The number of tagged muons per hour before selection.

(b) The number of selected muons per hour.

Figure 5.2: Muon-tagged event rates before (left) and after (right) muon selection. Both have been fitted with a Poisson function with mean μ.

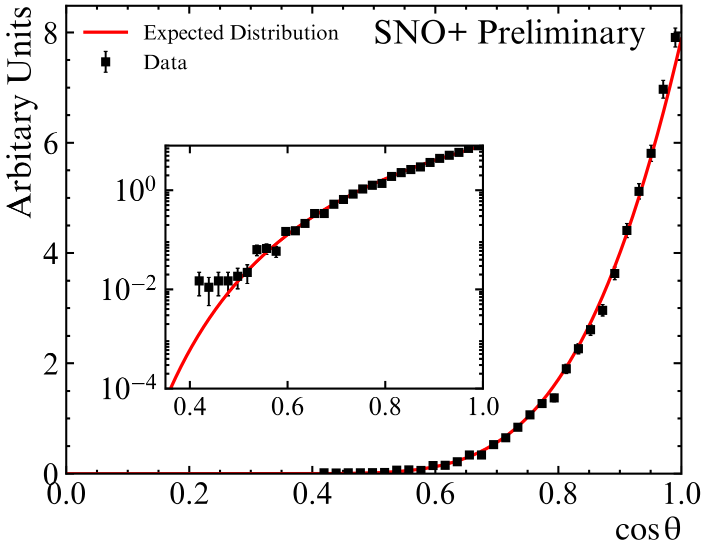

Figure 5.3: The reconstructed muon directions in data compared with the expected distribution, given by equation 3.7, shown in both linear and log scales.

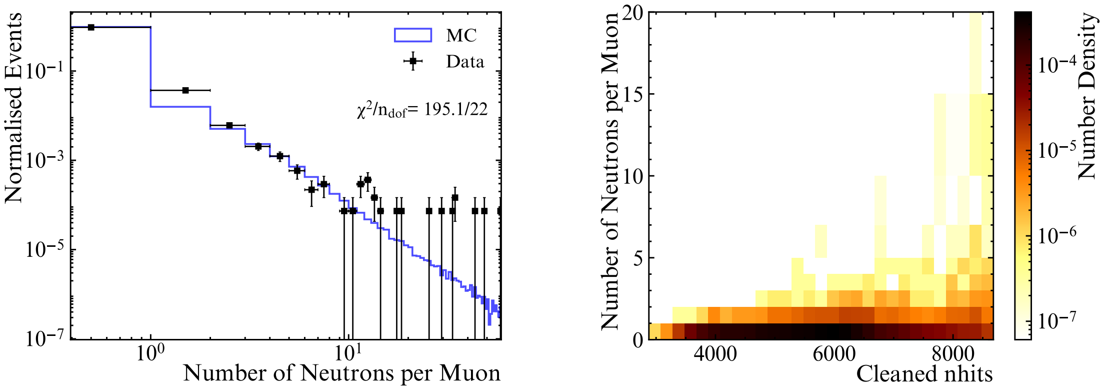

(a) The number of selected neutrons per muon in data, compared with simulation.

(b) The number of selected neutrons per muon against the number of cleaned PMT hits produced by the muon.

Figure 5.4: The number of neutrons observed after each muon (left), with a comparison to the number of cleaned PMT hits that the muon produced (right).

Figure 5.4a shows the distribution of the number of neutrons selected per muon. Most muons have zero observed neutrons associated with them. The excess of events in data with 1 neutron follower corresponds to a total of around 288 neutrons (24% of the dataset). There is another excess from events with 11 and 12 neutron followers which totals to around 88 neutrons (7.3% of the total dataset). Figure 5.4b shows how the number of observed neutrons is distributed according to the cleaned nhits of the muon. A correlation can be seen between these two quantities, where muons that have the highest number of observed neutron followers have a relatively large number of PMT hits. This could be due to either more energetic muons or muons with longer track lengths depositing more light in the detector, as well as producing more neutrons.

The time between a muon and a neutron capture event ($\Delta_\mu T$) decays exponentially, according to

$$f(\Delta_\mu T; b, A, t_n) = b + A \exp\left(-\frac{\Delta_\mu T}{t_n}\right), \tag{5.2}$$

where b is the flat background component, A is the amplitude, and t_n is the decay constant referred to as the neutron capture time. As mentioned in section 4.2.5, the neutron capture time was measured in water using the Am-Be source to be:

$t_n = 202.35 \pm 0.87\,\mu$s [42]. Figure 5.5 shows the time between the muon and the neutron capture event in data, fitted with a fixed neutron capture time equal to that measured using the Am-Be source. The fit yielded a background component of $\hat{b} = 1.93 \pm 0.53$. This corresponds to a predicted number of backgrounds of 103 ± 26, over the whole muon data set.

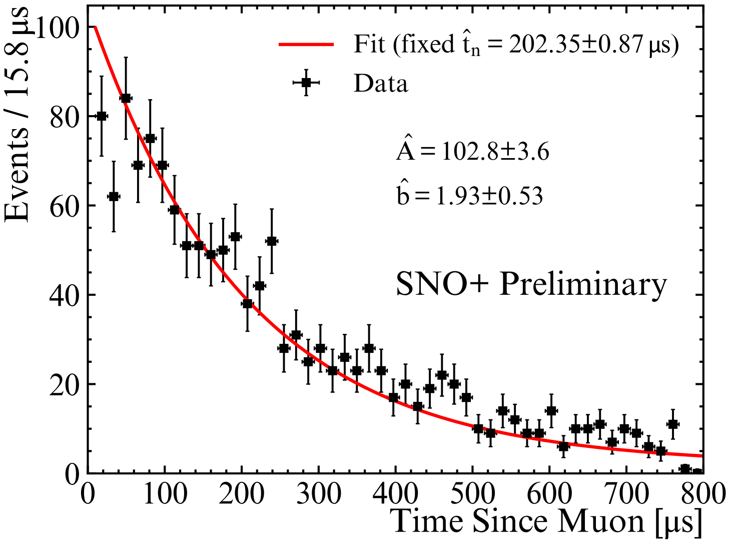

Figure 5.5: Time between muon and neutron capture events in data (black) fitted with equation 5.2 (red), with the neutron capture fixed to match the neutron capture measured using the Am-Be source [42].

Chapter 6

Backgrounds to the Cosmogenic Neutron Signal

This chapter identifies any events that may be wrongly tagged as a muon-induced neutron. There are two main sources of background to consider. The first is from products produced in cosmic muon spallation that are not neutrons, but mimic the neutron signal. The analysis of these backgrounds was performed by Billy Liggins in [1] and is given in section 6.1. The second is from events that are intrinsic to the detector, and for which an out of window rate must be found, as described in section 6.2.

6.1 Muon Correlated Backgrounds

Muon correlated backgrounds are events which coincide with the muon and incorrectly pass the selection criteria. Among the neutrons, a muon can also produce radioactive isotopes which can mimic the neutron capture signal when they decay. In [65], the yields of background spallation isotopes per muon were calculated using simulation. In [1], Billy Liggins used these production yields to calculate the expected number of events per muon that pass the neutron selection criteria in table 5.2. The results are shown in table 6.1.

The probability that an event passes the inTimeHits100 condition P_{hits} was calculated using simulations of each isotope. The probability that an event passes the timing condition P_{time} was calculated using the decay curves for the given half-lives. These probabilities can be found table 6.1. Isotopes which decay with a similar energy to the neutron capture signal tend to have a half-life that is much longer than the neutron capture time window. On the other hand, isotopes with a half-life similar to the neutron capture time will decay with much higher energies, exceeding the hit selection for neutron capture.

The final number of expected background events per muon was found to be 8472.32×10^{-10}. Due to this extremely small number, this contribution is considered to be negligible. Although SK experiences a lower average muon energy than SNO+, this background contribution remains negligible even if the yield is increase by three orders of magnitude [1].

6.2 Random Backgrounds

Random backgrounds are events that occur in coincidence with a muon, and are associated with the pool of intrinsic events that occur within the detector. The rate of these events is evaluated outside the muon time window. If an event occurs within the muon's fiducial volume, defined by the spatial selection criteria, it is counted towards the random background rate. The fiducial volume will depend on where the muon traverses the detector, so the rate is found calculated on a muon-by-muon basis. This rate is then multiplied by the length of the muon time window to give an estimate for the number of events that may have been accidentally tagged as a muon follower.

As mentioned in section 5.1, 10% of all events, with between 9 and 25 inTimeHits100, that are not tagged as a muon or muon follower are reconstructed for the purpose of measuring the random background rate. Of the events successfully reconstructed, those with a reconstructed radial position of 8 m or more are removed. The events are collected across each run and the perpendicular distance between each event and the muon track is calculated for any muon in that run. If this distance is less than

Isotope	$T_{1/2}$ (s)	Y^{μ} ($10^7 \mu^{-1}\text{m}^2\text{kg}^{-1}$)	P_{hits} (10^{-3})	P_{time} (10^{-4})	N^{μ} (10^{-10})
^{18}N	0.62	0.02	2.00	15.85	0.11
^{17}N	4.17	0.59	4.17	2.37	0.99
^{16}N	7.13	18.00	1.71	1.39	7.26
^{16}C	0.75	0.02	10.59	13.24	0.48
^{15}C	2.45	0.82	2.84	4.04	1.60
^{14}B	0.01	0.02	0.00	691.76	0.00
^{13}O	0.01	0.26	1.59	1086.11	76.13
^{13}B	0.02	1.90	3.19	552.76	568.92
^{12}N	0.01	1.30	1.29	859.91	244.27
^{12}B	0.02	12.00	3.23	478.05	3150.06
^{12}Be	0.02	0.10	4.20	410.64	29.30
^{11}Be	13.80	0.81	2.94	0.72	0.29
^{11}Li	0.01	0.01	0.50	1098.14	0.94
^{9}C	0.13	0.89	1.60	77.64	18.81
^{9}Li	0.18	1.90	2.05	55.46	36.80
^{8}B	0.77	5.80	0.72	12.85	9.10
^{8}Li	0.84	13.00	0.83	11.81	21.54
^{8}He	0.12	0.23	4.97	82.84	16.11
^{15}O	122.24	351.00	750.00	0.08	3624.41
^{14}O	70.20	13.00	160.77	0.14	50.11
^{11}C	1220.04	105.00	1000.00	0.01	144.84
^{10}C	19.29	7.60	628.57	0.51	416.78
^{13}N	597.90	19.00	1000.00	0.02	53.48
Total events per muon					8472.32×10^{-10}

Table 6.1: Each spallation isotope that is a candidate for passing the neutron selection criteria with their half-lives $T_{1/2}$, the yield per muon Y^{μ}, the probability of an event passing the inTimeHits100 condition P_{hits}, and the probability of an event passing the timing condition P_{time}. The final column gives the expected number of events per muon N^{μ} which has been summed at the bottom. Taken from Table 8.5 of [1].

4.6 m then the event is counted towards the random background rate for that run. This rate can then be used to find the expected number of random backgrounds during the muon time window: $10\mu\text{s} \leq \Delta_{\mu}T \leq 776\mu\text{s}$. If N_{run} is the total number of random background events in a run of length T_{run} [s], the number of expected random background events in the muon time window is given by

$$B_R^{\mu} = 10 N_{\text{run}} \frac{766 \times 10^{-6}\ [\text{s}]}{T_{\text{run}}\ [\text{s}]}, \tag{6.1}$$

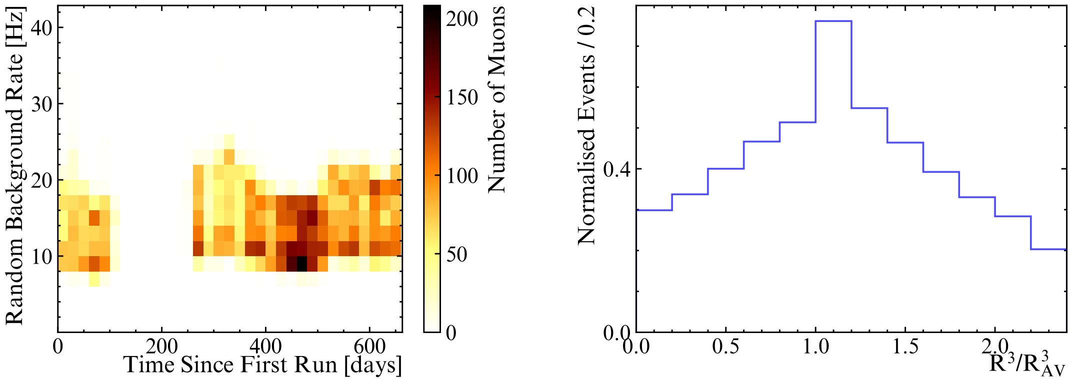

(a) Distribution of random backgrounds in time. The gap in time is due to the installation of the cover gas system

(b) Volume-weighted radial distribution of random backgrounds. $R_{\mathrm{AV}} = 6\,\mathrm{m}$ is the radius of the AV.

Figure 6.1: How the random backgrounds are distributed in time (left) and radius (right).

and the uncertainty is given by

$$\sigma_{BR\mu} = 10\sqrt{N_{\mathrm{run}}}\frac{766 \times 10^{-6}\ [\mathrm{s}]}{T_{\mathrm{run}}\ [\mathrm{s}]}. \tag{6.2}$$

In total, there are 150 ± 2 random backgrounds in coincidence with a muon.

The distributions of the random backgrounds, selected in data, in time and radius are shown in figure 6.1. Although figure 6.1a shows that the random backgrounds are approximately flat in time, figure 6.1b shows that the random backgrounds are not distributed isotropically within the detector. The distribution appears to increase with radius up to the radius of the AV, after which it begins to decrease. The consequence of this is a distribution of distances between the random background events and the muon track as shown in figure 6.2. Figure 6.3 shows the inTimeHits100 of the selected random background events.

6.3 Chapter Summary

This chapter has evaluated the contributions to the background of the cosmogenic neutrons. These contributions can be placed into one of two categories. The first category is backgrounds due to other cosmic muon spallation products. This was

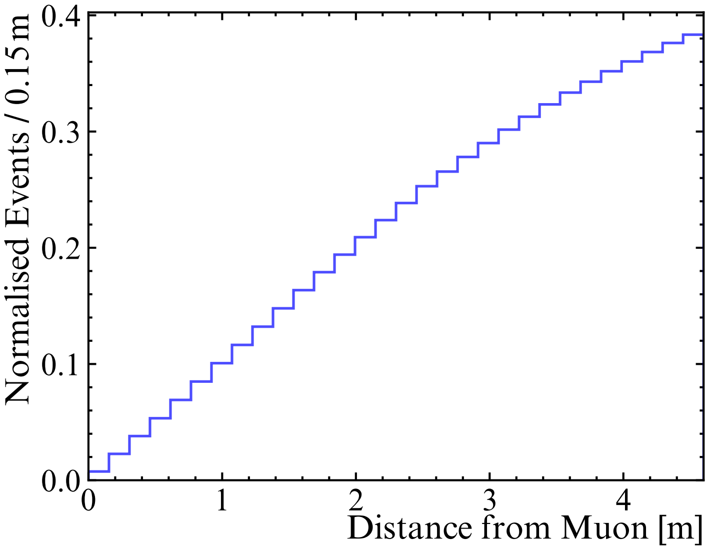

Figure 6.2: The perpendicular distance between the muons and the random background events selected from data.

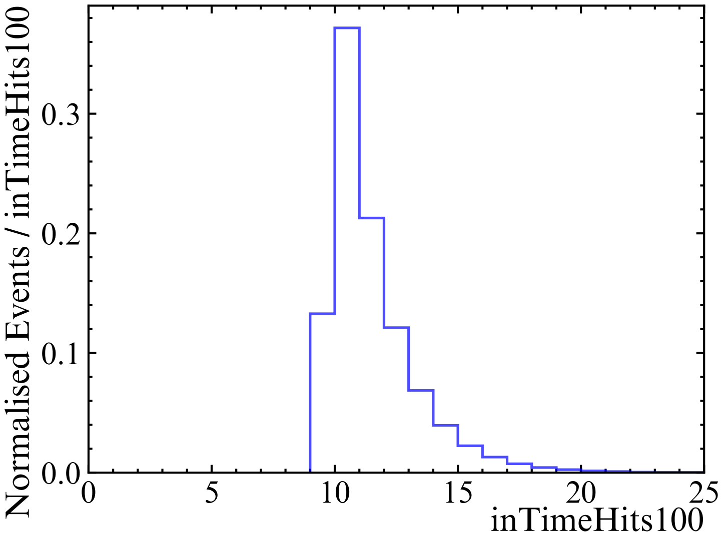

Figure 6.3: The inTimeHits100 of the random background events selected from data.

analysed in [1], a summary of which is presented in section 6.1. After using some pre-calculated yields and the probabilities of events passing the neutron selection criteria from simulation, an expected total of 8472.32×10^{-10} events per muon was found. This is considered to be negligible.

The second contribution is due to intrinsic events in the detector that can sometimes pass the neutron selection criteria. This is evaluated outside the muon time window to give a rate of these events. This rate is then multiplied by the muon time window to give a number of expected events per muon. The details for how this was done is shown in section 6.2. The data-driven total number of events across all muons was calculated to be 150 ± 2, which is of the same order of magnitude as the 103 ± 26 events predicted from fitting the time since muon in figure 5.5. Although the values do not agree, the data-driven value of 150 ± 2 will be used going forward, as the neutron capture time fit approach was simply to give an estimate of the number of expected background events.

Chapter 7

Neutron Selection Efficiency

The neutron selection efficiency, introduced in equation 3.11, relates the number of observed neutrons to the true number of neutrons in water. It is defined as the number of neutrons which pass the neutron selection criteria over the total number of neutrons along the muon path, in water. This is expected to be low in water due to the low number of PMTs hit during a neutron capture, making them easy to miss. A positional dependence in the neutron selection efficiency was observed during the Am-Be calibration [42]. This means that the neutron selection efficiency must be calculated on a muon-by-muon basis. The method for this will be outlined in the first section of this chapter. This method will require some intermediate steps that will be covered in the following two sections.

The final neutron selection efficiency results will be presented in section 7.4. The final section will discuss and calculate the different contributions to the uncertainty in the efficiency.

7.1 Method

For each muon in data, the neutron selection efficiency will be calculated using simulations of the muon. From these event-by-event simulations, truth and reconstruction information can be extracted, with the neutron selection criteria applied to the reconstruction information. The reconstruction information will take into account detector conditions, simulated trigger efficiency, and the uncertainty in reconstructing the positions of neutron captures.

The neutron selection efficiency will be affected by muon misreconstruction, which will need to be included in the neutron selection efficiency uncertainty. This is due to the shift in position it causes to the fiducial volume that defines the neutron selection. In order to take into account the effect this has on the efficiency, each muon in data will be smeared. In this context, a smeared muon is a muon that has had its initial position and direction displaced within the reconstruction uncertainty, so that the result is a track moved from the original reconstructed track. A detailed description of this process can be found in section 7.2. Each muon in data has been smeared 50 times, and, in order to produce enough neutrons, each smear is simulated $2,000$ times. These numbers have been optimised to reduce the statistical uncertainty and standard deviation of the efficiencies between smears, while keeping the computational time to a manageable amount.

As already alluded to, computational time must be considered for the event-by-event muon simulations. Due to the many processes induced by a muon, and the large amount of photons produced, simulating a muon can be computationally intense. A lot of time and memory are taken up by these simulations, and the method for calculating the efficiency must be adapted to work around this. For this reason, the event-by-event muon simulations are performed with no photon tracking. Muon simulations with no photon tracking take approximately 10-15 minutes per $1,000$ muons. A consequence of not tracking the photons is that the neutron captures can no longer be reconstructed. The solution to this comes from sampling PDFs generated using simulated 2.2 MeV gammas. This method is outlined in section 7.3.

The following outlines the method for calculating the neutron selection efficiency for a single muon from data, taking all of the above into consideration:

1. Smear the initial position and direction of the muon 50 times (see section 7.2)

2. Use the smeared initial positions and directions as inputs for muon simulations - each smeared muon is simulated $2,000$ times with photon tracking turned off

3. From the simulations, the true positions of any neutron captures that occur in water and along the muon track are collected to give the total number of neutrons N_{tot}, per smear
4. Using the true positions, a reconstructed position for the neutron capture is found from sampling the reconstruction PDFs (see section 7.3)
5. Apply the neutron selection criteria (table 5.2) to the reconstructed neutrons to get the number of passed events n_{pass}, per smear
6. Collect the total number of neutrons and number of passed neutrons across all $2,000$ simulations of each smeared muon, and calculate the neutron selection efficiency per smear s: $\varepsilon_s^\mu \pm \Delta\varepsilon_s^\mu$ using

$$\varepsilon_s^\mu = \frac{n_{pass}+1}{N_{tot}+2} \tag{7.1}$$

$$\Delta\varepsilon_s^\mu = \sqrt{\frac{(n_{pass}+1)(n_{pass}+2)}{(N_{tot}+2)(N_{tot}+3)} - \left(\frac{n_{pass}+1}{N_{tot}+2}\right)^2}, \tag{7.2}$$

which assumes Bayesian statistics [66]

7. Calculate the weighted average of the neutron selection efficiencies across all muon smears associated to the original data muon using

$$\varepsilon^\mu = \frac{\sum_{s=1}^{50} \varepsilon_s^\mu/(\Delta\varepsilon_s^\mu)^2}{\sum_{s=1}^{50} 1/(\Delta\varepsilon_s^\mu)^2} \tag{7.3}$$

This method gives a neutron selection efficiency per muon, and is carried out for each muon in data.

7.2 Muon Smearing

As discussed in the overview above, the misreconstruction of muons is accounted for by smearing the initial positions and directions of the reconstructed muons from data. The muons should only be smeared within the reconstruction uncertainty for the initial position and direction. This is done by sampling the correlated initial position and direction reconstruction resolutions, as shown in figure 7.1. Figure 7.1 has been created by applying the muon fitter to a sample of MC-generated muons, simulated in the SNO+ detector with photon tracking enabled. These MC-generated muons randomly sample their direction and energy from figure 3.6, as described in section 3.3.1. Around 50,000 muons were generated, and the resolutions for reconstructing the initial position and direction were found. The resolution is given by the angle between the true value and the reconstructed value.

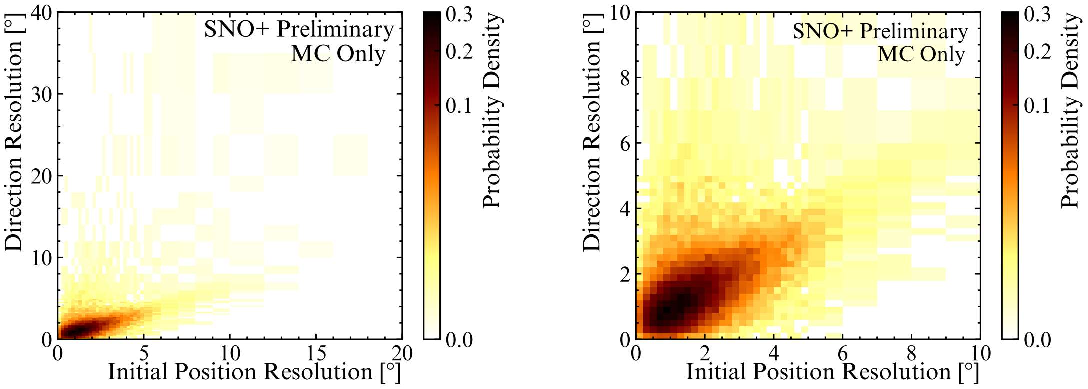

Figure 7.1: The correlation between the initial position and direction resolutions of the muon water fitter applied to MC-generated muons. The plot on the right is a zoomed in version of the plot on the left.

The correlation between the initial position and direction reconstruction resolutions should be included when smearing the muons. This is enforced when the two-dimensional histogram, from figure 7.1, is sampled using the inverse transinformation sampling method [67]. This method moves through the bins in the y-axis, and then along x-axis to give a cumulative density function (CDF) for each bin. A random number is then thrown and the last bin where the CDF is less than that random number is found. That bin is then uniformly sampled independently in x and y. The result is two angles: one to smear the initial position vector of the muon from data, and one to smear the direction vector of the muon from data.

7.3 Reconstructing Neutrons via Sampling

Since the event-by-event muon simulations are run with no photon tracking, there is no reconstruction information for the neutrons. Instead, a reconstructed position and reconstruction efficiency are sampled from PDFs, based on the true position of the neutron captures from the event-by-event muon simulations. The PDFs have been generated using 2.2 MeV gammas that have been simulated isotropically in the detector. A condition that only events simulated with $9 \leq \text{inTimeHits100} \leq 25$ are reconstructed was applied. This condition enforces the neutron selection for the inTimeHits100. Of the $\sim 9,400,000$ events simulated, around $2,300,000$ were reconstructed. Reconstruction of these simulated gammas was performed using the point-like reconstruction method that is described in section 4.3.1.

7.3.1 Reconstruction Efficiency

Not all events are successfully reconstructed. Firstly, the event has to trigger the detector, and secondly, the reconstruction algorithm has to run successfully. The reconstruction efficiency is the probability that an event has been reconstructed. This is found for different positions in the detector using the 2.2 MeV gammas that have been MC-generated isotropically in the detector. A simulated gamma is only reconstructed if the event passes the condition $9 \leq \text{inTimeHits100} \leq 25$, from the neutron selection criteria. This enforces the inTimeHits100 neutron selection condition when the reconstruction efficiency is applied to neutron captures from the event-by-event muon simulations.

The space, in which the 2.2 MeV gammas have been simulated, has been binned in radius ρ and zenith angle θ. The reconstruction efficiency per bin is calculated using

$$\varepsilon_{\text{bin}} = \frac{k_{\text{bin}} + 1}{N_{\text{bin}} + 2}, \tag{7.4}$$

with the error calculated using

$$\Delta\varepsilon_{\mathrm{bin}} = \sqrt{\frac{(k_{\mathrm{bin}}+1)(k_{\mathrm{bin}}+2)}{(N_{\mathrm{bin}}+2)(N_{\mathrm{bin}}+3)} - \left(\frac{k_{\mathrm{bin}}+1}{N_{\mathrm{bin}}+2}\right)^2}, \tag{7.5}$$

where k_{bin} is the number of reconstructed events in that bin, and N_{bin} is the total number of events generated in that bin. This method for calculating the efficiency uses Bayesian statistics [66]. The spatial binning has been optimised so that jumps in the reconstruction efficiency are minimal between bins. Figure 7.2 shows the result after binning.

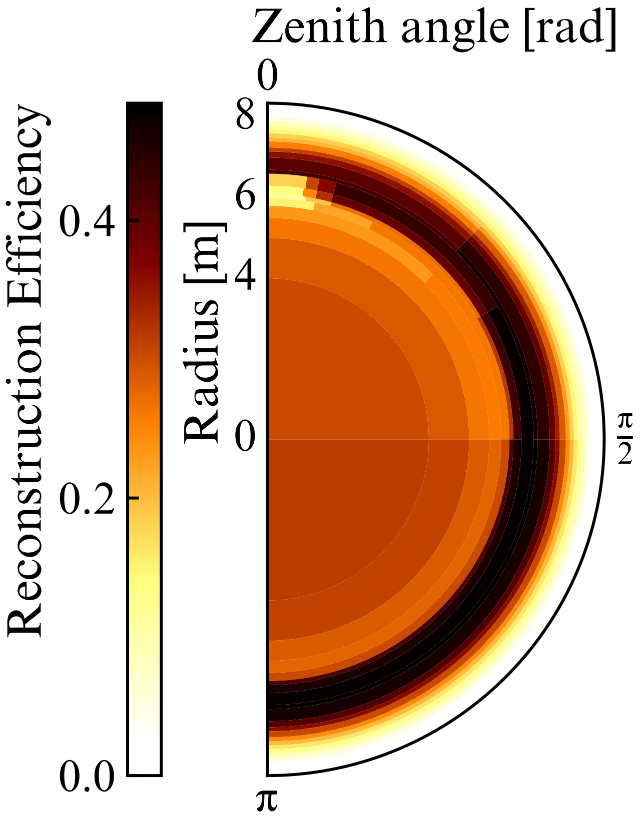

Figure 7.2: The reconstruction efficiency for different bins in radius and zenith angle, produced using simulated 2.2 MeV gammas.

Moving through the radial bins in figure 7.2, the reconstruction efficiency increases with radius up to around 7 m, after which it rapidly decreases. The reconstruction efficiency near the centre of the detector is low because the light has to travel further before reaching the PMTs. This increase in distance means the light is more likely to scatter, and the event may be missed by the detector. This becomes less of a problem moving closer to the PMTs however, at very close distances, the angular response of the PMTs is very poor, and the events are less likely to be reconstructed. This is due to the relatively low light collection at large incidence angles. The change in reconstruction efficiency with θ, at constant radius, is small, but there is an overall increase moving towards $\theta = \pi\,\text{rad}$. This is due to shadowing from the neck at the top of the AV.

7.3.2 Reconstructed Position

The position resolution is the difference between the true and reconstructed event position. This is split up into the x, y and z Cartesian coordinates. As with the reconstruction efficiency, the detector is divided into bins in radius and zenith angle, and a PDF of resolutions is generated per bin. The PDF is generated by fitting a function to the distribution of reconstruction resolutions. For the resolutions in the x and y coordinates, a linear combination of the normal distribution $f_{\text{norm}}(X)$ and the generalised normal distribution $f_{\text{gennorm}}(X;\beta)$ is used, as shown in

$$f(X;\alpha,\beta) = \alpha f_{\text{norm}}(X) + (1-\alpha) f_{\text{gennorm}}(X;\beta). \tag{7.6}$$

The distributions $f_{\text{norm}}(X)$ and $f_{\text{gennorm}}(X;\beta)$ are given by

$$f_{\text{norm}}(X) = \frac{\exp\left(-X^2/2\right)}{\sqrt{2\pi}}, \tag{7.7}$$

$$f_{\text{gennorm}}(X;\beta) = \frac{\beta}{2\Gamma(1/\beta)} \exp\left(-|X|^{\beta}\right), \tag{7.8}$$

respectively. The parameters α and the β are floated to fit the resolution data X. In both x and y coordinates, bin 1 (figures 7.3b and 7.4b) shows a sharper, more narrow distribution than bin 2 (figures 7.3c and 7.4c). This is because reconstruction performs worse near the edge of the detector due to the scattering of light which must travel further to get across to detector.

The resolutions in the z coordinates also show broader distributions at high radii, however the distributions are slightly asymmetric due to the effects of the neck. The neck affects reconstruction more for events directly below the neck, hence the greatest amount of asymmetry is observed in bins 2 and 7 (figures 7.5c and 7.5h, respectively). The asymmetry in the outer radial bins means that the distributions in z require a different function for the fitting. In this case the data X is fitted with a linear combination of the normal distribution and the asymmetric Laplace distribution $f_{\text{lap-asym}}(X;\kappa)$. This gives

$$f(X;\alpha,\kappa) = \alpha f_{\text{norm}}(X) + (1-\alpha) f_{\text{lap-asym}}(X;\kappa), \tag{7.9}$$

where κ and α are the parameters floated in the fit, and $f_{\text{lap-asym}}(X;\kappa)$ is given by

$$f_{\text{lap-asym}}(x;\kappa) = \begin{cases} \frac{1}{\kappa+\kappa^{-1}} \exp\left(-X\kappa\right), & X \geq 0 \\ \frac{1}{\kappa+\kappa^{-1}} \exp\left(X/\kappa\right), & X < 0. \end{cases} \tag{7.10}$$

The results of fitting the position resolution PDFs in x, y, and z are summarised in figures 7.3, 7.4 and 7.5, respectively.

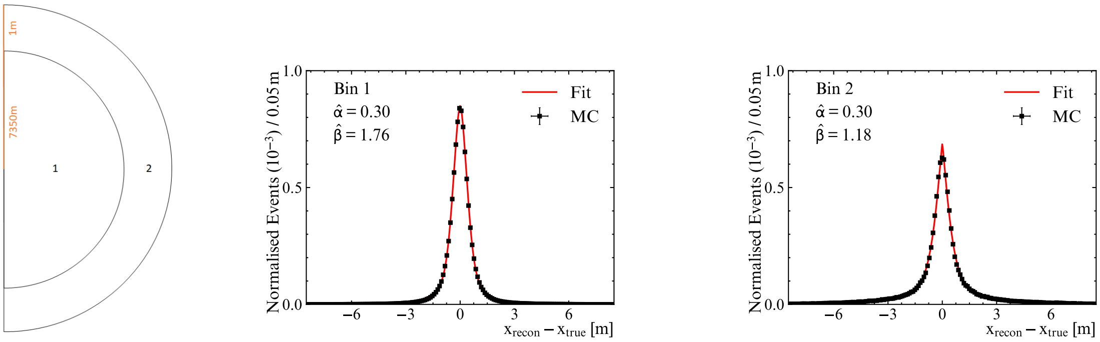

(a) Bin structure.

(b) Bin 1: $x_{\text{recon}} - x_{\text{true}}$.

(c) Bin 2: $x_{\text{recon}} - x_{\text{true}}$.

Figure 7.3: (b) and (c) show the difference between the reconstructed position and true position in the x plane in bins 1 and 2 of the binning represented in (a), respectively. The red shows the fit using equation 7.6.

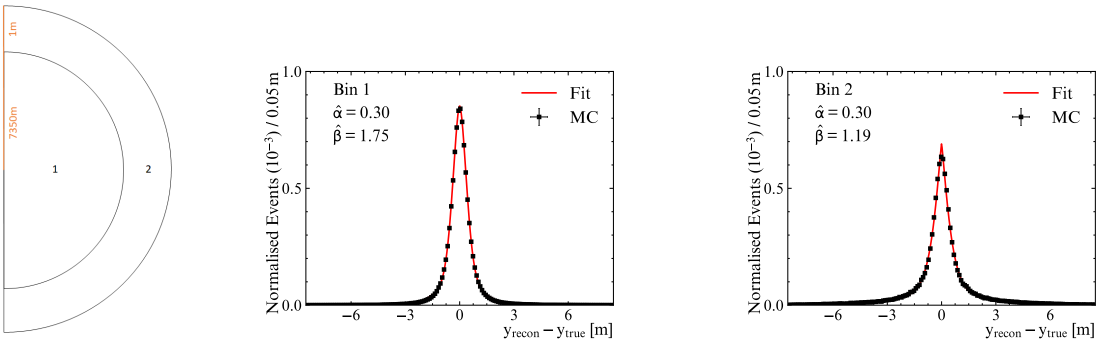

(a) Bin structure.

(b) Bin 1: $y_{\text{recon}} - y_{\text{true}}$.

(c) Bin 2: $y_{\text{recon}} - y_{\text{true}}$.

Figure 7.4: (b) and (c) show the difference between the reconstructed position and true position in the y plane in bins 1 and 2 of the binning represented in (a), respectively. The red shows the fit using equation 7.6.

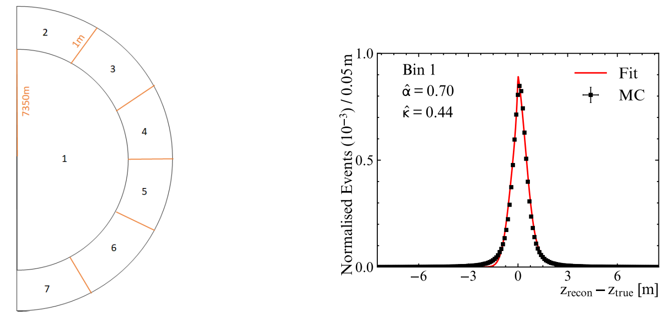

(a) Bin structure.

(b) Bin 1: $z_{\text{recon}} - z_{\text{true}}$.

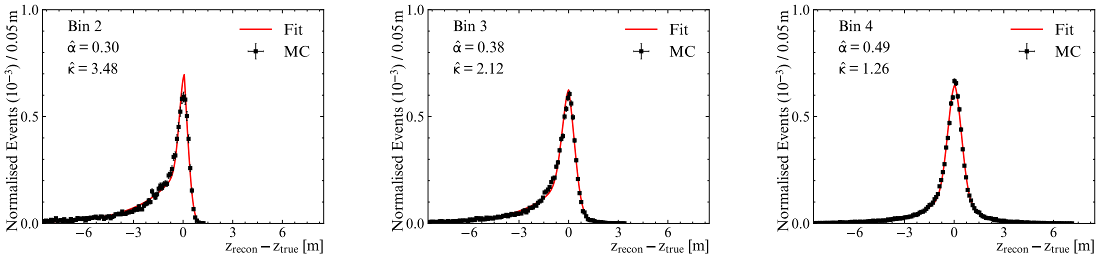

(c) Bin 2: $z_{\text{recon}} - z_{\text{true}}$.

(d) Bin 3: $z_{\text{recon}} - z_{\text{true}}$.

(e) Bin 4: $z_{\text{recon}} - z_{\text{true}}$.

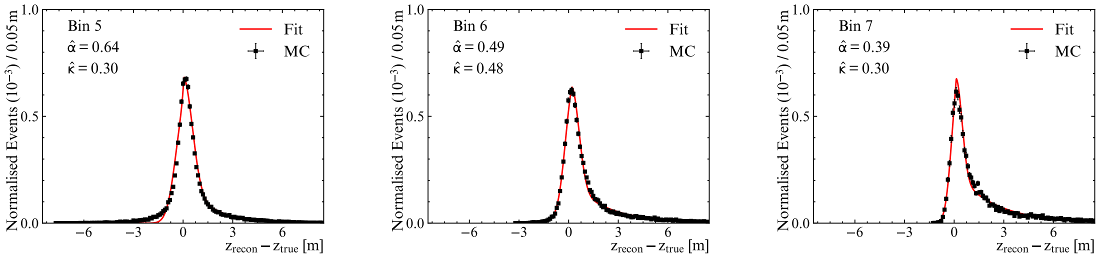

(f) Bin 5: $z_{\text{recon}} - z_{\text{true}}$.

(g) Bin 6: $z_{\text{recon}} - z_{\text{true}}$.

(h) Bin 7: $z_{\text{recon}} - z_{\text{true}}$.

Figure 7.5: (b-h) show the difference between the reconstructed position and true position in the z plane in bins $1-7$ of the binning represented in (a), respectively. The red shows the fit using equation 7.9.

7.4 Neutron Selection Efficiency Results

The method for calculating the neutron selection efficiency was carried out for approximately 10% of the muons in data. This sample covers the whole time period of the water data, and the whole range of muon path lengths, as shown in figure 7.6. The neutron selection efficiencies from this sample have then been binned according to the reconstructed track length of the muon, as shown in figure 7.7. Within each 0.5 m bin, the weighted average efficiency is calculated. The relative difference between each value within a bin and the efficiency given by that bin is known as the residual. The error in each bin's neutron selection efficiency is given by the width of the Gaussian fitted residuals for that bin. Each muon in the entire data set will be assigned a neutron selection efficiency and uncertainty according to the bin their track length falls within.

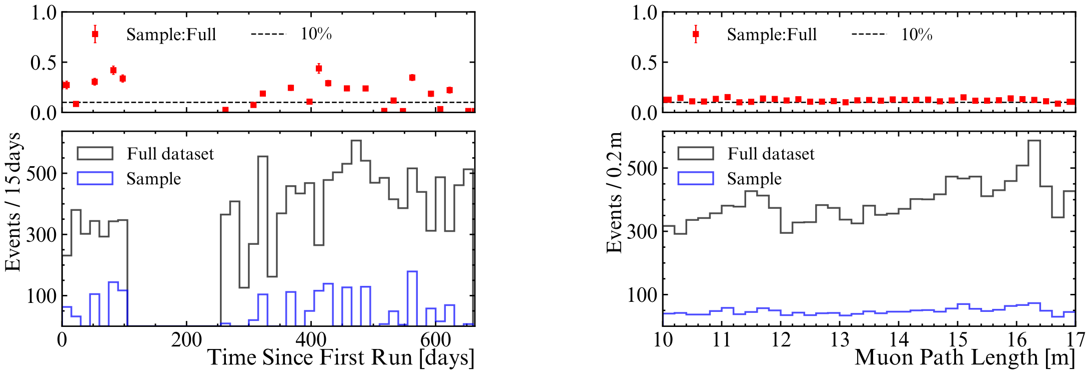

(a) Comparison of the distribution of muons over time in the full dataset (black) with the distribution in the 10% sample (blue), and the ratio of the sample over the full dataset for each bin (red).

(b) Comparison of the distribution of muon path lengths in the full dataset (black) with the distribution in the 10% sample (blue), and the ratio of the sample over the full dataset for each bin (red).

Figure 7.6: The 10% sample from the full dataset of muons used for the neutron selection efficiency calculations. The top panels show the ratio between the 10% sample and the full dataset.

7.5 Systematic Uncertainty in the Efficiency

Systematic uncertainties are inherent biases in measurements that cause a shift to the result. For any measured quantity, there may be several sources of systematic

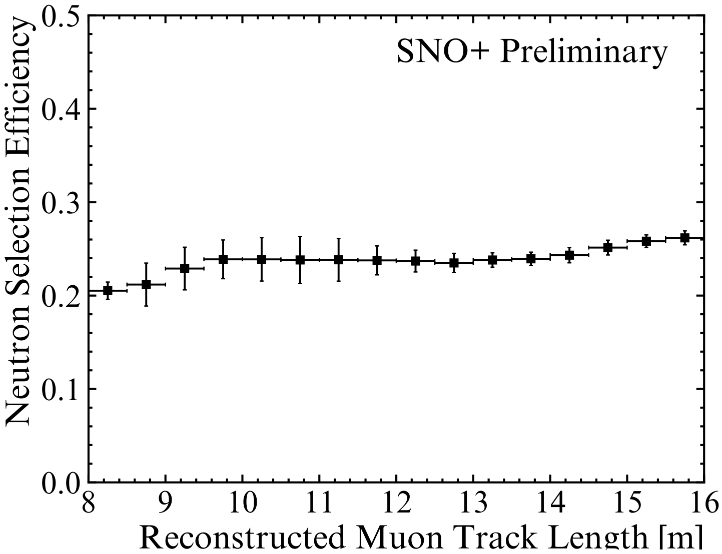

Figure 7.7: The selection efficiency of neutron captures in water against the reconstructed track length of the muon, for 10% of the muons in data, binned according to the reconstructed track length of the muon.

uncertainty that each contribute to an overall uncertainty. This section explores the different contributions to the systematic uncertainty in the neutron selection efficiency.

7.5.1 Uncertainty due to Spread in the Efficiency

As already discussed, there is an uncertainty due to the spread in the neutron selection efficiencies within each bin. The source of the spread in the efficiencies is a combination of random statistical fluctuations and the smearing of the muons. This means that this uncertainty includes the uncertainty due to the misreconstruction of muons. The uncertainty has been quantified by fitting the residuals of each bin to a Gaussian. The standard deviation of the fit is taken as the spread of the residuals, and multiplying this by the neutron selection efficiency gives the uncertainty in the efficiency for that bin. Each muon in data will be assigned the uncertainty of the bin their reconstructed track length falls within.

7.5.2 Uncertainty due to the Modelling of Neutrons

Another source of uncertainty comes from the modelling of the neutrons and neutron captures in the simulations. The two ways in which this could affect the efficiency are that the neutrons in simulation may travel a greater or shorter distance before being captured, or the neutron capture event produces more or less PMT hits. Both of these contributions to the uncertainty can be constrained using data, as shown below.

Comparing Simulation and Data

A comparison between the data and simulation has been made for the inTimeHits100 in figure 7.8a, and the perpendicular distance between the muon track and the neutron capture event in figure 7.8b. Both plots have been corrected for the random backgrounds using figure 6.3 and figure 6.2, respectively. In this correction, the data-derived random background is subtracted from the data points using the ratio of the number of random backgrounds over the total number of neutrons (150/1412).

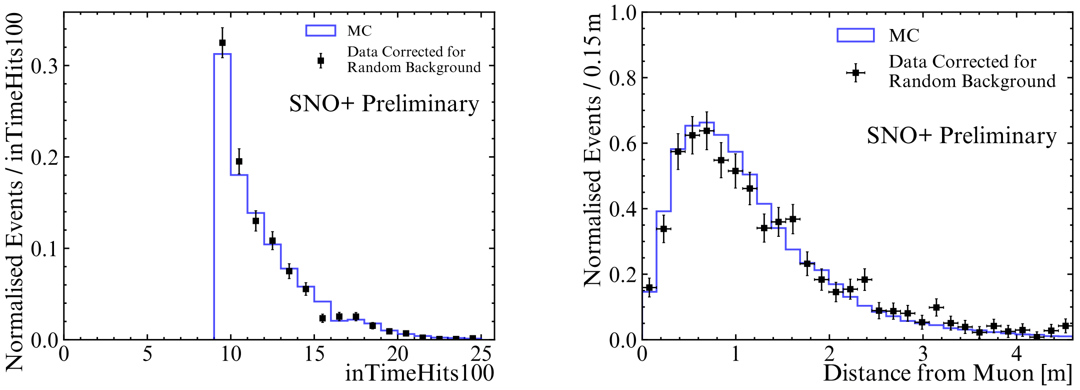

(a) The inTimeHits100 of the neutron capture events in data (black) and the simulation of 2.2 MeV gammas (blue).

(b) The perpendicular distance between the muon track and the neutron capture events in data (black) and in the muon simulations (blue).

Figure 7.8: Comparisons of the neutrons selected in data and the neutron captures produced in simulations. In both plots, the data has been corrected for the respective distributions in the selected random background events.

Distance Travelled by the Neutrons

Figure 7.8b above compares the perpendicular distance travelled by the neutron before capturing, for both simulation and data. This quantity is used to select the neutrons. If the simulation incorrectly models the distance travelled by the neutrons, the neutron selection efficiency would be calculated incorrectly. However, the comparison shown in figure 7.8b suggests that the data and simulations match well, and this could be used to constrain the uncertainty in the model. The following procedure outlines how this data-driven constraint is quantified.

To constrain the systematic uncertainty using data, each perpendicular distance travelled by each neutron in simulation is multiplied by a "scale factor". The neutron selection criteria is then applied to these scaled neutrons. The χ^2 between the data and scaled simulations is then calculated. The general equation for the χ^2 is

$$\chi^2 = \sum_{i=1}^{N} \frac{(n_i - \nu_i)^2}{\sigma_i^2}, \tag{7.11}$$

where $\mathbf{n} = (n_1, ..., n_N)$ is the set of measurements, $\boldsymbol{\sigma} = (\sigma_1, ..., \sigma_N)$ are the errors for $\mathbf{n}$, and $\boldsymbol{\nu} = (\nu_1, ..., \nu_N)$ is the set of predictions. In the case of comparing scaled MC and the data, $\mathbf{n}$ are the values from data, $\boldsymbol{\sigma} = (\sqrt{n_1}, ..., \sqrt{n_N})$ are the uncertainties, and $\boldsymbol{\nu}$ are the values of the scaled MC.

The scaling of the MC is repeated and the χ^2 is calculated for different scale factors. The results for this are shown in figure 7.9, where the plot has been fitted with a quadratic that has a minimum, with a 1σ error interval, of 1.07 ± 0.03. Figure 7.10 shows the effect of applying this scale factor to the distance from muon data-MC comparison.

A scale factor of greater than one will cause less neutrons to capture within the fiducial volume, and so less neutrons will pass the selection criteria. This will cause the neutron selection efficiency to decrease. Figure 7.11 shows how changing the scaling on the distance travelled by the neutrons affects the neutron selection efficiency. As expected, increasing the scale factor causes an overall down shift in

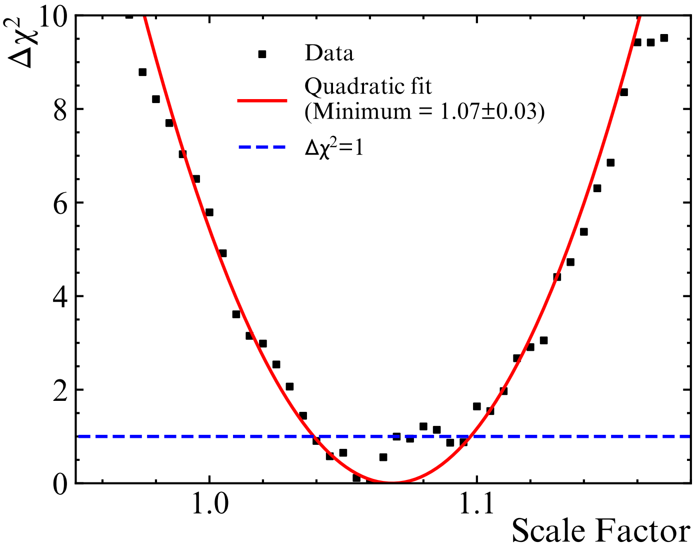

Figure 7.9: How the χ^2 between data and simulation changes when different scale factors are applied to the distance travelled by neutrons in simulation. The points (black) have been fit with a quadratic (red) which has a minimum at 1.07 ± 0.03.

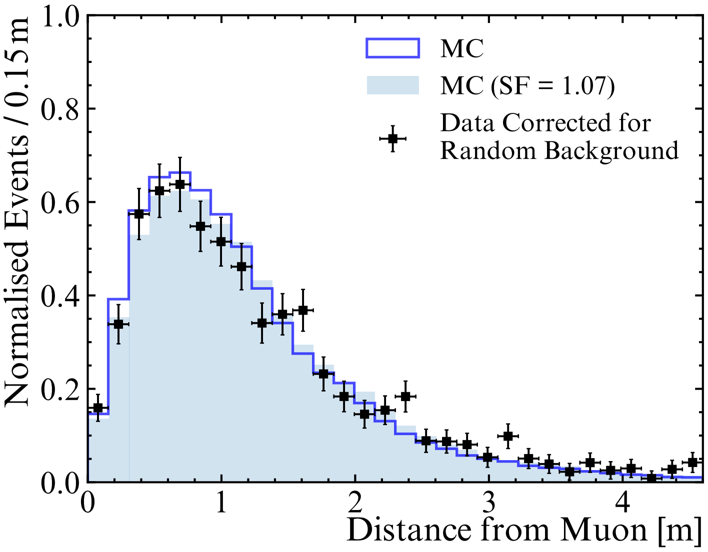

Figure 7.10: A comparison between the data (black), the non-scaled MC (blue, empty), and the MC with a scale factor of 1.07 applied (blue, filled) for the perpendicular distance between the muon track and the neutron capture event. The MC is scaled by multiplying each simulated neutron's perpendicular distance by the scale factor, then passing the neutron selection criteria over them.

the bin values. The down shift is greater at shorter muon track lengths, most likely due to muons with shorter track lengths being closer to the edge of the fiducial volume, where it is easier for neutrons to escape the selection cuts. The correction to the neutron selection efficiency from this study will be referred to as the Distance correction.

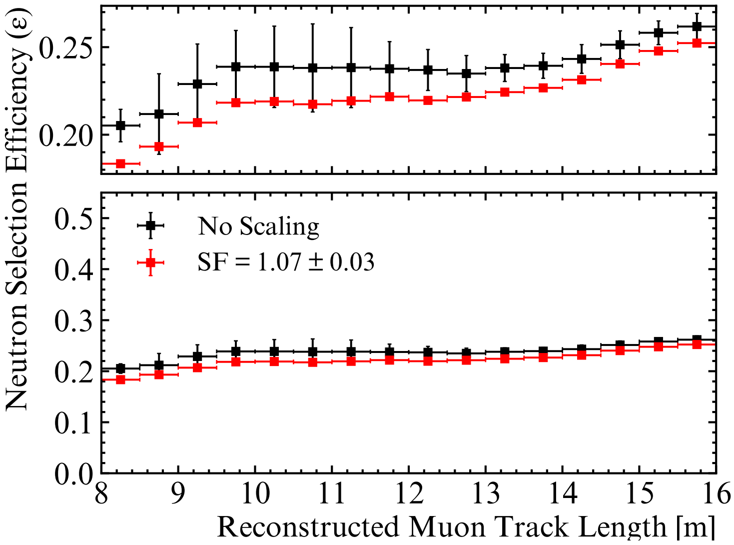

Figure 7.11: The neutron selection efficiency against the reconstructed muon track length. The plot compares efficiencies using the scale factor (SF) (red), applied to the distance from muon that the data prefers, to the efficiencies with no scale factor (black). The top panel is a zoom of the lower panel.

Number of PMT Hits from Neutron Capture

The above method was repeated for the inTimeHits100. Figure 7.8a, from section 7.5.2, shows the comparison between data and simulation for the inTimeHits100 of neutron capture events. As the MC events used in this comparison were generated isotropically, the events have been weighted by radius according to the radial distribution of the cosmogenic neutron events in data.

The method by which the inTimeHits100 is calculated means that there is an inherent distribution within integer bins, as shown in figure 7.12. This is due to the signal's trigger waveform being smoothed, causing it to have a non-integer height. In order to apply a scale factor to the distribution uniformly, the inTimeHits100 is forced to be distributed uniformly within each integer bin before applying the scale factor. Similar to the previous section, the scale factor is applied by multiplying the inTimeHits100 of each event by the scale factor, then pass through the neutron selection criteria.

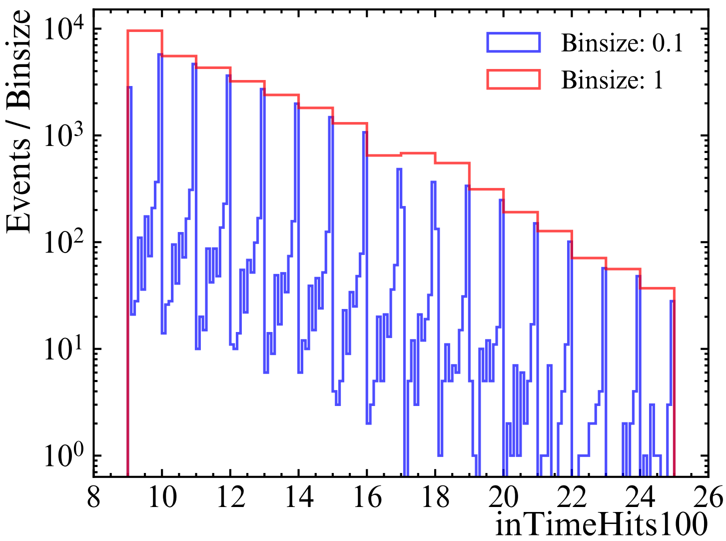

Figure 7.12: The number of inTimeHits100 within bins of width 0.1 and 1 to demonstrate the distribution within integer bins.

The result of applying the scaling method to the uniformly distributed events is shown in figure 7.13. This plot has been fitted with a quadratic. The minimum, with a 1σ error interval, was found to be: 0.95 ± 0.01. The effect this has on the data-MC comparison is shown in figure 7.14.

To increase the statistics used in this investigation, the above method was repeated using data taken for the Am-Be calibration. As described in section 4.2.5, the Am-Be calibration source was used as a source of neutrons during the water phase. For a large fraction of the neutrons emitted by the Am-Be source, a 4.4 MeV gamma is also emitted. The time it takes for the neutron to capture means that there is a delay between the prompt 4.4 MeV gamma and the delayed neutron capture. For the analysis of Am-Be data, the coincidence tag, given in table 7.1, was applied to data during processing, where N_p is the cleaned nhits of the prompt candidate, N_d is the cleaned nhits of the delayed candidate, and ΔT is the time between the delayed and prompt events. From this point, only the delayed candidates (the neutrons) will be considered.

During the Am-Be calibration, the source was moved to different positions within

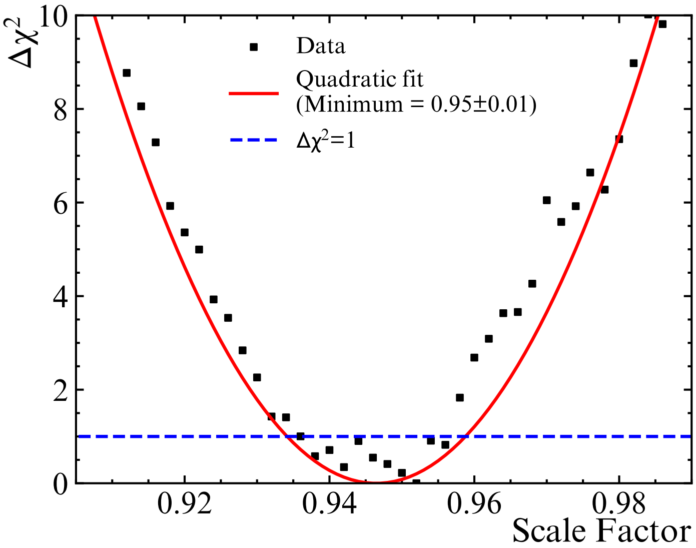

Figure 7.13: How the χ^2 between data and simulation changes when different scale factors are applied to the uniformly distributed inTimeHits100 of the simulated neutron captures. The points (black) have been fit with a quadratic (red) which minimises at 0.95 ± 0.01.

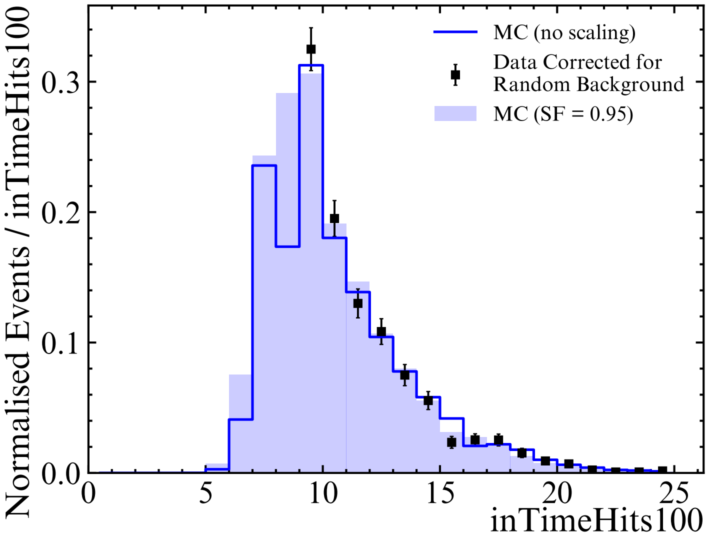

Figure 7.14: A comparison between the cosmogenic neutron data (black), the MC (blue, empty), and the MC with a scale factor of 0.95 applied (blue, filled) for the inTimeHits100. The MC is scaled by multiplying each simulated neutron's inTimeHits100 by the scale factor, then passing the neutron selection criteria over them.

the detector. These different positions included some within the AV (internal) and some outside the AV (external). These positions are shown in figure 4.3. Simulations of neutrons generated at the different Am-Be deployment positions were also

Parameter	Select if
fitValid	True
ΔT	$\leq 1000\,\mu$s
N_p	≥ 17
N_d	≥ 7

Table 7.1: The selection criteria that are applied to the Am-Be data to select the prompt (4.4 MeV gamma) and delayed (2.2 MeV gamma) candidates, where N_p is the nhits cleaned of the prompt candidate, N_d is the nhits cleaned of the delayed candidate, and ΔT is the time between the delayed and prompt events.

produced.

After selecting the data, the next step is to assess the number of background events, and their contribution to the inTimeHits100. Figure 7.15 shows the time between the delayed and prompt events in the Am-Be data. This has been fitted with equation 5.2 using a fixed decay time, taken as the neutron capture time measured in the Am-Be calibration: $t_n = 202.53^{+0.87}_{-0.76}\,\mu$s [42]. Fixing the decay time yields a flat background component of $b = 2754$, which corresponds to $137,693$ events (out of a total of $497,098$ events). This flat background comes from events that have been accidentally tagged as delayed candidates, known as accidentals, which are a background. In order to find the inTimeHits100 distribution of these accidentals, the coincidence tag was run over data when there was no Am-Be source in the detector. Two runs were selected for this purpose: one before source deployment, and one after the source was removed. Accidental delayed events are uncorrelated with their prompt event. This means the distribution of times between the prompt and delayed events is expected to be flat, as observed in figure 7.16a. The inTimeHits100 distribution is given in figure 7.16b.

Figure 7.17 compares the inTimeHits100 for data and simulation, where the data has been corrected for the inTimeHits100 distribution of the accidental background using the ratio $137,694/497,098$. This plot compares the data and simulation after applying the selection condition of $9 \leq$ inTimeHits100 ≤ 25. The events in this comparison have been weighted by the radial distribution of the cosmogenic neutron events in data. This has been done to include any radial dependency of the

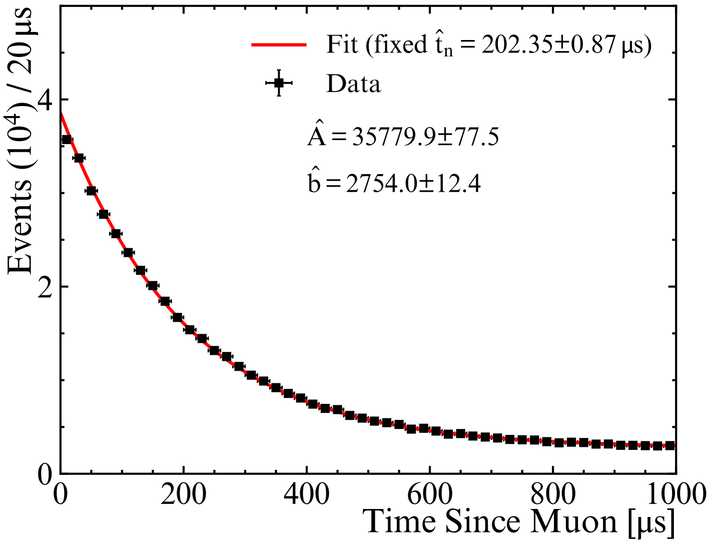

Figure 7.15: The time between the prompt and delayed events in the Am-Be data (black), fitted with equation 5.2 using the neutron capture time measured in the Am-Be calibration (red) [42].

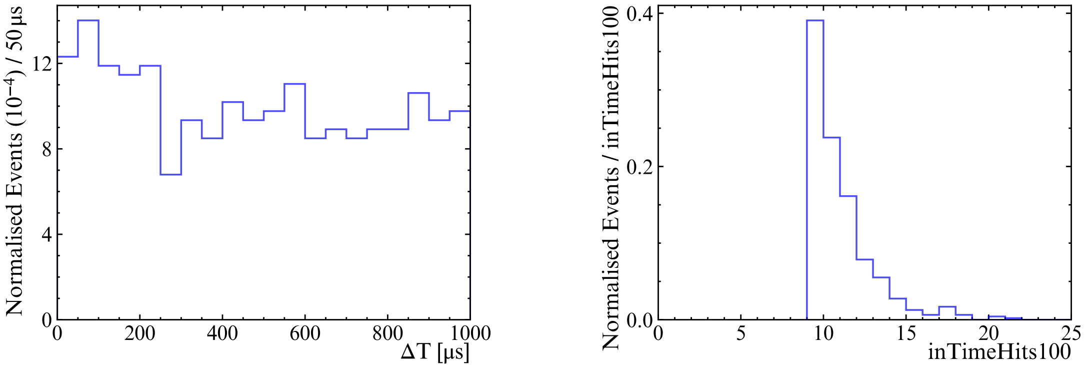

(a) The time between the prompt and delayed candidates after running the Am-Be event selection criteria over runs with no Am-Be source in the detector.

(b) The inTimeHits100 of the prompt out of window accidentals with a selection condition of $9 \leq$ inTimeHits100 ≤ 25 applied.

Figure 7.16: The time (left) and inTimeHits100 (right) distributions for the out of window accidentals selected from runs before and after the Am-Be source deployment.

inTimeHits100. A comparison with these data events will be used for the uniform scaling method, as outlined above.

Figure 7.18 shows the χ^2 between the inTimeHits100 of the Am-Be neutron candidates from data and the simulated neutron events after a scaling factor has been applied to the uniformly distributed inTimeHits100. This plot has been fitted

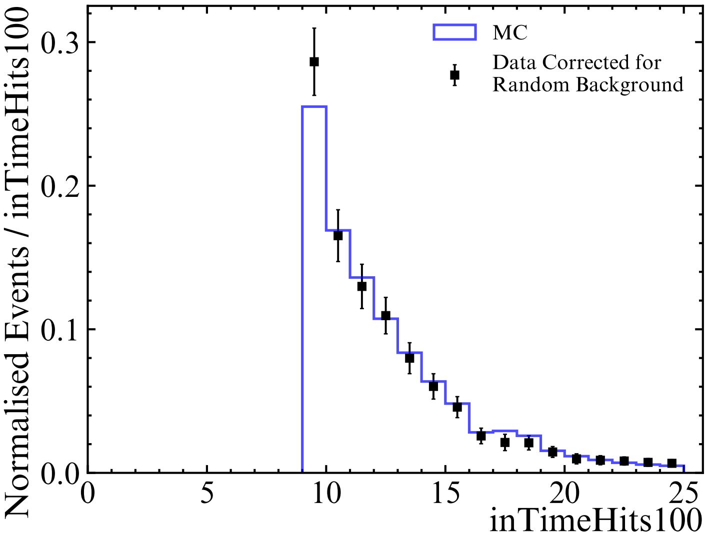

Figure 7.17: Comparison of the inTimeHits100 between the MC (blue) and data (black) for the delayed Am-Be neutron candidates, after correcting for the accidental background contribution and applying the neutron selection condition of $9 \leq \text{inTimeHits100} \leq 25$.

with a quadratic, and the minimum, with a 1σ error interval, was found to be: 0.99 ± 0.02. The scaled distribution is shown in figure 7.19, where it is compared to the non-scaled distribution and the data.

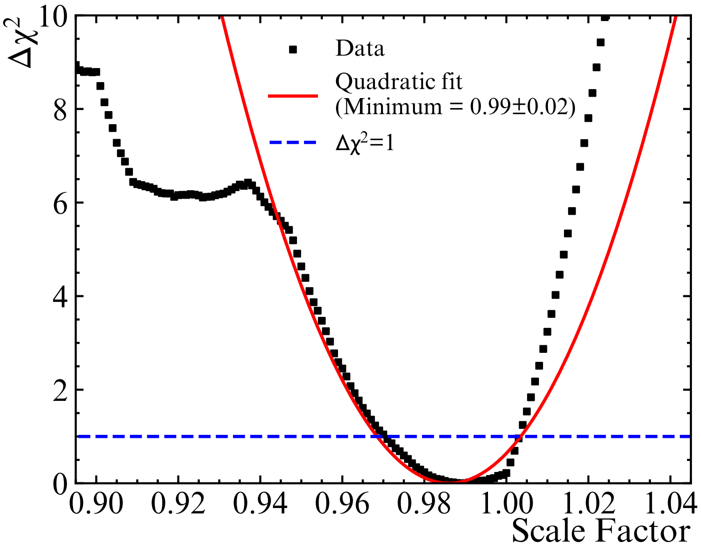

Figure 7.18: How the χ^2 between data and simulation changes when different scale factors are applied to the uniformly distributed inTimeHits100 of the simulated Am-Be neutrons (black). The points have been fitted with a quadratic (red) which minimises at 0.99 ± 0.02.

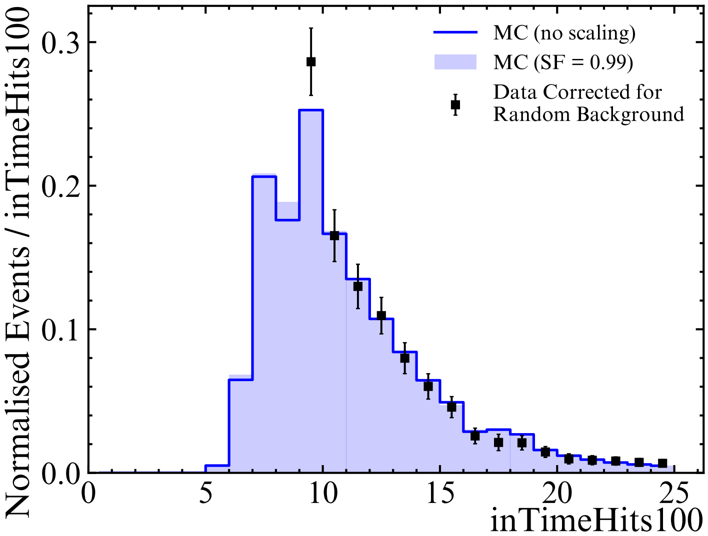

Figure 7.19: A comparison between the Am-Be neutron data (black), the MC (blue, empty), and the MC with the scale factor of 0.99 applied (blue, filled) for the inTimeHits100. The MC is scaled by multiplying each simulated neutron's inTimeHits100 by the scale factor, then passing the neutron selection criteria over them.

These two investigations have yielded two preferred scaling factors for the inTimeHits100: 0.95 ± 0.01 from the cosmogenic neutrons and 0.99 ± 0.02 from the Am-Be neutrons, which will be named the Cosmogenic and Am-Be corrections, respectively. Now the efficiencies which correspond to these scale factors must been found. Since the simulations used to calculate the neutron selection efficiency were performed with the photon tracking turned off, finding the effect on the efficiency from scaling the inTimeHits100 is not as simple as applying a scale factor and re-doing the selection and calculation. Instead,

$$\varepsilon' = \varepsilon \frac{N_{after}}{N_{before}} \tag{7.12}$$

can be used to find the neutron selection efficiency after scaling the inTimeHits100 ε'. The ratio $\frac{N_{after}}{N_{before}}$ is found using the MC-generated 2.2 MeV gammas, used in section 7.3, where N_{before} is the number of events that pass the inTimeHits100 selection condition before applying a scale factor to the inTimeHits100, and N_{after} is the number of events that pass the inTimeHits100 selection condition after applying a scale factor to the inTimeHits100. The relation between the ratio $\frac{N_{after}}{N_{before}}$ and the scale factor applied is shown in figure 7.20.

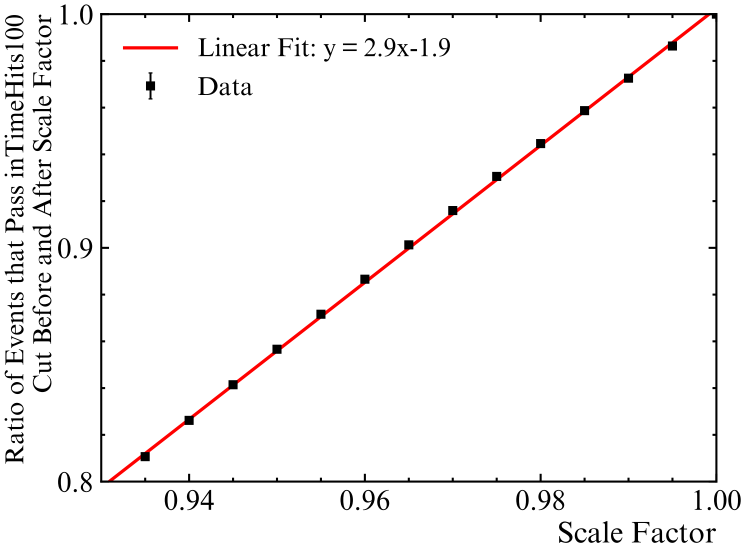

Figure 7.20: How the scale factor applied to the inTimeHits100 affects the number of events which pass the inTimeHits100 selection condition. This has been fitted with the equation: $y = 2.9x - 1.9$ (red).

Using the scale factors obtained given by the Am-Be correction and Cosmogenic correction, figure 7.20 can be extrapolated to give the corresponding ratio $\frac{N_{after}}{N_{before}}$. This is used in equation 7.12 to find the associated neutron selection efficiencies after applying the scale factors to the inTimeHits100. The final neutron selection efficiencies from the two corrections are shown in figure 7.21. Both the 1σ error found for the scale factors (red and blue error bars) and the error due to the spread in the efficiencies (black error bars) have been included. As it is much greater than the error from the uncertainty in the scale factor, the errors from the spread in efficiencies across each bin will be taken as the final uncertainties in the neutron selection efficiency within each bin. The neutron selection efficiency after applying the Am-Be correction agrees with the efficiency with no scaling applied. However, the neutron selection efficiency after applying the Cosmogenic correction does not agree with the other results. The effect this has on the final neutron yield will be presented in the next section.

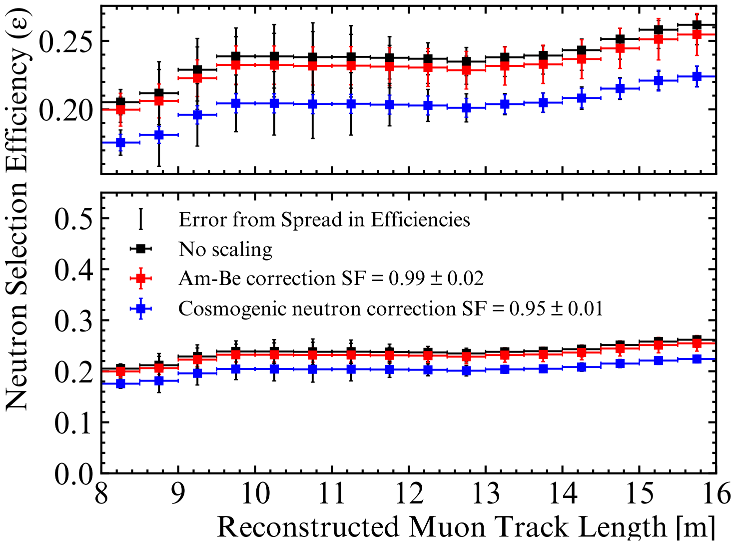

Figure 7.21: How scaling the inTimeHits100 affects the neutron selection efficiency. Black shows the efficiency when no scaling is applied, red shows the efficiency when the Am-Be correction is applied, and blue shows the efficiency when the Cosmogenic correction is applied. Black error bars represent the error due to the spread in efficiencies, and the red and blue error bars represent the error in the scale factor.

Summary of Corrections to Neutron Selection Efficiency

This section has provided the analysis for constraining the uncertainty in the performance of neutrons in simulation. The analysis has been performed using a data-MC comparison, where the MC has been scaled by various scale factors, and the preferred scale factor has been selected. This method was applied to the distance travelled by neutrons, resulting in the Distance correction; the inTimeHits100 of the neutrons produced by cosmic muons, resulting in the Cosmogenic correction; and the inTimeHits100 of the neutrons produced by the Am-Be source, resulting in the Am-Be correction. The neutron selection efficiencies, for each muon track length bin, before and after applying each correction are shown in table 7.2. The application of these corrections will be discussed in chapter 8.

Muon Track Length Bin [m]	Neutron Selection Efficiency			
	No correction	Distance correction	Am-Be Hits correction	Cosmogenic Hits correction
8.0–8.5	0.205 ± 0.009	0.183 ± 0.012	0.200 ± 0.012	0.176 ± 0.006
8.5–9.0	0.212 ± 0.023	0.193 ± 0.020	0.206 ± 0.012	0.181 ± 0.006
9.0–9.5	0.229 ± 0.023	0.207 ± 0.020	0.223 ± 0.013	0.196 ± 0.007
9.5–10.0	0.239 ± 0.021	0.218 ± 0.016	0.232 ± 0.014	0.204 ± 0.007
10.0–10.5	0.239 ± 0.023	0.219 ± 0.020	0.232 ± 0.014	0.204 ± 0.007
10.5–11.0	0.238 ± 0.025	0.217 ± 0.025	0.232 ± 0.014	0.204 ± 0.007
11.0–11.5	0.238 ± 0.023	0.219 ± 0.023	0.232 ± 0.014	0.204 ± 0.007
11.5–12.0	0.238 ± 0.016	0.222 ± 0.013	0.231 ± 0.014	0.203 ± 0.007
12.0–12.5	0.237 ± 0.012	0.220 ± 0.012	0.231 ± 0.014	0.203 ± 0.007
12.5–13.0	0.235 ± 0.010	0.222 ± 0.010	0.229 ± 0.014	0.201 ± 0.007
13.0–13.5	0.238 ± 0.008	0.224 ± 0.009	0.232 ± 0.014	0.204 ± 0.007
13.5–14.0	0.239 ± 0.007	0.227 ± 0.008	0.233 ± 0.014	0.205 ± 0.007
14.0–14.5	0.243 ± 0.008	0.231 ± 0.009	0.237 ± 0.014	0.208 ± 0.007
14.5–15.0	0.251 ± 0.008	0.240 ± 0.009	0.245 ± 0.015	0.215 ± 0.007
15.0–15.5	0.258 ± 0.007	0.248 ± 0.008	0.251 ± 0.015	0.221 ± 0.008
15.5–16.0	0.262 ± 0.008	0.252 ± 0.008	0.255 ± 0.015	0.224 ± 0.008

Table 7.2: The neutron selection efficiencies for each muon tack length bin, before and after applying the various corrections, as described in the text.

7.6 Chapter Summary

This chapter's focus has been on evaluating the neutron selection efficiency. This is what accounts for any missed neutrons, after applying the neutron selection criteria. The method for calculating this was outlined in section 7.1. This method uses muon simulations to calculate an efficiency per muon, and accounts for any effects due to muon misreconstruction. This involves smearing the track of each muon in data within the reconstruction uncertainty. Further details of this are in section 7.2.

To save on computational power, the muon simulations used for calculating the neutron selection efficiency are run with no photon tracking. Although this makes the simulations run faster, this is problematic due to the neutron reconstruction method requiring the photons produced by the event. This is avoided using reconstruction PDFs that are sampled based on the true position of the neutrons produced in the muon simulations. More details on this are found in section 7.3.

The results of running the neutron selection efficiency calculation method are presented in section 7.4. The method was run over a sample of 10% of the cosmic muons from data. These efficiencies were then binned according to the reconstructed track length of the muons. Each muon in the full data set will then be given an efficiency based on the bin their reconstructed track length falls within.

Finally, in section 7.5, the different contributions to the systematic uncertainty in the efficiency were evaluated. The first is the spread in efficiencies due to the muon smearing, that accounts for the muon misreconstruction. This is found per bin by fitting the residuals from the weighted mean for each bin with a Gaussian, and using the standard deviation of that fit. The uncertainty is then assigned to each muon along with its efficiency.

The other contribution to the systematic uncertainty that was considered was due to how the neutrons are modelled in simulation. The first way this could affect the neutron selection efficiency is if the neutrons travel further in simulation before being captured than they actually do. This was constrained using a comparison between data and simulation for the distance between muon and neutron capture. It was found that the data preferred a slightly longer distance travelled by the neutrons, resulting in a decrease in the neutron selection efficiency, named the Distance correction. The second way in which the neutron modelling could affect the efficiency is from the number of PMT hits produced in the simulations. This was constrained using a similar method of comparing the cosmogenic neutron data with the simulation. However, the method was repeated using data taken in water with the Am-Be calibration source, because of the greater number of events in this data set. This produced two corrections to the efficiency that are named as the Cosmogenic correction and the Am-Be correction, based on which data set used. The effect of this on the yield will be investigated in the next chapter.

Chapter 8

Results

Neutron spallation is caused by the electromagnetic showers which accompany the muon as it travels. Due to this showering effect, if one neutron is produced it is likely that more will be produced making the process non-Poissonian. Although cosmogenic neutron production is not necessarily a Poisson process, the measurements of the neutron yield by different experiments, shown in figure 3.9, have all assumed it is a Poisson process. So that we can compare this SNO+ result for the yield to the results of other experiments, yield has been computed assuming Poisson neutron production.

For Poisson neutron production, the probability that we observe N^i_{obs} neutrons for the i^{th} muon, given an expected number of neutrons λ^i, is given by

$$P(N^i_{\mathrm{obs}}|\lambda^i) = \frac{(\lambda^i)^{N^i_{\mathrm{obs}}}}{N^i_{\mathrm{obs}}!} e^{-\lambda^i}. \tag{8.1}$$

From equations 3.10 and 3.11, the parameter λ^i can be replaced with $\lambda^i = Y^\mu_n \varepsilon^i L^i \rho + B^i_R$, where the background due to other spallation products (B^i_C) has been neglected. Over a total of N_μ muons in the data set, the likelihood function is

$$L(Y^\mu_n) = \prod_{i=1}^{N_\mu} \frac{(Y^\mu_n \varepsilon^i L^i \rho + B^i_R)^{N^i_{\mathrm{obs}}}}{N^i_{\mathrm{obs}}!} e^{-Y^\mu_n \varepsilon^i L^i \rho - B^i_R}, \tag{8.2}$$

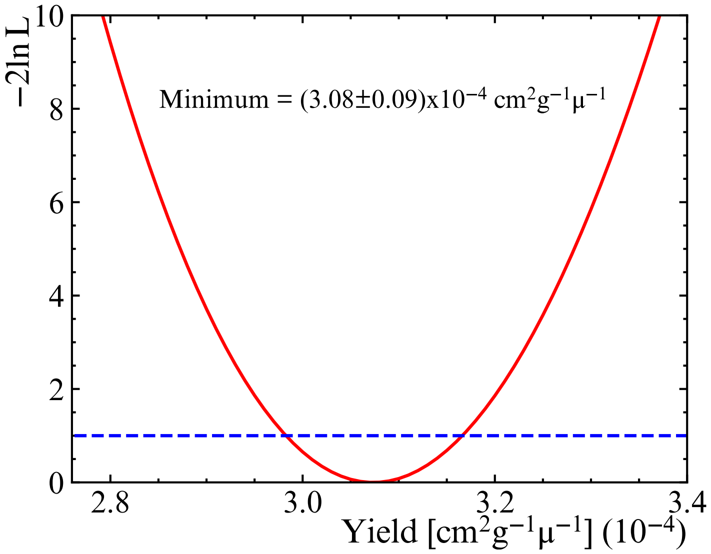

Figure 8.1: Estimation of the yield using the maximum likelihood method.

The log-likelihood is then given by

$$\mathcal{L}(Y) = \sum_{i=1}^{N_\mu} \left[-Y_n^\mu \varepsilon^i L^i \rho - B_R^i + N_{\text{obs}}^i \ln\left(Y_n^\mu \varepsilon^i L^i \rho + B_R^i \right) - \ln\left(N_{\text{obs}}^i ! \right) \right] . \tag{8.3}$$

Profiling this function with respect to Y_n^μ will give the best estimate for the yield.

For a range of values for Y_n^μ, the negative log-likelihood is computed and the minimum is found. Before considering any systematic uncertainty, figure 8.1 shows $-2\mathcal{L}(Y_n^\mu)$, the minimum of which corresponds to a final yield of $Y_n^\mu = (3.08 \pm 0.09) \times 10^{-4}\,\text{cm}^2\text{g}^{-1}\mu^{-1}$. The 1σ error corresponds to the points of intersection with $-2\mathcal{L}(Y_n^\mu) = 1$, and is purely statistical at this stage.

The next step is to include the systematic uncertainties from the neutron selection efficiency ε^μ, the reconstructed muon track length L^μ, and the number of random backgrounds B_R^μ. For each quantity with a systematic uncertainty, a penalty term is added to the likelihood. These penalty terms are Gaussians centred about their measured value so that the log-likelihood function becomes

$$\mathcal{L}(Y_n^\mu, \varepsilon^\mu, L^\mu) = \mathcal{L}(Y_n^\mu) + \frac{1}{2}\left(\frac{\varepsilon^\mu - \bar{\varepsilon}^\mu}{\sigma_\varepsilon^\mu} \right)^2 + \frac{1}{2}\left(\frac{L^\mu - \bar{L}^\mu}{\sigma_L^\mu} \right)^2 + \frac{1}{2}\left(\frac{B_R^\mu - \bar{B}_R^\mu}{\sigma_{B_R}^\mu} \right)^2 , \tag{8.4}$$

where $\bar{\varepsilon}^\mu$, $\bar{L}^\mu$ and $\bar{B}_R^\mu$ are the measured values, and σ_ε^μ, σ_L^μ and $\sigma_{B_R}^\mu$ are the uncertainties for ε^μ, L^μ and B_R^μ, respectively. A set of "trial" values for the yield are generated. For each trial value, the negative log-likelihood is profiled over ε^μ, L^μ and B_R^μ to find the minimum, with each parameter constrained by their respective penalty terms. This results in a negative log-likelihood curve for the yield.

The random background uncertainty is data driven and has been calculated for each muon using equation 6.2.

The uncertainty in the reconstructed muon path length comes from the reconstruction uncertainty in the muon's direction and initial position. In order to include the correlation between the direction and position uncertainty, figure 7.1 has been sampled for a range of path lengths. For each muon in the full muon data set, $1,000$ sample path lengths were generated. The error is given as the average difference between the muon's reconstructed path length and the sampled path lengths. The error has been split into an "upper error" and a "lower error" depending on if the sampled path length was longer or shorter than the reconstructed path length, respectively. These errors have been fitted against the reconstructed path length, as shown in figure 8.2. These fits will be extrapolated to give an upper and lower uncertainty in the path length for each muon.

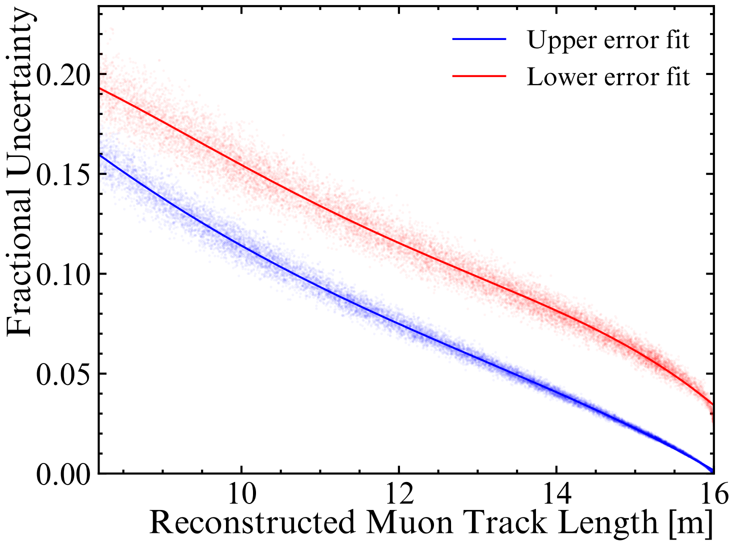

Figure 8.2: The fractional uncertainty as a function of track length. The points were made by sampling figure 7.1 $1,000$ times, and finding the average difference between the sampled path length and the original path length.

A more detailed review of the uncertainty in the neutron selection efficiency was presented in section 7.5. It was found from scaling the distance travelled by the neutrons and the inTimeHits100 that corrections should be applied to the efficiency. Three corrections were found: the Distance correction, the Am-Be correction, and the Cosmogenic correction.

The above method for calculating the likelihood with the penalty terms was applied using neutron selection efficiencies with: no correction, a combination of the Distance correction and the Am-Be correction, and the Cosmogenic correction. The results are shown in figure 8.3. From the black and green plots, it is shown that the systematic uncertainty on the yield, due to the uncertainties in ε^μ, L^μ and B_R^μ, has no effect on the width of the curve. This suggests that the statistical uncertainty dominates over the systematic uncertainty. However, the blue and the red plots show that the different corrections applied to the inTimeHits100 cause the yield to shift, with the maximum shift being around 17%.

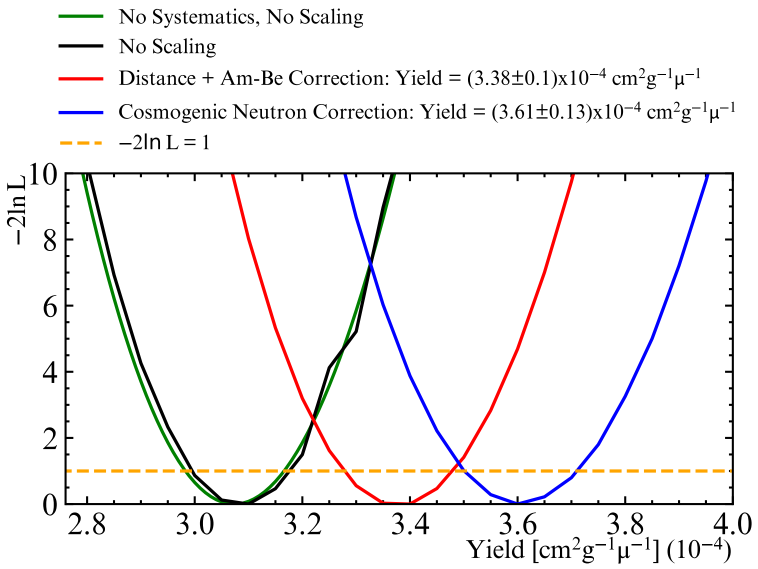

Figure 8.3: The cosmogenic neutron yield calculated using efficiencies with no scaling, and efficiencies that have been scaled using the Am-Be correction and the cosmogenic neutron correction.

Figure 8.4 shows this result for the neutron yield in comparison to other experimental results. For the SNO+ result on this plot, a conservative value of $Y_n^\mu = (3.38^{+0.23}_{-0.30}) \times 10^{-4}\,\mathrm{cm}^2\mathrm{g}^{-1}\mu^{-1}$ has been plotted. This is equal to the yield given by the Distance and Am-Be correction, with the upper and lower errors corresponding to the yields with the Cosmogenic correction and no correction, respectively. The final uncertainty in this result includes the 3% statistical uncertainty. Also included in figure 8.4 is the GEANT4 prediction for the neutron yield in water at SNO+: $Y_n^\mu = (2.130 \pm 0.001(\text{stat})) \times 10^{-4}\,\text{cm}^2\text{g}^{-1}\mu^{-1}$. This was calculated from simulating each muon from the data set and applying equation 3.10, with N_n^μ corresponding to the number neutrons produced in water, in the simulation.

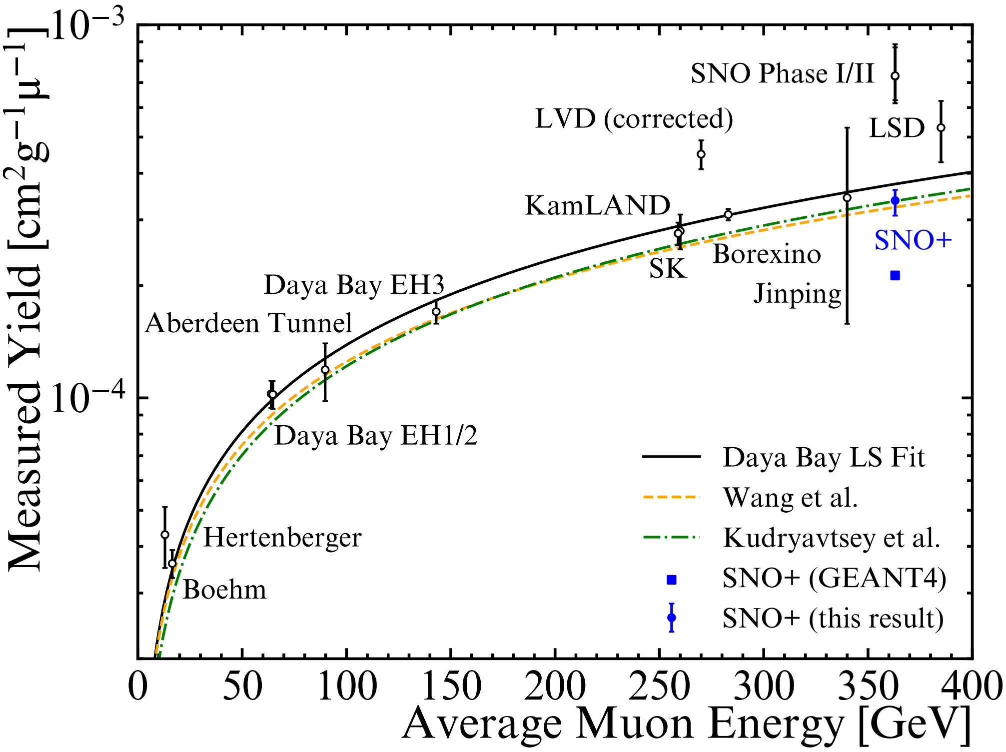

Figure 8.4: The neutron yield measured in this analysis (blue, round) and the GEANT4 predicted yield (blue, square) compared with measurements made by other experiments: Hertenberger [46], Boehm [47], Daya Bay [48], Aberdeen Tunnel [49], SK [50], KamLAND [51], LVD [52], Borexino [53], Jingping [54], SNO [55], LSD [56], in order of average muon energy. The solid line is a fit made for liquid scintillator based measurements by Daya Bay [48]. The dashed lines are FLUKA-based liquid scintillator predictions [40][57].

This is the final result of this analysis on measuring the cosmogenic neutron yield in water at SNO+. In chapter 9, this result will be discussed in the context of the previous results, with an outlook to a possible future measurement by SNO+.

Chapter 9

Conclusions

The neutrons produced by cosmic muons can pose as a background to underground experiments performing low-energy physics searches. The number of neutrons produced by a cosmic muon depends on the energy of the muon, and the medium it is moving through. Many underground experiments have made measurements of the cosmic muon-induced neutron multiplicity, using different detection media, across a wide range of cosmic muon energies. SNO+ is a multi-purpose neutrino experiment, located around 2 km underground, using the detector infrastructure inherited from the SNO experiment. SNO made the cosmogenic neutron multiplicity measurement using heavy water. The water and scintillator phases of SNO+ provides the opportunity to make the measurement using the same cosmic muon flux, using both water and scintillator. This thesis has outlined the analysis for measuring the cosmogenic neutron multiplicity in water at SNO+, in which the detection signal for neutrons is the 2.2 MeV gamma produced after neutron capture on hydrogen.

A total of 321 days of water phase data have been analysed. The muon and neutron selection criteria were designed to select a highly pure data set. After applying the muon and neutron selection criteria, $13,694$ muons and $1,208$ neutrons remained. This corresponded to an average muon rate of $1.72\,\mu\text{hour}^{-1}$. Fitting the neutron capture time, measured using the Am-Be calibration source, to the selected cosmogenic neutrons appeared to show good agreement, validating the purity of the sample.

There are two contributions to the background. The first is the other spallation products produced by the muon, which mimic the neutron capture signal. The study of this background found a number of 8472.32×10^{-10} expected events per muon, and therefore is considered to be negligible. The second contribution is due to the random background events that occur in coincidence with a muon. In total, we predict 150 ± 2 random backgrounds in coincidence with a muon.

As the neutron capture signal generates so few PMT hits, neutrons can be easily missed in selection. This means that it is very important to find the neutron selection efficiency which accounts for the missed neutrons. The neutron selection efficiencies have been calculated for $\sim 10\%$ of the full muon data set which results in a collection of efficiencies that can be binned according to the muon path length. These binned efficiencies are then assigned to the entire muon data set based on their path lengths. Each binned efficiency has an error from the spread in efficiencies per bin. This is due to muon reconstruction effects. Other systematic errors on the efficiency that have been considered include the mismodelling of neutron captures in the simulations that were used to calculate the efficiency. These have been constrained using a data-MC comparison.

The final result for the cosmogenic neutron yield is $Y_n^\mu = (3.38^{+0.23}_{-0.30}) \times 10^{-4}\,\text{cm}^2\text{g}^{-1}\mu^{-1}$, which has been presented in comparison to results from other experiments. The Geant4 predicted neutron yield in water at SNO+ is $Y_n^\mu = (2.130 \pm 0.001(\text{stat})) \times 10^{-4}\,\text{cm}^2\text{g}^{-1}\mu^{-1}$. This shows a $\sim 30\%$ deficit when compared to the measured yield. Similar deficiencies in the Geant4 prediction were observed by Daya Bay [48], and a study comparing the muon-induced neutron production models in FLUKA and Geant4 [45]. As figure 5.4a showed, in section 5.4, the biggest contributor to the excess in neutron events in data comes from cosmic muons that produce single neutron followers.

Comparing the SNO+ measurement of $Y_n^\mu = (3.38^{+0.23}_{-0.30}) \times 10^{-4}\,\text{cm}^2\text{g}^{-1}\mu^{-1}$ to the SNO result of $Y_n^\mu = (7.28 \pm 0.09(\text{stat})^{+0.23}_{-0.30}(\text{syst}) \times 10^{-4}\,\text{cm}^2\text{g}^{-1}\mu^{-1}$, for which the same muon fluxes were present, switching from heavy water to UPW shows a decrease in the neutron production. Only the oxygen, within water molecules, have neutrons available to release in cosmic muon-induced interactions. Whereas in heavy water, the two deuterium isotopes each have a neutron that may also be liberated by a muon. The decrease in the number of nuclei available to emit neutrons in muon interactions explains the decrease in neutron yield in water, compared with heavy water.

Although this result does not agree with the global liquid scintillator fit, produced by Daya Bay [48], this result does agree with the FLUKA-based liquid scintillator prediction. This reiterates the observation of SK's result in light water agreeing with KamLAND's result in scintillator, for the same muon flux [50]. Repeating this water measurement using the scintillator data of SNO+ will allow for an interesting comparison that could support this further. This comparison would contribute to the understanding of how atomic composition affects the muon-induced neutron yield. Due to the higher light yield of scintillator, the ability to detect neutrons will be greater, resulting in a higher neutron selection efficiency. However, this increase in light yield from water also means that muons will produce a much larger number of photons. This will lead to longer simulations, and difficulties in reconstructing muon tracks. The tools developed by the author for the water measurement, as discussed in this thesis, lay the groundwork for future SNO+ cosmogenic neutron yield measurements.

Appendix A

Run Selection

The conditions of a run, such as the number of online PMTs or the run duration, are stored in run tables. These tables are read in by the run selection code and are compared with a table of run criteria. For each entry in the run criteria table there is a threshold value. The values in the run table are compared to their associated threshold values in the run criteria table. If a value fails a criterion, then the run will be failed, and not passed over to processing.

During the scintillator phase, the initial run selection criteria were designed to select only the highest quality of runs that would be suitable for analysis. These runs were named “Scintillator Gold” runs. Among other criteria, these gold runs are required to be at least 30 minutes long, and have all 19 PMT crates on. The SNO+ detector has around 9400 PMTs, with one crate powering up toe 500 PMTs.

The detector may not always be in a perfect state, and from time to time runs with crates off. Instead of throwing these runs away, it was decided that these runs could be useful for analyses such as background rate measurements. For this purpose, the author designed two new sets of criteria: “Scintillator Silver” and “Scintillator Bronze”. As with the gold runs, silver runs must be at least 30 minutes long, but they can have a maximum of one PMT crate off. The bronze criteria allows runs to be at least 15 minutes in duration, with a maximum of two crates off.

Figure A.1 shows how the number of days that pass each criteria changes with time, compared with the total physics time, during the period from May 2022 to

February 2023. Over a total physics time of 239.5 days, the silver criteria results in 25.7 days more of data, compared with the gold criteria. This is an increase of 17.0%. The bronze criteria gains 54.3 days on top of the gold criteria, which is a gain of 36.0%. This new criteria has been added to the run selection checks, and silver and bronze lists are now automatically generated.

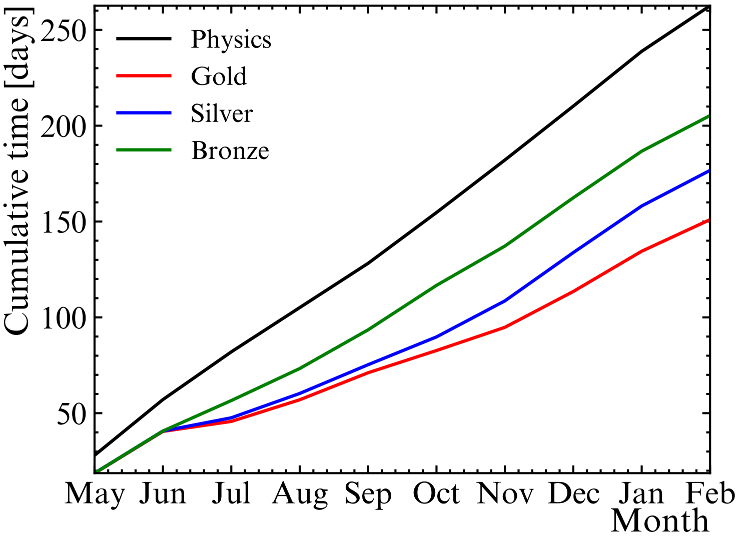

Figure A.1: The cumulative number of days of physics, gold, silver and bronze time using data from May 2022 to February 2023.

Appendix B

Telluric Acid Purification Plant

The tellurium begins its journey as TeA, which has been stored underground in SNOLAB. As a consequence of the time stored underground, the impurities due to cosmic muon activation have naturally reduced over time. However, before being added to the detector, the TeA must undergo further purification. The purpose of the purification process is to reduce the levels of radioactive backgrounds in the tellurium. This is completed in the TeA purification plant of SNOLAB.

TeA is a weak acid that undergoes the following equilibrium state between the protonated (left) and deprotonated (right) form:

$$\mathrm{Te(OH)_6} \rightleftharpoons \mathrm{Te(OH)_5O^-} + \mathrm{H^+}. \tag{B.1}$$

In equation B.1, the left side of the equilibrium is insoluble in water, whereas the right side is soluble. The first step of the purification is to dissolve the protonated acid crystals in water, which is then heated. This step occurs in the dissolution tank (DT). The solution is then passed through a filter, to remove insoluble impurities, before being cooled. Nitric acid is added to reduce the pH of the solution and force the equilibrium state to shift to the left, so the TeA becomes insoluble and crystallises. The crystals are collected using filters leaving behind the soluble impurities in the leftover solution. The leftover solution, containing the impurities, is sent to the nitric waste tank (NWT), where it is safely stored until it can be removed from the lab. The TeA crystals are rinsed with a mixture of cold nitric acid and UPW, mixed and cooled in the nitric rinse tank (NRT). This purges any residual liquid from the crystals. The crystals are then flushed with air to draw out the remaining liquid, which is sent to the NWT. Hot UPW is added from the hot water tank (HWT), into which the TeA crystals dissolve. The dissolved crystals can then be transferred back, so that this process can be repeated.

At the end of the second filtration pass, the final solution is cooled and the TeA crystals will form. The supernatant liquid is pumped to the nitric waste tank, and the crystals are flushed dry. The crystals are then rinsed three times with cold UPW from the thermal rinse tank (TRT). This time the residual liquid is dumped into the supernatant storage tank (SST), where it can be recycled. The final product is dissolved in hot UPW and sent to the TeBD synthesis plant. More details on the TeA purification process can be found in [68].

At the TeBD synthesis plant, the now purified TeA is reacted with BD to produce TeBD. The TeA is first heated under a vacuum with distilled BD and the water is removed to produce TeBD which is soluble in LAB. The TeBD is then mixed at a $1 : 1$ ratio with liquid scintillator taken from the detector before being added back into the detector [30]. The loading method is described fully in [69].

The TeA plant vessels mentioned above (DT, NWT, NRT, HWT, TRT, SST) each play an important role in the purification process. For safety reasons during plant operations, it is extremely useful to know approximately how much each vessel contains. Without knowing this information, a vessel could be overfilled. For this purpose, sensors are used to either measure the weight of the vessel, or the liquid level within the vessel. The sensors are linked to a programme called Delta-V, which is used to process and read out the data. A vessel's weight is measured using load cells which are positioned underneath the vessel. A vessel's level is measured using ultrasonic level sensors, placed at the top of the vessel. The ultrasonic level sensors send ultrasonic pulses down towards the surface of the liquid. The sound waves bounce off the liquid's surface and the sensor records the time it takes for the pulse to return. Calibrations of the level sensors and load cells were performed, by the author, to investigate how reliable each vessel's sensor is. The proceeding sections will present the results from the calibration of each vessel. As the main goal here is to show the sensors follow the general expected trend, accuracy will not be important.

B.1 Dissolution Tank Calibration

The DT has load cells which measure the weight of the DT and its contents. To evaluate the accuracy of the load cells, the DT was filled with water, and then slowly emptied. The water in the DT can be removed through a valve-controlled line, underneath the vessel. This line was used to empty the water into buckets, which can be weighed using a scale. The weight of the bucket can then be compared to the change in weight shown by Delta-V. This was repeated three times, and the results are shown in figure B.1.

The precision of the scale is $\pm 0.05\,\mathrm{kg}$, which is associated to each measurement of the weight removed. While the precision of the Delta-V reading is $\pm 0.005\,\mathrm{kg}$, the error for the Delta-V measurements was chosen to be $\pm 1\,\mathrm{kg}$, due to fluctuations of the reading. This will be the same for each calibration.

Although not all the points in figure B.1 lie on the $x = y$ line, the conclusion was that Delta-V's reading of the DT's weight is accurate enough for its purpose.

B.2 Nitric Waste Tank Calibration

The NWT has an ultrasonic level sensor located as the top of the vessel, off-centre. The NWT was filled with water, and then emptied into buckets from a valve on the side of the vessel, near the bottom. Each bucket was weighed on the scale and the cumulative total water removed was calculated for each bucket. Once the water level dropped below the valve level, water was drained from a different valve at the very bottom of the vessel, so that as much water as possible could be removed. A total of $(1900 \pm 10)\,\mathrm{kg}$ of water was added to the NWT.

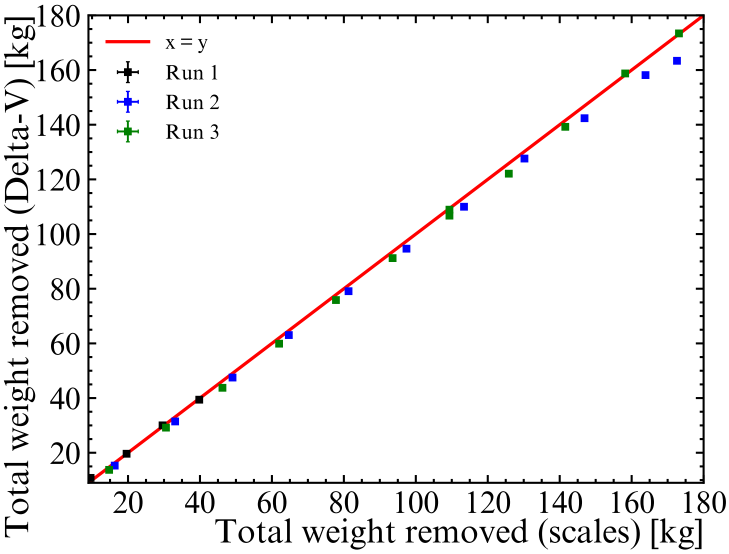

Figure B.1: The cumulative weight removed from the DT, measured by a scale, compared with that measured by Delta-V.

The liquid level, measured by the level sensors and shown in Delta-V, can be compared with the fraction of the total weight remaining in the NWT, calculated by measuring the total weight of the water removed. The results for repeating this method twice are shown in figure B.2. This procedure could only be carried out twice due to the amount of water involved in the filling of the NWT however, both repeats match well. It can be observed from the plot that the liquid level, measured by the level sensor, performs two separate downward shifts before jumping back up. This was observed at the same two points during each repeat. This confirms that the level sensor for the NWT is unreliable. As the purpose of the NWT is mostly to store waste supernatant, this is not considered to be a problem. The cause of these issues could be due to a combination of the ultrasonic level sensor being off-centre and the bottom of the NWT being conical-shaped. Further investigations were not required.

B.3 Hot Water Tank Calibration

The HWT has an ultrasonic level sensor at the top of the vessel. The HWT was filled with water and slowly emptied. The HWT does not have a valve to empty directly

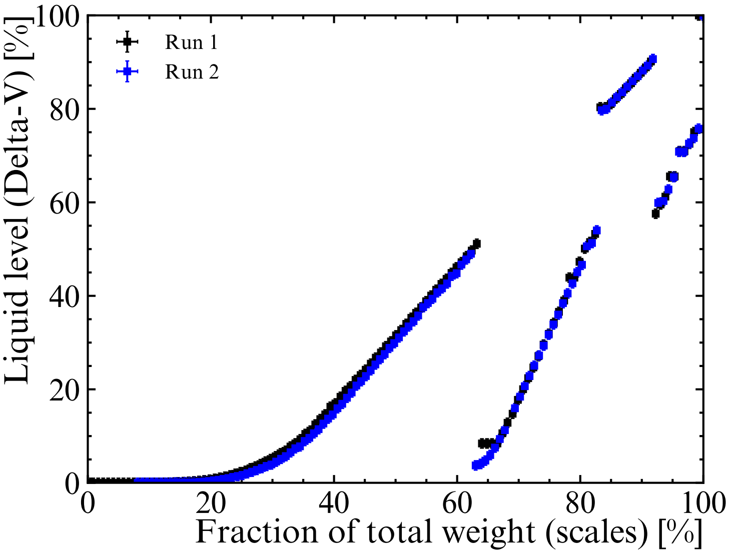

Figure B.2: The fraction of the total weight remaining in the NWT, measured by a scale, compared with the liquid level measured by Delta-V.

into a bucket. Instead the water was emptied into the DT, and the change in weight was measured by the DT's load cells. Figure B.3 shows the comparison between the liquid level in the HWT measured by the level sensor, and the cumulative weight of water removed, as a fraction of the total weight. The larger errors in the fraction of the total weight are due to the weight being measured using the DT's load cells, which have contributions due to fluctuations. The points follow the general trend that is expected, although they do not all align with the $x = y$ line. For the purposes of the HWT, this was considered to be a sufficient agreement.

B.4 Thermal Rinse Tank Calibration

The TRT has an ultrasonic level sensor to measure the liquid level in the vessel. Water can be extracted from the vessel directly into buckets. The weight of each bucket can be measured, and the liquid level can be recorded using Delta-V. Figure B.4 shows the comparison between the change in weight measured by the scales and the change in liquid level, as measured by Delta-V using the ultrasonic level sensor. The agreement between two measurements is acceptable for the purpose of the TRT.

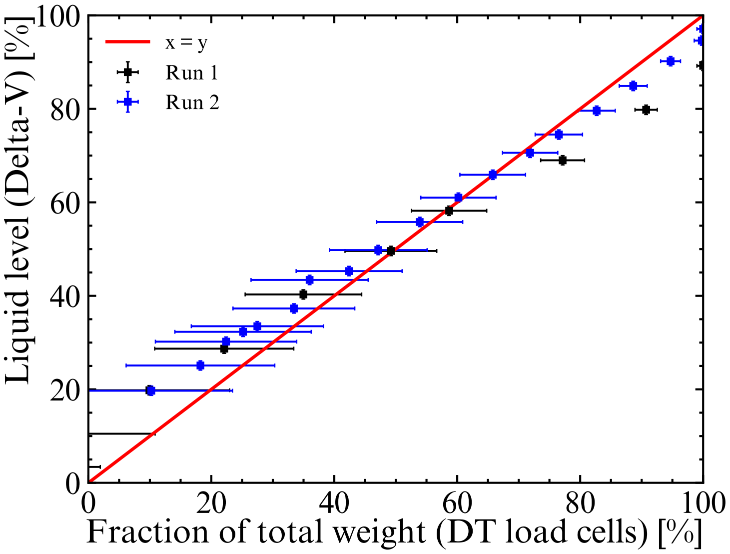

Figure B.3: The fraction of the total weight remaining in the HWT measured by Delta-V, using the load cells associated with the DT, compared with the liquid level measured by Delta-V.

B.5 Nitric Rinse Tank Calibration

The NRT was filled with water and then emptied via multiple buckets. After each extraction, the bucket was weighed using the scales, and the liquid level was recorded using Delta-V, which reads in the measurement from the ultrasonic level sensor. The results from this are shown in figure B.5. It can be seen in the first run there are three values that are outliers. This is not repeated in the second and third runs, so they are considered to be anomalies, possibly due to fluctuations in the Delta-V reading. Overall, the results agree within the allowed margin or error for the role of the level sensor in operations.

B.6 Supernatant Storage Tank Calibration

The SST has both load cells to measure the vessel's weight, and an ultrasonic level sensor to measure the level of the liquid in the vessel. The SST was filled with water, and the water was removed bucket-by-bucket. With each bucket removed, the weight and the level displayed on Delta-V, associated to the SST, was recorded.

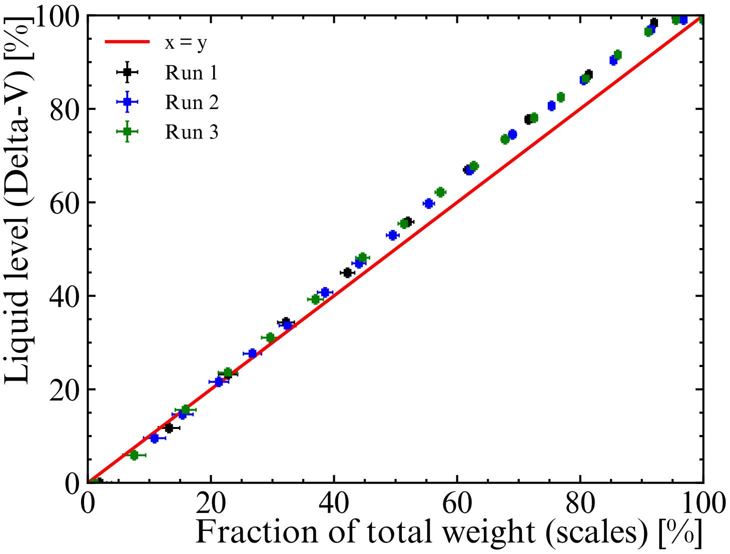

Figure B.4: The fraction of the total weight remaining in the TRT, measured by a scale, compared with the liquid level measured by Delta-V.

These quantities are compared to the weight of water removed, measured using the scales, as shown in figure B.6. Both load cells and level sensor follow the correct trend, and are considered to be reliable enough for plant operations. It was decided that a repeat measurement was unnecessary.

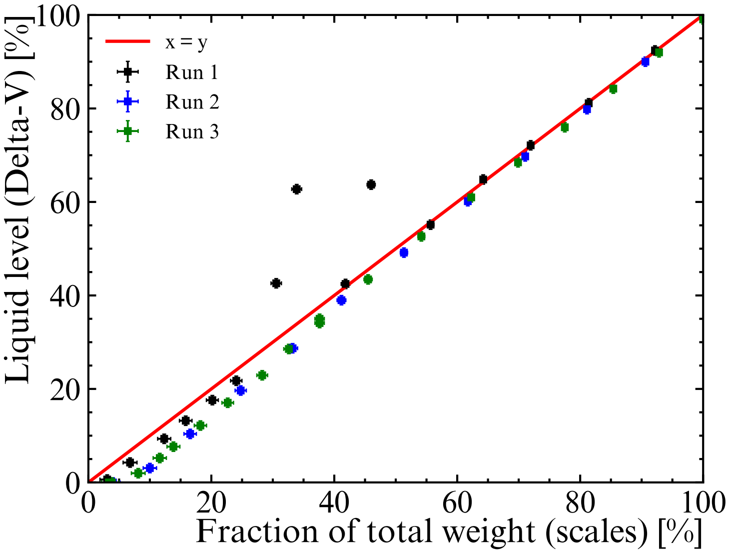

Figure B.5: The fraction of the total weight remaining in the NRT, measured by a scale, compared with the liquid level measured by Delta-V.

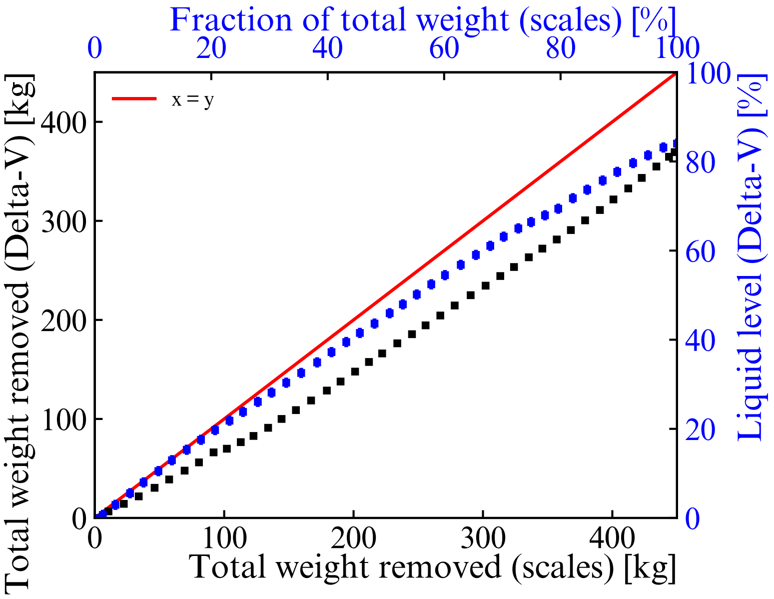

Figure B.6: In black is the cumulative weight removed from the SST, measured by a scale, compared with that measured by Delta-V. In blue is the fraction of the total weight remaining in the SST, measured by a scale, compared with the liquid level measured by Delta-V.

Bibliography

[1] Billy Liggins. “Cosmic muon-induced neutrons in the SNO+ water phase”. en. PhD thesis. Queen Mary University of London, Apr. 2020. URL: `https://qmro.qmul.ac.uk/xmlui/bitstream/handle/123456789/68614/Liggins_B_PhD_final_210420.pdf?sequence=1&isAllowed=y`.

[2] Wolfgang Pauli. *Dear radioactive ladies and gentlemen*. German. Dec. 1930. URL: `https://inspirehep.net/literature/45177`.

[3] Clyde L. Cowan Jr et al. “Detection of the Free Neutrino: a Confirmation”. In: *Science* 124.3212 (July 1956), pp. 103–104. DOI: `https://doi.org/10.1126/science.124.3212.103`.

[4] Raymond Davis, Don S. Harmer, and Kenneth C. Hoffman. “Search for Neutrinos from the Sun”. en. In: *Physical Review Letters* 20.21 (May 1968), pp. 1205–1209. ISSN: 0031-9007. DOI: `10.1103/PhysRevLett.20.1205`. URL: `https://link.aps.org/doi/10.1103/PhysRevLett.20.1205` (visited on 07/04/2025).

[5] John N. Bahcall. “Solar Neutrino Cross Sections and Nuclear Beta Decay”. en. In: *Physical Review* 135.1B (July 1964), B137–B146. ISSN: 0031-899X. DOI: `10.1103/PhysRev.135.B137`. URL: `https://link.aps.org/doi/10.1103/PhysRev.135.B137` (visited on 07/04/2025).

[6] R. Becker-Szendy et al. “Electron- and muon-neutrino content of the atmospheric flux”. en. In: *Physical Review D* 46.9 (Nov. 1992), pp. 3720–3724. ISSN: 0556-2821. DOI: `10.1103/PhysRevD.46.3720`. URL: `https://link.aps.org/doi/10.1103/PhysRevD.46.3720` (visited on 07/04/2025).

[7] Y. Fukuda et al. “Evidence for Oscillation of Atmospheric Neutrinos”. en. In: *Physical Review Letters* 81.8 (Aug. 1998), pp. 1562–1567. ISSN: 0031-9007, 1079-7114. DOI: `10.1103/PhysRevLett.81.1562`. URL: `https://link.aps.org/doi/10.1103/PhysRevLett.81.1562` (visited on 07/04/2025).

[8] Q. R. Ahmad et al. “Direct Evidence for Neutrino Flavor Transformation from Neutral-Current Interactions in the Sudbury Neutrino Observatory”. en. In: *Physical Review Letters* 89.1 (June 2002), p. 011301. ISSN: 0031-9007, 1079-7114. DOI: `10.1103/PhysRevLett.89.011301`. URL: `https://link.aps.org/doi/10.1103/PhysRevLett.89.011301` (visited on 07/04/2025).

[9] M.C. Gonzalez-Garcia and M. Yokoyama. “Neutrino Masses, Mixing, and Oscillations”. In: *Prog. Theor. Exp. Phys.* 8 (2022), p. 083C01. DOI: `10.1093/ptep/ptac097`. URL: `https://pdg.lbl.gov/2024/reviews/rpp2024-rev-neutrino-mixing.pdf`.

[10] M. Aker et al. *Direct neutrino-mass measurement based on 259 days of KATRIN data.* arXiv:2406.13516 [nucl-ex]. June 2024. DOI: `10.48550/arXiv.2406.13516`. URL: `http://arxiv.org/abs/2406.13516` (visited on 07/15/2025).

[11] Planck Collaboration et al. “*Planck*2018 results: VI. Cosmological parameters”. en. In: *Astronomy & Astrophysics* 641 (Sept. 2020). Publisher: EDP Sciences, A6. ISSN: 0004-6361, 1432-0746. DOI: `10.1051/0004-6361/201833910`. URL: `https://www.aanda.org/10.1051/0004-6361/201833910` (visited on 07/15/2025).

[12] Shadab Alam et al. “Completed SDSS-IV extended Baryon Oscillation Spectroscopic Survey: Cosmological implications from two decades of spectroscopic surveys at the Apache Point Observatory”. In: *Physical Review D* 103.8 (Apr. 2021). Publisher: American Physical Society, p. 083533. DOI: `10.1103/PhysRevD.103.083533`. URL: `https://link.aps.org/doi/10.1103/PhysRevD.103.083533` (visited on 07/15/2025).

[13] Ettore Majorana. “Teoria simmetrica dell’elettrone e del positrone”. In: *Il Nuovo Cimento (1924-1942)* 14.4 (Apr. 1937), pp. 171–184. ISSN: 1827-6121. DOI: `10.1007/BF02961314`. URL: `https://doi.org/10.1007/BF02961314`.

[14] Peter Minkowski. “$\mu \to e\gamma$ at a rate of one out of 10^9 muon decays?” In: *Physics Letters B* 67.4 (Apr. 1977), pp. 421–428. ISSN: 0370-2693. DOI: `10.1016/0370-2693(77)90435-X`. URL: `https://www.sciencedirect.com/science/article/pii/037026937790435X` (visited on 07/04/2025).

[15] M. Goeppert-Mayer. “Double Beta-Disintegration”. en. In: *Physical Review* 48.6 (Sept. 1935), pp. 512–516. ISSN: 0031-899X. DOI: `10.1103/PhysRev.48.512`. URL: `https://link.aps.org/doi/10.1103/PhysRev.48.512` (visited on 07/02/2025).

[16] Mark G. Inghram and John H. Reynolds. “Double Beta-Decay of Te 130”. en. In: *Physical Review* 78.6 (June 1950), pp. 822–823. ISSN: 0031-899X. DOI: `10.1103/PhysRev.78.822.2`. URL: `https://link.aps.org/doi/10.1103/PhysRev.78.822.2` (visited on 07/02/2025).

[17] Matteo Agostini et al. “Toward the discovery of matter creation with neutrinoless double-beta decay”. In: *Reviews of Modern Physics* 95.2 (May 2023). arXiv:2202.01787 [hep-ex], p. 025002. ISSN: 0034-6861, 1539-0756. DOI: `10.1103/RevModPhys.95.025002`. URL: `http://arxiv.org/abs/2202.01787` (visited on 07/02/2025).

[18] J. Kotila and F. Iachello. “Phase-space factors for double-β decay”. en. In: *Physical Review C* 85.3 (Mar. 2012), p. 034316. ISSN: 0556-2813, 1089-490X. DOI: `10.1103/PhysRevC.85.034316`. URL: `https://link.aps.org/doi/10.1103/PhysRevC.85.034316` (visited on 07/02/2025).

[19] Jonathan Engel and Javier Menéndez. “Status and Future of Nuclear Matrix Elements for Neutrinoless Double-Beta Decay: A Review”. In: *Reports on Progress in Physics* 80.4 (Apr. 2017). arXiv:1610.06548 [nucl-th], p. 046301.

ISSN: 0034-4885, 1361-6633. DOI: `10.1088/1361-6633/aa5bc5`. URL: `http://arxiv.org/abs/1610.06548` (visited on 07/04/2025).

[20] VLADIMIR I Tretyak and YURI G Zdesenko. “TABLES OF DOUBLE BETA DECAY DATA—AN UPDATE”. In: *Atomic Data and Nuclear Data Tables* 80.1 (Jan. 2002), pp. 83–116. ISSN: 0092-640X. DOI: `10.1006/adnd.2001.0873`. URL: `https://www.sciencedirect.com/science/article/pii/S0092640X01908733` (visited on 07/08/2025).

[21] M. Agostini et al. “Final Results of GERDA on the Search for Neutrinoless Double- Decay”. en. In: *Physical Review Letters* 125.25 (Dec. 2020), p. 252502. ISSN: 0031-9007, 1079-7114. DOI: `10.1103/PhysRevLett.125.252502`. URL: `https://link.aps.org/doi/10.1103/PhysRevLett.125.252502` (visited on 07/04/2025).

[22] D. Q. Adams et al. “Search for Majorana neutrinos exploiting millikelvin cryogenics with CUORE”. In: *Nature* 604.7904 (Apr. 2022). arXiv:2104.06906 [nucl-ex], pp. 53–58. ISSN: 0028-0836, 1476-4687. DOI: `10.1038/s41586-022-04497-4`. URL: `http://arxiv.org/abs/2104.06906` (visited on 07/04/2025).

[23] S. Abe et al. *Search for Majorana Neutrinos with the Complete KamLAND-Zen Dataset*. arXiv:2406.11438 [hep-ex]. June 2024. DOI: `10.48550/arXiv.2406.11438`. URL: `http://arxiv.org/abs/2406.11438` (visited on 07/04/2025).

[24] The SNO+ Collaboration et al. “Measurement of the ^{8}B Solar Neutrino Flux in SNO+ with Very Low Backgrounds”. In: *Physical Review D* 99.1 (Jan. 2019). arXiv:1812.03355 [hep-ex], p. 012012. ISSN: 2470-0010, 2470-0029. DOI: `10.1103/PhysRevD.99.012012`. URL: `http://arxiv.org/abs/1812.03355` (visited on 01/10/2025).

[25] SNO+ Collaboration et al. “Measurement of the ^{8}B Solar Neutrino Flux Using the Full SNO+ Water Phase Dataset”. In: *Physical Review D* 110.12 (Dec. 2024). arXiv:2407.17595 [hep-ex], p. 122003. ISSN: 2470-0010, 2470-0029. DOI:

10.1103/PhysRevD.110.122003. URL: http://arxiv.org/abs/2407.17595 (visited on 01/10/2025).

[26] SNO+ Collaboration et al. “Evidence of Antineutrinos from Distant Reactors using Pure Water at SNO+”. In: *Physical Review Letters* 130.9 (Mar. 2023). arXiv:2210.14154 [nucl-ex], p. 091801. ISSN: 0031-9007, 1079-7114. DOI: 10.1103/PhysRevLett.130.091801. URL: http://arxiv.org/abs/2210.14154 (visited on 01/10/2025).

[27] SNO+ Collaboration et al. *Initial measurement of reactor antineutrino oscillation at SNO+*. arXiv:2405.19700 [hep-ex]. May 2024. DOI: 10.48550/arXiv.2405.19700. URL: http://arxiv.org/abs/2405.19700 (visited on 01/10/2025).

[28] SNO+ Collaboration et al. “Search for invisible modes of nucleon decay in water with the SNO+ detector”. In: *Physical Review D* 99.3 (Feb. 2019). arXiv:1812.05552 [hep-ex], p. 032008. ISSN: 2470-0010, 2470-0029. DOI: 10.1103/PhysRevD.99.032008. URL: http://arxiv.org/abs/1812.05552 (visited on 01/10/2025).

[29] SNO+ Collaboration et al. “Improved search for invisible modes of nucleon decay in water with the SNO+ detector”. In: *Physical Review D* 105.11 (June 2022). arXiv:2205.06400 [hep-ex], p. 112012. ISSN: 2470-0010, 2470-0029. DOI: 10.1103/PhysRevD.105.112012. URL: http://arxiv.org/abs/2205.06400 (visited on 01/10/2025).

[30] SNO+ Collaboration et al. “The SNO+ Experiment”. In: *Journal of Instrumentation* 16.08 (Aug. 2021). arXiv:2104.11687 [physics], P08059. ISSN: 1748-0221. DOI: 10.1088/1748-0221/16/08/P08059. URL: http://arxiv.org/abs/2104.11687 (visited on 12/05/2024).

[31] SNO+ Collaboration et al. “Development, characterisation, and deployment of the SNO+ liquid scintillator”. In: *Journal of Instrumentation* 16.05 (May 2021). arXiv:2011.12924 [physics], P05009. ISSN: 1748-0221. DOI: 10.1088/

1748-0221/16/05/P05009. URL: `http://arxiv.org/abs/2011.12924` (visited on 01/13/2025).

[32] Victor Hess. *On the Observations of the Penetrating Radiation during Seven Balloon Flights*. 2018. URL: `https://arxiv.org/abs/1808.02927`.

[33] J. Alvarez-Muñiz et al. "Cosmic Rays". In: *Particle Data Group* 110.3 (May 2024). DOI: `10.1103/PhysRevD.110.030001`.

[34] Stefano Cecchini and Maurizio Spurio. *Atmospheric muons: experimental aspects*. 2012. URL: `https://arxiv.org/abs/1208.1171`.

[35] J. Bailey et al. "Measurements of relativistic time dilatation for positive and negative muons in a circular orbit". en. In: *Nature* 268.5618 (July 1977). Publisher: Nature Publishing Group, pp. 301–305. ISSN: 1476-4687. DOI: `10.1038/268301a0`. URL: `https://www.nature.com/articles/268301a0` (visited on 07/08/2025).

[36] H. Bichsel, D. E. Groom, and S. R. Klein. "Passage of Particles Through Matter". In: *Particle Data Group* 40.10 (2016). DOI: `10.1088/1674-1137/40/10/100001`. URL: `https://pdg.lbl.gov/2016/reviews/rpp2016-rev-passage-particles-matter.pdf`.

[37] J. J. Beatty, J. Matthews, and S. P. Wakely. "Cosmic Rays". In: *Particle Data Group* 40.10 (2016). DOI: `10.1088/1674-1137/40/10/100001`.

[38] D.-M. Mei and A. Hime. "Muon-Induced Background Study for Underground Laboratories". en. In: *Physical Review D* 73.5 (Mar. 2006). arXiv:astro-ph/0512125, p. 053004. ISSN: 1550-7998, 1550-2368. DOI: `10.1103/PhysRevD.73.053004`. URL: `http://arxiv.org/abs/astro-ph/0512125`.

[39] Donald E. Groom, Nikolai V. Mokhov, and Sergei I. Striganov. "MUON STOPPING POWER AND RANGE TABLES 10 MeV–100 TeV". en. In: *Atomic Data and Nuclear Data Tables* 78.2 (July 2001), pp. 183–356. ISSN: 0092640X. DOI: `10.1006/adnd.2001.0861`.

[40] Y.-F. Wang et al. "Predicting neutron production from cosmic-ray muons". In: *Physical Review D* 64.1 (June 2001). Publisher: American Physical Society, p. 013012. DOI: `10.1103/PhysRevD.64.013012`. URL: `https://link.aps.org/doi/10.1103/PhysRevD.64.013012` (visited on 07/11/2025).

[41] Obada Nairat, John F. Beacom, and Shirley Weishi Li. *Neutron Tagging Can Greatly Reduce Spallation Backgrounds in Super-Kamiokande*. arXiv:2409.10611 [hep-ph]. Sept. 2024. DOI: `10.48550/arXiv.2409.10611`. URL: `http://arxiv.org/abs/2409.10611` (visited on 01/02/2025).

[42] The SNO+ Collaboration et al. "Measurement of neutron-proton capture in the SNO+ water phase". In: *Physical Review C* 102.1 (July 2020). arXiv:2002.10351 [physics], p. 014002. ISSN: 2469-9985, 2469-9993. DOI: `10.1103/PhysRevC.102.014002`. URL: `http://arxiv.org/abs/2002.10351` (visited on 01/03/2025).

[43] S. Agostinelli et al. "Geant4—a simulation toolkit". In: *Nuclear Instruments and Methods in Physics Research Section A: Accelerators, Spectrometers, Detectors and Associated Equipment* 506.3 (July 2003), pp. 250–303. ISSN: 0168-9002. DOI: `10.1016/S0168-9002(03)01368-8`. URL: `https://www.sciencedirect.com/science/article/pii/S0168900203013688` (visited on 01/21/2025).

[44] *About FLUKA — The official CERN FLUKA website*. URL: `https://fluka.cern/about` (visited on 07/16/2025).

[45] H. M. Araújo et al. "Muon-induced neutron production and detection with GEANT4 and FLUKA". In: *Nuclear Instruments and Methods in Physics Research Section A: Accelerators, Spectrometers, Detectors and Associated Equipment* 545.1 (June 2005), pp. 398–411. ISSN: 0168-9002. DOI: `10.1016/j.nima.2005.02.004`. URL: `https://www.sciencedirect.com/science/article/pii/S0168900205005838` (visited on 07/11/2025).

[46] R. Hertenberger, M. Chen, and B. L. Dougherty. "Muon-induced neutron and pion production in an organic liquid scintillator at a shallow depth". en. In: *Physical Review C* 52.6 (Dec. 1995), pp. 3449–3459. ISSN: 0556-2813, 1089-

490X. DOI: `10.1103/PhysRevC.52.3449`. URL: `https://link.aps.org/doi/10.1103/PhysRevC.52.3449` (visited on 05/09/2025).

[47] F. Boehm et al. “Neutron production by cosmic-ray muons at shallow depth”. en. In: *Physical Review D* 62.9 (Oct. 2000), p. 092005. ISSN: 0556-2821, 1089-4918. DOI: `10.1103/PhysRevD.62.092005`. URL: `https://link.aps.org/doi/10.1103/PhysRevD.62.092005` (visited on 05/09/2025).

[48] F. P. An et al. “Cosmogenic neutron production at Daya Bay”. en. In: *Physical Review D* 97.5 (Mar. 2018), p. 052009. ISSN: 2470-0010, 2470-0029. DOI: `10.1103/PhysRevD.97.052009`. URL: `https://link.aps.org/doi/10.1103/PhysRevD.97.052009` (visited on 05/08/2025).

[49] S. C. Blyth et al. “Measurement of cosmic-ray muons and muon-induced neutrons in the Aberdeen Tunnel Underground Laboratory”. en. In: *Physical Review D* 93.7 (Apr. 2016), p. 072005. ISSN: 2470-0010, 2470-0029. DOI: `10.1103/PhysRevD.93.072005`. URL: `https://link.aps.org/doi/10.1103/PhysRevD.93.072005` (visited on 05/09/2025).

[50] M. Shinoki et al. “Measurement of the cosmogenic neutron yield in Super-Kamiokande with gadolinium loaded water”. In: *Phys. Rev. D* 107 (9 May 2023), p. 092009. DOI: `10.1103/PhysRevD.107.092009`. URL: `https://link.aps.org/doi/10.1103/PhysRevD.107.092009`.

[51] S. Abe et al. “Production of radioactive isotopes through cosmic muon spallation in KamLAND”. en. In: *Physical Review C* 81.2 (Feb. 2010), p. 025807. ISSN: 0556-2813, 1089-490X. DOI: `10.1103/PhysRevC.81.025807`. URL: `https://link.aps.org/doi/10.1103/PhysRevC.81.025807` (visited on 05/08/2025).

[52] L. V. D. Collaboration. *Measurement of the Neutron Flux Produced by Cosmic-Ray Muons with LVD at Gran Sasso*. arXiv:hep-ex/9905047. May 1999. DOI: `10.48550/arXiv.hep-ex/9905047`. URL: `http://arxiv.org/abs/hep-ex/9905047` (visited on 11/05/2025).

[53] G. Bellini et al. “Cosmogenic Backgrounds in Borexino at 3800 m water-equivalent depth”. en. In: *Journal of Cosmology and Astroparticle Physics* 2013.08 (Aug. 2013), p. 049. ISSN: 1475-7516. DOI: `10.1088/1475-7516/2013/08/049`. URL: `https://dx.doi.org/10.1088/1475-7516/2013/08/049` (visited on 05/09/2025).

[54] Lin Zhao et al. “Measurement of Muon-induced Neutron Production at the China Jinping Underground Laboratory”. In: *Chinese Physics C* 46.8 (Aug. 2022). arXiv:2108.04010 [hep-ex], p. 085001. ISSN: 1674-1137, 2058-6132. DOI: `10.1088/1674-1137/ac66cc`. URL: `http://arxiv.org/abs/2108.04010` (visited on 05/09/2025).

[55] B. Aharmim et al. “Cosmogenic Neutron Production at the Sudbury Neutrino Observatory”. In: *Physical Review D* 100.11 (Dec. 2019). arXiv:1909.11728 [hep-ex], p. 112005. ISSN: 2470-0010, 2470-0029. DOI: `10.1103/PhysRevD.100.112005`. URL: `http://arxiv.org/abs/1909.11728` (visited on 12/05/2024).

[56] M. Aglietta et al. “Neutron flux generated by cosmic-ray mouns at 5200 hg/cm2 s.r. underground. Depth-neutron intensity curve”. en. In: *Il Nuovo Cimento C* 12.4 (July 1989), pp. 467–477. ISSN: 0390-5551. DOI: `10.1007/BF02525079`. URL: `https://doi.org/10.1007/BF02525079` (visited on 05/09/2025).

[57] V.A. Kudryavtsev, N.J.C. Spooner, and J.E. McMillan. “Simulations of muon-induced neutron flux at large depths underground”. en. In: *Nuclear Instruments and Methods in Physics Research Section A: Accelerators, Spectrometers, Detectors and Associated Equipment* 505.3 (June 2003). Publisher: Elsevier BV, pp. 688–698. ISSN: 0168-9002. DOI: `10.1016/s0168-9002(03)00983-5`. URL: `https://linkinghub.elsevier.com/retrieve/pii/S0168900203009835` (visited on 07/11/2025).

[58] D.F. Cowen et al. “The Sudbury Neutrino Observatory electronics chain”. In: *IEEE Transactions on Nuclear Science* 42.4 (Aug. 1995). Conference Name:

IEEE Transactions on Nuclear Science, pp. 925–932. ISSN: 1558-1578. DOI: `10.1109/23.467769`. URL: `https://ieeexplore.ieee.org/document/467769/?arnumber=467769` (visited on 01/10/2025).

[59] J. Caravaca and G. D. Orebi Gann. *ECA Calibrations in RAT*. SNO+ Internal Document (doc-3698-v2). Jan. 2017.

[60] SNO+ Collaboration et al. “Optical calibration of the SNO+ detector in the water phase with deployed sources”. In: *Journal of Instrumentation* 16.10 (Oct. 2021). arXiv:2106.03951 [physics], P10021. ISSN: 1748-0221. DOI: `10.1088/1748-0221/16/10/P10021`. URL: `http://arxiv.org/abs/2106.03951` (visited on 02/19/2025).

[61] Freija Descamps. *PCA calibration with SNO+ RAT*. SNO+ Internal Document (doc-1987-v5). May 2016.

[62] Logan Lebanowski and Meng Luo. *SNO+ Energy Calibration with the 16N Source*. SNO+ Internal Document (doc-5003-v2). June 2018.

[63] Ian T. Coulter. “Modelling and reconstruction of events in SNO+ related to future searches for lepton and baryon number violation”. PhD thesis. Oxford U., 2013. URL: `https://ora.ox.ac.uk/objects/uuid:495395b3-bf15-4c9b-851d-c13e7dad8a22`.

[64] L. Lebanowski, E. Leming, and L. Meng. *Reconstructed* ^{16}N *spectra and fits with energy calibration*. SNO+ Internal Document (doc-5407-v10). Jan. 2019.

[65] Shirley Weishi Li and John F. Beacom. “First calculation of cosmic-ray muon spallation backgrounds for MeV astrophysical neutrino signals in Super-Kamiokande”. In: *Physical Review C* 89.4 (Apr. 2014). arXiv:1402.4687 [hep-ph]. ISSN: 0556-2813, 1089-490X. DOI: `10.1103/PhysRevC.89.045801`. URL: `http://arxiv.org/abs/1402.4687` (visited on 07/07/2025).

[66] Marc Paterno. *Calculating efficiencies and their uncertainties*. en. Tech. rep. FERMILAB-TM-2286-CD, 15017262. Dec. 2004, FERMILAB–TM–2286–CD,

15017262. DOI: `10.2172/15017262`. URL: `http://www.osti.gov/servlets/purl/15017262-pSCrSE/native/` (visited on 06/12/2025).

[67] Robert Collins. “Intro to Sampling Methods”. In: (). URL: `https://www.cse.psu.edu/~rtc12/CSE586/lectures/cse586samplingPreMCMC.pdf`.

[68] S. Hans et al. “Purification of telluric acid for SNO+ neutrinoless double-beta decay search”. In: *Nuclear Instruments and Methods in Physics Research Section A: Accelerators, Spectrometers, Detectors and Associated Equipment* 795 (Sept. 2015), pp. 132–139. ISSN: 0168-9002. DOI: `10.1016/j.nima.2015.05.045`. URL: `https://www.sciencedirect.com/science/article/pii/S0168900215006853` (visited on 01/14/2025).

[69] D. J. Auty et al. “A Method to Load Tellurium in Liquid Scintillator for the Study of Neutrinoless Double Beta Decay”. In: *Nuclear Instruments and Methods in Physics Research Section A: Accelerators, Spectrometers, Detectors and Associated Equipment* 1051 (June 2023). arXiv:2212.12444 [physics], p. 168204. ISSN: 01689002. DOI: `10.1016/j.nima.2023.168204`. URL: `http://arxiv.org/abs/2212.12444` (visited on 12/12/2024).